STRESS-BASED TOPOLOGY OPTIMIZATION FOR STEADY-STATE AND TRANSIENT THERMOELASTIC DESIGN

A Dissertation
Presented to
The Academic Faculty

By

Mark K. Leader

In Partial Fulfillment
of the Requirements for the Degree
Doctor of Philosophy in the
Aerospace Engineering

Georgia Institute of Technology

August 2021

STRESS-BASED TOPOLOGY OPTIMIZATION FOR STEADY-STATE AND TRANSIENT THERMOELASTIC DESIGN

Thesis committee:

Dr. Graeme J. Kennedy, Advisor
School of Aerospace Engineering
Georgia Institute of Technology

Dr. Claudio V. Di Leo
School of Aerospace Engineering
Georgia Institute of Technology

Dr. Brian J. German
School of Aerospace Engineering
Georgia Institute of Technology

Dr. Justin S. Gray
NASA Glenn Research Center

Dr. Julian J. Rimoli
School of Aerospace Engineering
Georgia Institute of Technology

Date approved: June 29, 2021

ACKNOWLEDGMENTS

I feel very fortunate for having had this time to explore and focus on the research presented here, and I have a lot of people to thank for making this time so rewarding. First, and most of all, I would like to thank my wife Natalie for her constant support throughout this process, and for encouraging me when I needed it the most. Thanks to my parents, Richard and Carrie, for modeling life-long learning, and for allowing me the freedom and opportunity to pursue my interests. Thanks to my in-laws, Ron and Michelle, for their support over these years as well.

Next, I would like to thank my advisor, Dr. Graeme Kennedy. I am incredibly thankful for his mentorship and support, and for introducing me to new ideas which led to this work. I would also like to thank my thesis committee members, Dr. Brian German, Dr. Julian Rimoli, Dr. Claudio Di Leo, and Dr. Justin Gray, for the time they have taken to serve on the committee. Each committee member provides a unique perspective and I appreciate their thoughtful feedback.

I would like to thank all of the friends that I met during my graduate studies, in particular: Tingwei Chin, Komahan Boopathy, Jan Kiviaho, Chun Rong Ngoh, Donald Bistri, Elena Garombo, Rick Dong, and Aaron Fu. As the eldest member of the group when I joined, Tingwei patiently answered my endless questions and I am glad to still count him as a friend. Komahan is the most curious person that I have ever met, and his ability to understand concepts so fundamentally has inspired me. Aaron has impressed me since he joined the lab and I know the group has a bright future with him leading the way now.

I am grateful for the funding provided by NASA's Transformational Tools and Technologies Project under grant number 80NSSC18M0151 with Technical Monitor Jeff Chin. This research was also supported in part through research cyberinfrastructure resources and services provided by the Partnership for an Advanced Computing Environment (PACE) [1] at the Georgia Institute of Technology.

TABLE OF CONTENTS

LIST OF TABLES

LIST OF FIGURES

CHAPTER 1
INTRODUCTION

1.1 Background

Topology optimization is a powerful design tool, benefiting from a broadened design space that can be efficiently navigated with gradient-based optimization algorithms. This is especially useful when considering coupled multiphysics design problems, where the optimal design becomes less intuitive to human designers - potentially enabling next-generation aviation concepts, including all-electric aircraft. However, generating useful designs relies on accurately modeling the physics relevant to the structure. Furthermore, the structure's design stress should be considered in every case in order to obtain feasible designs. Current topology optimization approaches have used narrowly-scoped physics models, neglect stress-constraints, or both. This thesis enhances multiphysics topology optimization by applying stress-based topology optimization to both problems with frequency analysis, and problems with transient heating considerations. The results demonstrated here achieve highly detailed designs at a scalable computational cost through the use of a novel adaptive mesh refinement approach.

Broadly speaking, topology optimization (first developed by Bendsøe and Kikuchi [2]) is a design process which optimizes a structure's shape to improve it's performance. This process depends on what the structure is being required to do, and any design constraints needed for the structure. Forces, boundary conditions, and material properties all need to be defined as well. Figure 1.1a shows an example problem domain with forces and boundary conditions. Next, this domain is discretized - or meshed - into many elements (Figure 1.1b). The topology optimization problem then seeks to determine whether material should be present (or not) in each of these elements, which determines the optimized

design[1] (Figure 1.1c). The final design depends on the problem formulation chosen, which takes a form similar to Equation 1.1. The problem formulation starts with an objective function that we want to minimize - such as "minimize the mass of the structure". The next step of the optimization problem formulation is to define constraints, for example: "constrain the maximum stress in the design to be less than the material's yield stress" to prevent material failure. Finally, this is all governed by the solution of the finite element equations, because the objective and constraint values of the problem depend on the physics being modeled. The optimization problem is stated with respect to the design variables ($\mathbf{x}$), which describe whether there is material or not in each discretized element, determining the layout of the final design (for example, a design variable value $x_i = 1$ indicates that the i^{th} element contains material, whereas a design variable value $x_i = 0$ indicates that the i^{th} element is void). Figure 1.1c shows the final design for this example problem, where the final design is shown in blue and green (representing two different materials in this case), and the void region is shown in grey.

$$\begin{aligned} \text{min} \quad & \text{objective function} \\ \text{with respect to} \quad & 0 < \mathbf{x} \leq 1 \\ \text{subject to} \quad & \text{constraints} \\ \text{governed by} \quad & \text{finite element solution} \end{aligned} \tag{1.1}$$

Topology optimization has already demonstrated its potential for significant weight reduction. Applications of topology optimization within the aerospace industry have enabled weight reduction of critical aircraft components. For example, using topology optimization, Airbus achieved a weight reduction of 1,000 kilograms per aircraft on components of the A380 [4, 5], while Bombardier reduced the weight of their passenger jet wingbox ribs by 10% [6]. However, these designs relied solely on mechanical analysis with no

[1] This is the case for what is used in this work, which is known as "density-based" topology optimization, which differs from the other primary approach known as the "level-set method"[3]

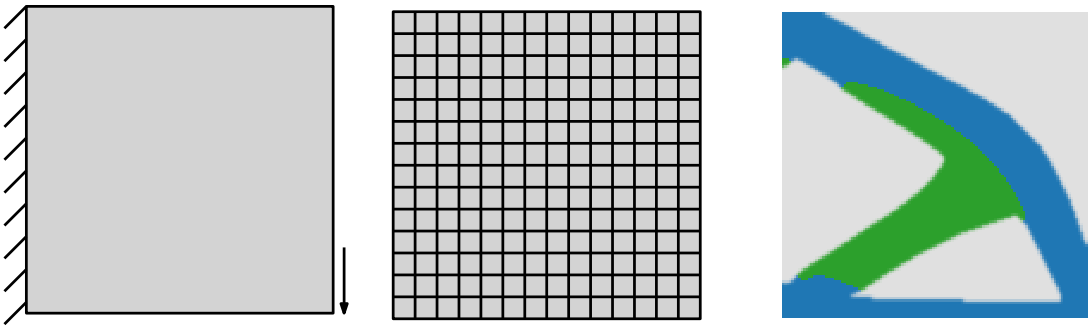

(a) Problem (b) Discretization (c) Design

Figure 1.1: Example topology optimization problem

consideration of stress-constraints.

Topology optimization can be especially beneficial for problems involving complex physics, such as thermoelasticity, where the coupled nature of the problem makes the optimal design less intuitive for the human designer. From a design standpoint, these thermal structures have several design requirements to consider. First, thermal structures must avoid material stress limits to ensure safe operation. Second, thermal structures must effectively conduct heat away from temperature-sensitive components so that temperature limits are avoided. Finally, weight should be minimized to improve overall vehicle performance.

One particular application that can benefit from thermoelastic topology optimization is electric aircraft. Fully electric aircraft offer the potential of improvements in operating costs, community noise, emissions, energy efficiency, and reliability over conventional vehicles that rely on internal combustion engines [7]. Two key challenges for electric aircraft are energy storage weight and thermal management. Combustion engines offer the advantages that the weight of the aircraft decreases throughout the flight as fuel is burned, and that waste heat is partially rejected through the exhaust into the atmosphere. However, for battery electric aircraft, the battery weight remains constant throughout the flight and methods available to dissipate heat generated by electric motors, power electronics, and batteries are more limited. As a result, both weight and thermal management are critical considerations in the design of electric aircraft. However, the correct physics must be

modeled to achieve meaningful designs. Structures are often exposed to transient thermal environments that cannot be modeled accurately using steady-state analysis. Following the example of electric aircraft, the heat generated by the electric motors will be at its greatest during takeoff and climb, while the convective cooling is at its least. During cruise, the heat generated will be less than takeoff and climb due to a lower required thrust, while convective cooling will be at its greatest magnitude. In this example, the rate of heat into and out of the structure change frequently throughout the flight. This indicates that the structure is in a predominantly transient thermal state. Using steady-state analysis to design this structure not only risks underestimating the maximum temperature, but can also lead to misidentifying the load case causing the worst-case thermal state. Using steady-state analysis for problems with transient thermal behavior also misrepresents the spatial temperature distribution, leading to significant design differences when topology optimization is used. This is just one particular example to illustrate the importance of using transient analysis for thermal-structural design problems; transient heat transfer is important to consider for a wide-range of problems, including electric vehicles, as well as MEMS devices, integrated circuits [8], turbomachinery, combustion engines, space launch vehicles, atmosphere re-entry, and more.

1.1.1 Thermoelastic topology optimization

Topology optimization has been used in a wide range of applications to produce novel, lightweight designs. Topology optimization is an ideal design tool for problems requiring both thermal and mechanical design considerations because it can be used to design high-performance structures while considering the thermomechanical coupling of the physics of the problem, while also considering time-dependent design effects. Thermoelastic topology optimization was first studied by Rodrigues and Fernandes [9]. Since then, thermoelastic topology optimization has been used in a wide range of applications, including microstructure design for maximizing thermal expansion [10], improving thermal transport

properties [11], thermal buckling [12], thermoelectric energy conversion [13], compliance minimization [14, 15, 16, 17], and stress minimization [17, 18]. The consideration of stress-constraints [19, 20, 21], displacement-constraints [22, 23], and temperature-constraints [17, 24] have all also been studied. Many authors have applied topology optimization to heat conduction problems to produce optimal designs for heat sinks [25, 26, 27, 28, 29, 30, 31], and others have included design-dependent thermal loads as well, using various approaches [32, 33, 34, 35, 36, 37]. Other authors have explored topology optimization for combined convection and conduction problems [38, 39, 40, 41], including natural convection problems [42, 43, 44, 45, 46], and heat exchanger design [47, 48, 49, 50, 51, 52]. Kambampati, Jauregui, Museth, and Kim [53] also considered mechanical performance with convective cooling by applying topology optimization to load carrying heat exchangers, by minimizing compliance of the structure subject to mass and temperature constraints. Thermal design problems are especially well-suited for multimaterial design. Multi-material design problems have been studied for both compliance-minimization problems [54, 55], and stress-constrained problems [56]. Kang and James [57] formulated thermoelastic topology optimization problems with temperature-constrained boundaries, and also investigated multi-material designs with material-specific temperature constraints.

Topology optimization in general can be sensitive to the problem formulation. It was found by Pedersen and Pedersen [58, 59] that mechanical compliance is a poor objective function for thermoelastic topology optimization problems, leading to volume constraints which may not be active. Lohan, Dede, and Allison [60] compared four different temperature objectives for topology optimization of heat conducting structures, and found that the results varied greatly depending on the choice of objective. Design-dependent temperature constraints and asymmetric loading were also studied. While compliance is a popular objective function for topology optimization, this work emphasizes the use of stress-constraints throughout. All structures need to be designed so that the expected maximum stress will be lower than the allowable design stress, and given that different topology

optimization problem formulations yield different designs, there seems to be no reason not to include stress in the problem formulation. Minimizing compliance is equivalent to maximizing stiffness. One reason why a stiffer structure might be desirable is to reduce displacement if clearance is a concern, but this concern could be addressed with a displacement constraint if needed. The primary reason why stress-based problems are less popular than compliance-based problems is that stress is a challenging function to consider for topology optimization. A number of issues arise with stress-based topology optimization problems. The first is an issue of imposing a global constraint on a point-wise quantity [61]. The second issue is the stress-singularity issue that affects stress constraints in areas of vanishing density [62, 63, 64]. Solutions to these problems are widely known now and the approach taken in this work is presented in chapter 4. The third issue is that stress-based problems have a high degree of nonlinearity compared to compliance-based problems, making the optimization problem more difficult to solve. This nonlinearity arises because local stresses are highly sensitive to density changes in neighboring regions. This requires a robust optimization algorithm to reliably solve these types of problems. Stress-based topology optimization problems are also known to be more computationally expensive than compliance-based topology optimization problems [64, 65].

Selecting the right problem formulation only matters if we are modeling the physics of the problem accurately to begin with, and many thermal design problems are predominantly transient in nature. There are a number of reasons that steady-state analysis would not be suitable for certain thermoelastic topology optimization problems. First, the boundary conditions are often heavily dependent on time, which makes determining the worst-case loads challenging. Second, the distribution of temperature, and therefore also stress, will differ with transient physics, which would lead to different designs. Third, the steady-state heat transfer problem cannot be solved without fixed-temperature boundary conditions that are physically unrealistic in most instances. Finally, time-dependent analysis allows for the optimization to account for the fact the physics is both path-dependent and design-

dependent. The path-dependence arises because the maximum temperature depends on the temperature at all previous time-steps and the design dependence arises because the maximum temperature for one design would not necessarily occur at the same time-step for a different design.

Several authors have performed transient thermal topology optimization, considering conduction [66, 67, 68, 69, 70, 71, 72] as well as combined conduction and convection [73]. Zeng, Wang, Yang, and Alexandersen [8] used topology optimization with transient convective heat transfer to design efficient heat sinks for microchips. Designs generated using transient physics were compared to designs generated using steady-state physics, demonstrating that designs generated using transient analysis performed better in transient thermal environments than designs generated using steady-state analysis. Some work has also been done on solving topology optimization with transient thermoelastic physics. Li, Steven, and Xie [74] solved transient thermoelastic topology optimization with evolutionary structural optimization (ESO) using 1,749 total elements to minimize either the maximum stress or the time-averaged stress. Deng, Yan, and Cheng [75] performed concurrent multi-objective topology optimization of porous material, minimizing compliance due to mechanical loads, and minimizing thermal expansion due to thermal loads. Zhuang and Xiong [69] solved topology optimization with transient thermal loads using equivalent static thermal loads. Kang and James [76] used topology optimization to design shape memory alloys, requiring the use of transient thermal analysis, and Mello, Salas, and Silva [77] designed electrothermomechanical actuated compliant mechanisms with the objective of maximizing the displacement integral over time. To date, most transient topology optimization problems focus on the thermal aspect of the design only, and of the authors who have solved thermoelastic topology optimization problems, none have incorporated stress-constraints, and much of the existing work relies on using approximation techniques to reduce computational cost. The results presented in chapter 6 are the first demonstration of stress-constrained transient thermoelastic topology optimization.

One of the main roadblocks in implementing time-dependent topology optimization of any kind is the high computational cost. A conventional thermoelastic topology optimization problem with steady-state physics typically requires the solution of two linear systems per optimization iteration, one for forward analysis and another to compute the gradient. On the other hand, the computational cost per iteration is much higher for time-dependent thermoelastic topology optimization, which requires the solution of at least two linear systems *for each* time step - increasing the computation cost by by 10 to 100 times, if not more. For this reason, much of the previous work on time-dependent thermal topology optimization utilizes strategies to reduce computation time. In this work, I show that the computational cost is manageable without utilizing these strategies due to the computational efficiency of the analysis and optimization tools, allowing higher-fidelity analysis to be used directly for optimization, and also resulting in more detailed designs. This work will solve much larger problems than have been previously performed in the literature, with $\mathcal{O}(10^5)$ elements, without using any approximate solution techniques. These results have a higher resolution than this element count would imply, too, thanks to the novel adaptive mesh refinement approach described in chapter 3.

1.1.2 Natural frequency constrained topology optimization

The reason for emphasizing stress-constrained transient thermoelastic topology optimization is to properly represent the underlying physics of the problem and use meaningful constraints for the design. The choice of constraints depends heavily on the structure's environment, and many structures operate in highly vibratory environments. For that reason, many design problems require consideration of natural frequencies to prevent dynamic instability. For aerospace structures operating in high-vibration environments, it is important to require that the structure's fundamental frequency be greater than a critical threshold to avoid an unwanted frequency response. Imposing a lower bound on a structure's natural frequencies results in a stiffer design, so for these problems especially, it is critical that

stress constraints are used to ensure that material stress limits are satisfied.

Applying natural frequency constraints to topology optimization presents a number of challenges. Grandhi [78] notes that mode switching during the optimization problem can be one of the most difficult challenges to address. Mode switching occurs during topology optimization because as the design changes, the lowest eigenvalue is increased, but this can cause a new mode shape to become the lowest eigenvalue. Another challenge associated with natural frequency constraints is that an eigenvalue problem needs to be solved at every optimization iteration which is very computationally expensive, especially for large problems. Because of this, previous work on topology optimization with frequency constraints has been limited to smaller problems. Grandhi and Venkayya [79] performed frequency constrained mass minimization using both equality and inequality constraints for truss problems with up to 489 design variables. Xu, Jiang, Tong, and Wu [80] performed structural optimization on ground truss structures with natural frequency, stress, displacement, and buckling constraints on problems with on the order of ten degrees of freedom. Pedersen [81] used topology optimization to maximize the eigenvalues of different plate problems with between 6,000 and 10,000 elements, and Shu, Wang, Fang, Ma, and Wei [82] sought to minimize the frequency response of a bi-clamped beam subject to harmonic forcing using the level set method for 2- and 3D problems. Ferrari, Lazarov, and Sigmund [83] took a different approach to the problem of maximizing the fundamental frequency by replacing the eigenvalue problem with a frequency response problem, and found that this was an efficient approach allowing them to solve problems with $\mathcal{O}(10^6)$ degrees of freedom. However, the frequency response function is not compatible as an optimization constraint. Dunning, Ovtchinnikov, Scott, and Kim [84] found success implementing a block Jacobi Conjugate Gradient method to solve the buckling eigenvalue problem. To apply frequency constraints, an efficient eigensolver is needed to robustly and accurately evaluate the eigenvalues and eigenvectors of interest. Within the structural finite-element community it is common to solve generalized eigenvalue problems using the Lanczos method [85]. Sleijpen and Vorst

[86] present an efficient Jacobi–Davidson method solver for linear eigenvalue problems. Other authors have since continued to study the Jacobi–Davidson method to solve generalized eigenvalue problems [87, 88, 89]. The Jacobi–Davidson method is preferable to Lanczos because it can evaluate eigenvalues accurately while using less expensive inexact solutions of a linear system at each iteration.

CHAPTER 2
TRAJECTORY-BASED THERMAL ANALYSIS

2.1 Background

NASA's Maxwell X-57 aircraft is being developed under the Scalable Convergent Electric Propulsion Technology and Operations Research (SCEPTOR) program, which is converting a general aviation class aircraft, the Tecnam P2006T, from using combustion engines to being fully electric powered. The final version of the X-57, referred to as the Mod IV, is estimated to reduce the overall energy requirement by 4.8 times compared to the baseline aircraft [90]. A key modification that allows for such a significant increase in efficiency is the use of 12 high-lift motors distributed across both wings. These high-lift motors increase the dynamic pressure across the wings at low speeds, allowing the wings to be sized for cruise rather than takeoff and landing [91]. This reduces the wing area by a factor of 2.5, decreasing both cruise drag and structural weight [90].

Electric aircraft generate excess heat from batteries, motors, and power electronics with limited mechanisms to efficiently dissipate it. As a result, it can be beneficial to design electric aircraft structures to both sustain structural loads, while also conducting excess heat to an exposed aerodynamic surface where it can be convected away from the vehicle. These challenges could be addressed with topology optimization, but first, the design thermal load case needs to be determined. This chapter presents a simplified zero-dimensional thermal model of the structure enclosing one of the electric high-lift motors on NASA's X-57 aircraft, using specific mission performance requirements [19]. The thermal model presented here demonstrates that due to the constantly changing heat flux boundary boundary conditions, steady-state thermal equilibrium is never achieved throughout a simulated flight. Initially, the work presented in this chapter was an attempt to determine proper ther-

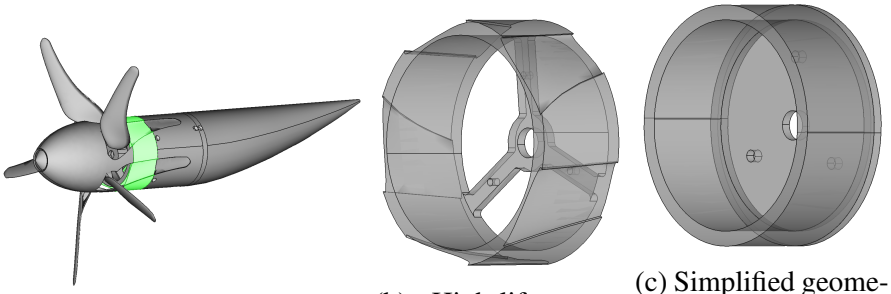

(a) High-lift motor geometry

(b) High-lift motor housing

(c) Simplified geometry used for topology optimization

Figure 2.1: From left to right: High-lift motor geometry with motor housing highlighted, high-lift motor housing geometry shown isolated, and simplified geometry used for topology optimization

mal boundary conditions to design this structure using steady-state thermoelastic topology optimization; instead, it turned into the motivating rationale for the rest of this thesis – highlighting the need for transient thermal analysis for design scenarios like this one.

The X-57 high-lift motor geometry is shown in Figure 2.1a, with the motor housing structure highlighted in green, and shown on its own in Figure 2.1b. The simplified geometry, shown in Figure 2.1c, was created by choosing the greatest volume available to allow the largest possible design space for optimization, while still ensuring that mating conditions with other components, or other relevant clearances, would not be affected. This simplified model is also the basis for the trajectory-based heat transfer analysis presented in this chapter.

2.2 Trajectory-based transient thermal analysis

To obtain worst-case estimates of the thermal conditions, various trajectory profiles are considered to estimate the maximum transient thermal load in the motor housing components. The rate of heat generated by the motor is obtained through the power consumed by the motor and its thermal efficiency, given by

$$\dot{Q}_{\text{in}} = P_{\text{motor}}(1 - \eta_{\text{motor}}). \tag{2.1}$$

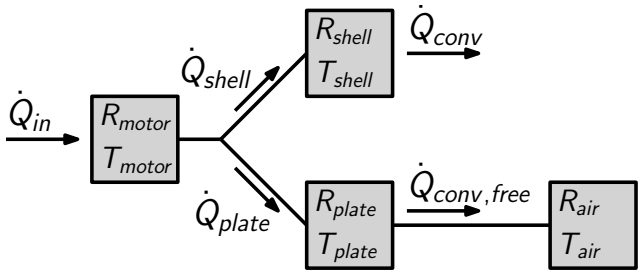

Figure 2.2: Lumped-mass heat transfer model for transient thermal analysis

Any of this heat dissipated to other neighboring structures (for example, the shaft) is not considered, providing a conservative estimate. The outer surface of the shell is exposed to the free stream, so this surface dissipates heat through convection at a rate $\dot{Q}_{\text{conv}}$. The aft surface of the plate is exposed to stagnant air within the nacelle, so this surface will be cooled through unforced convection to air within the nacelle at a rate $\dot{Q}_{\text{conv,free}}$. The remaining surfaces are adjacent to other structural components and are assumed to be insulated, so $\dot{Q} = 0$ is used as the thermal boundary condition for these other regions.

Since the high-lift motors are designed to operate for a short duration of time and in a range of operating conditions, a transient thermal analysis is required to compute the relevant thermal loads. A simplified thermal model based on the heat transfer analogy to electrical circuits is used to perform this transient analysis. A diagram of the simplified model is shown in Figure 2.2. The motor generates heat at a rate defined by Equation 2.1. The heat generated by the motor heats up the motor itself, which conducts heat to the adjacent surfaces on the motor's structural housing. For modeling purposes, the structure of the motor housing is decomposed into two segments: the *shell*, which is the portion encasing the motor radially, and the *plate*, which connects to the aft portion of the motor. The interface between the shell and the plate is neglected for heat transfer analysis. The heat from the motor conducts to these two surfaces in parallel. This decomposition is important because the shell convects to the free-stream, while the plate convects to a cavity of air withing the nacelle aft of the plate. The air inside the nacelle is modeled as a fixed mass of air which is insulated.

Based on the model illustrated in Figure 2.2, heat is conducted from the motor block to the plate at a rate defined by

$$\dot{Q}_{\text{plate}} = \frac{T_{\text{motor}} - T_{\text{plate}}}{R_{\text{plate}}}, \tag{2.2}$$

and heat is conducted to the shell at a rate of

$$\dot{Q}_{\text{shell}} = \frac{T_{\text{motor}} - T_{\text{shell}}}{R_{\text{shell}}}. \tag{2.3}$$

The heat from the plate is dissipated to the cavity of air aft of it within the nacelle through free convection at a rate of

$$\dot{Q}_{\text{conv,free}} = A_{\text{plate}} h_{\text{plate}} (T_{\text{plate}} - T_{\text{air}}), \tag{2.4}$$

where A_{plate} is the area of one of the faces of the plate, h_{plate} is the convective heat transfer coefficient from the plate to the air within the nacelle, A_{shell} is the outer surface of the shell exposed to the free-stream, and h_{shell} is the convective heat transfer coefficient from the shell to the free-stream. The heat from the shell is dissipated through convection to the atmosphere at a rate of

$$\dot{Q}_{\text{conv}} = A_{\text{shell}} h_{\text{shell}} (T_{\text{shell}} - T_{\infty}). \tag{2.5}$$

Each of these heat transfer rates can be used to compute the rate of temperature change for each component

$$\frac{\mathrm{d}T_{\text{motor}}}{\mathrm{d}t} = \frac{1}{m_{\text{motor}} c_{\text{motor}}} (\dot{Q}_{\text{in}} - \dot{Q}_{\text{plate}} - \dot{Q}_{\text{shell}}), \tag{2.6}$$

$$\frac{\mathrm{d}T_{\text{plate}}}{\mathrm{d}t} = \frac{1}{m_{\text{plate}} c_{\text{plate}}} (\dot{Q}_{\text{plate}} - \dot{Q}_{\text{conv,free}}), \tag{2.7}$$

Table 2.1: Nominal trajectory profile for the analysis of thermal loads on high-lift motors

Phase	duration (s)	HLP Power (%)	Velocity (kts)	Altitude (m)
HLP run-up	30	100	0	0
go/no-go	30	0	0	0
ground roll	10	100	0 – 64	0
climb to 1500'	90	75	64 – 105	0 – 457
cruise climb	540	0	105 – 135	457 – 1744
cruise	300	0	135	1744
descent to 1500'	450	0	135 – 105	1744 – 457
final approach	180	75	105 – 64	457
go around to 1500'	90	75	105	457
approach pattern	90	0	105	457
final approach	180	75	105 – 64	457 – 0

$$\frac{\mathrm{d}T_{\mathrm{shell}}}{\mathrm{d}t} = \frac{1}{m_{\mathrm{shell}} c_{\mathrm{shell}}} (\dot{Q}_{\mathrm{shell}} - \dot{Q}_{\mathrm{conv}}), \tag{2.8}$$

$$\frac{\mathrm{d}T_{\mathrm{air}}}{\mathrm{d}t} = \frac{1}{m_{\mathrm{air}} c_{\mathrm{v,air}}} \dot{Q}_{\mathrm{conv,free}}. \tag{2.9}$$

The efficiency losses of the motor heat up the motor block at a rate of $\dot{Q}_{\mathrm{in}}$, which is cooled through conduction to the plate and the shell at rates $\dot{Q}_{\mathrm{plate}}$, and $\dot{Q}_{\mathrm{shell}}$, respectively. The plate temperature increases at a rate proportional to the difference between the heat it takes on from the motor $\dot{Q}_{\mathrm{plate}}$ and the rate that it cools via free convection, $\dot{Q}_{\mathrm{conv,free}}$. The temperature of the shell increases at a rate proportional to the difference in the rate of heat it takes from the motor, $\dot{Q}_{\mathrm{shell}}$, and the rate it cools through convection to the free-stream, $\dot{Q}_{\mathrm{conv}}$. Finally, the temperature of the air in the nacelle changes proportionally to the heat it takes from the plate through free convection at a rate of $\dot{Q}_{\mathrm{conv,free}}$. Equation 2.6 through Equation 2.9 can be used to find the temperature history by integrating them over various trajectory profiles.

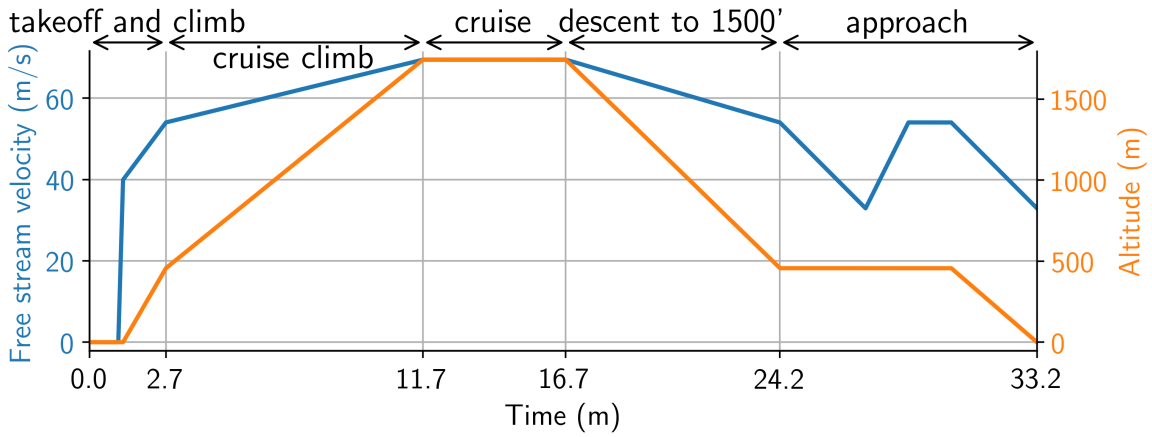

Figure 2.3: Nominal trajectory velocity and altitude profiles

2.2.1 Trajectory profiles

The high-lift motors are designed only to be used during the ascent and descent portions of the flight. Chin, Schnulo, and Smith [92] studied the transient temperature response of passive systems on the X-57 Maxwell. The work in this chapter uses the same parameters for the trajectory profile as Chin, Schnulo, and Smith, who defined a nominal trajectory for the X-57 Mod II aircraft. Additionally, the velocity and altitude time histories are based on the ranges of values provided by Schnulo, Chin, Falck, Gray, Papathakis, Clarke, Reid, and Borer [93], and constant accelerations are assumed for each segment. Table 2.1 provides a summary of the nominal trajectory profile used for computing the approximate thermal loads, and Figure 2.3 provides a graphical representation of the flight velocity and altitude (above ground level) values used for this analysis.

Figure 2.4 shows the thermal profile of the nominal trajectory, with the structural temperature change shown on top, and the total heat flux in and out of the structure shown on the bottom. While the model computes the temperature of each of the components separately, the difference in temperature between components is less than 1%. For this reason, the labels in the legend are collapsed for clarity in Figure 2.4. To illustrate the heat flux over time, the values are combined into either $\dot{Q}_{\text{in}}$, or $\dot{Q}_{\text{out}}$, to more clearly show the total heating and cooling of the structure over the course of the flight. $\dot{Q}_{\text{in}}$ is still simply the heat

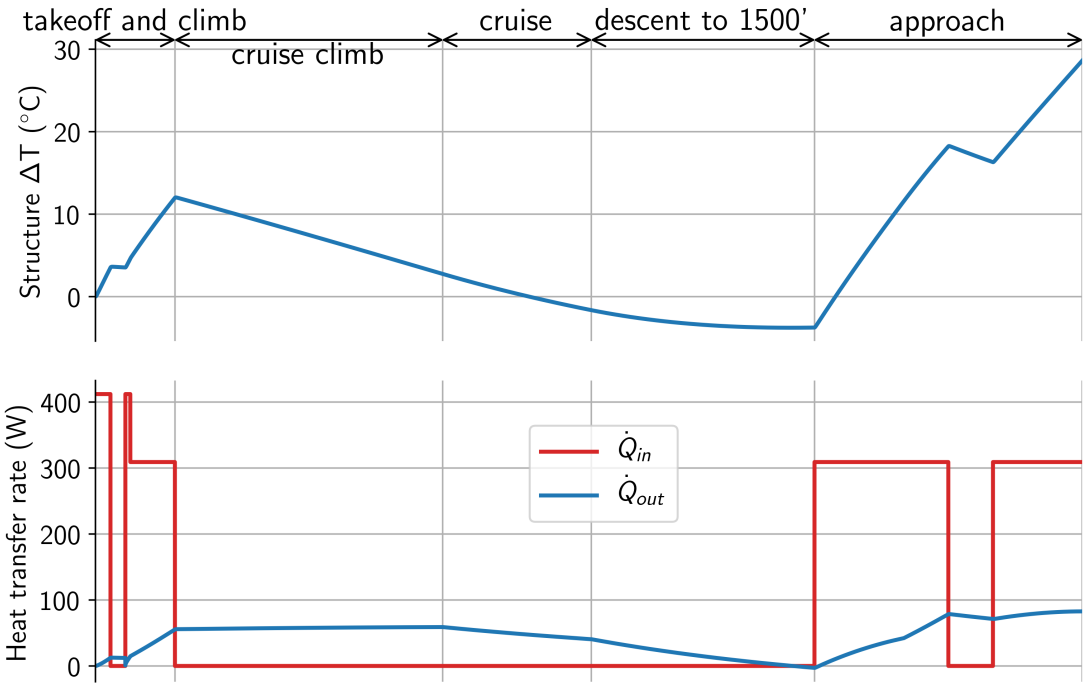

Figure 2.4: Nominal trajectory thermal profile. The temperature of the structure over the course of the simulated trajectory is shown on the top, and the total heat flux in and out of the structure is shown on the bottom.

generated by the motor, while $\dot{Q}_{\text{out}}$ is the sum of $\dot{Q}_{\text{conv}}$ and $\dot{Q}_{\text{conv,free}}$.

The transient thermal behavior for two other possible scenarios was also investigated: a round-trip trajectory, where the nominal trajectory is flown, followed by a 10 minute cool-down, followed by a repeat of the nominal trajectory; and an off-nominal "diverted" scenario, where the takeoff and climb segments are completed, but the aircraft makes an immediate descent, resulting in the motor being required to operate continuously, without the benefit of cooling off during cruise.

The trajectory profile for the round-trip trajectory is shown in Figure 2.5, with the time-histories of the temperature change and heat flux in and out of the structure shown at the top and bottom of Figure 2.6, respectively. The trajectory profile for the diverted trajectory is shown in Figure 2.7, and the time history of the temperature change and the input and output heat flux values are shown at the top and bottom of Figure 2.8, respectively.

These results use a ground level-elevation of 694 m, representative of Edwards Air

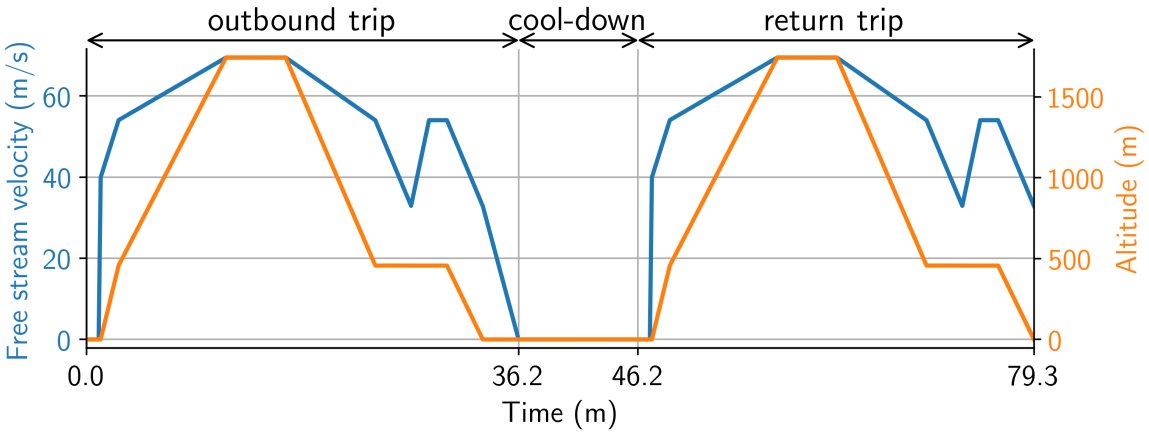

Figure 2.5: Round-trip trajectory velocity and altitude profiles

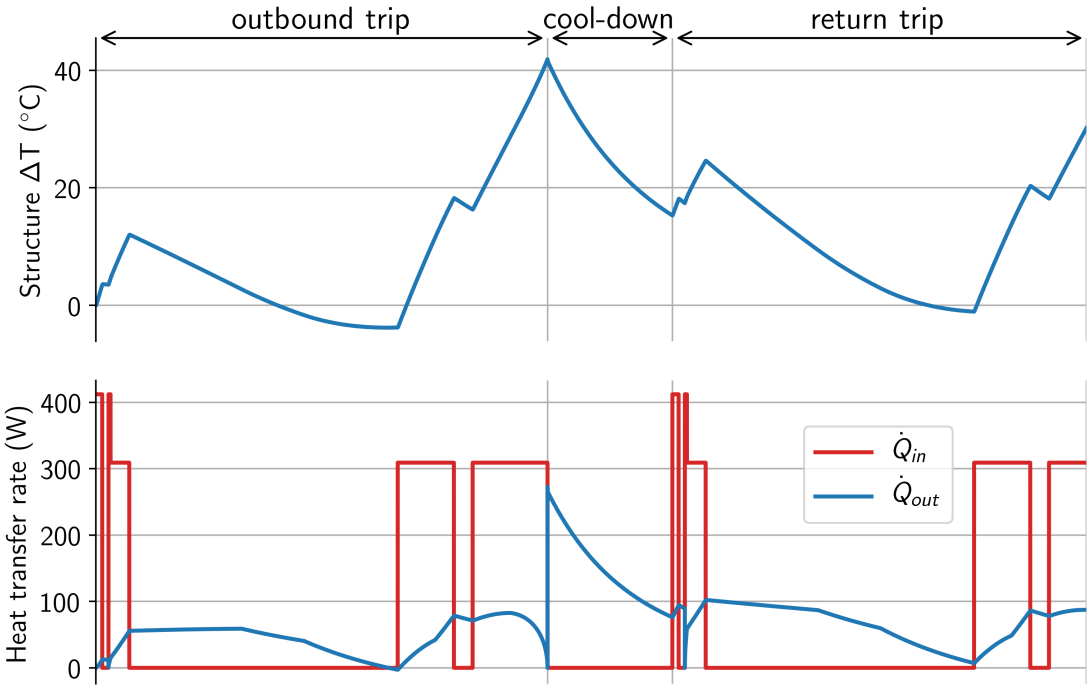

Figure 2.6: Round-trip trajectory thermal profile. The temperature of the structure over the course of the simulated trajectory is shown on the top, and the total heat flux in and out of the structure is shown on the bottom.

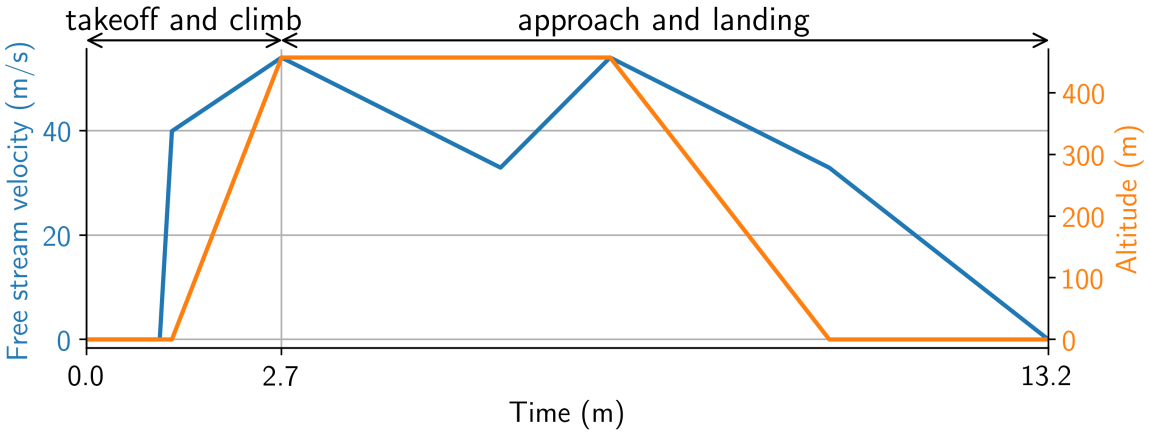

Figure 2.7: Diverted trajectory velocity and altitude profiles

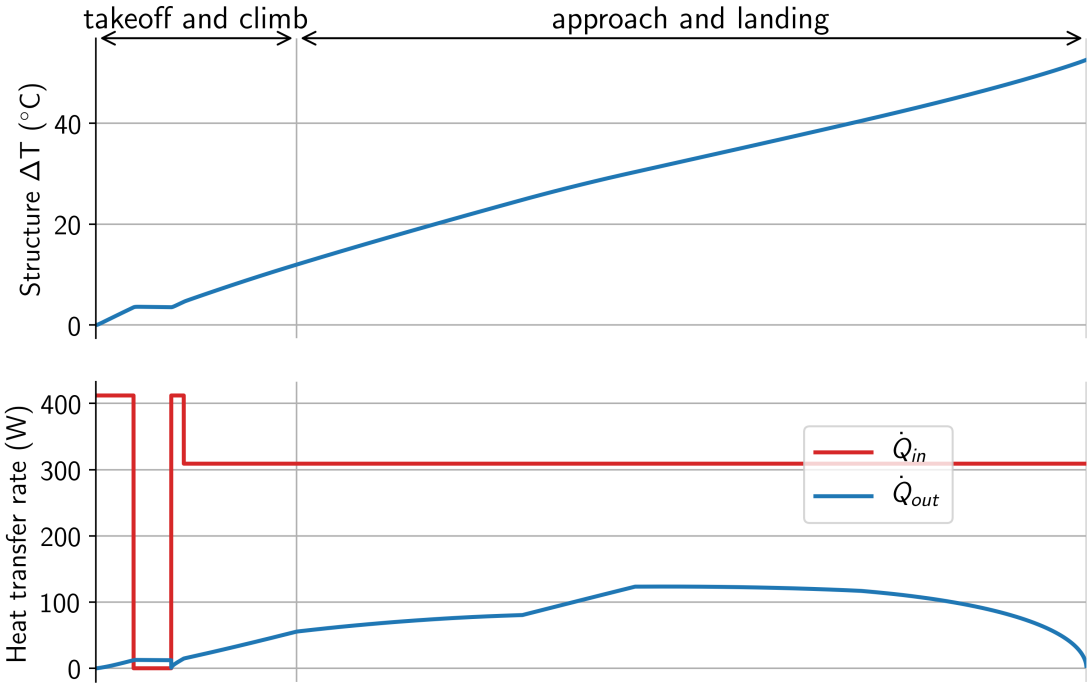

Figure 2.8: Diverted trajectory thermal profile. The temperature of the structure over the course of the simulated trajectory is shown on the top, and the total heat flux in and out of the structure is shown on the bottom.

Force Base, and are performed assuming a $35\ ^{\circ}\mathrm{C}$ day. A limitation of this model is the lumped-mass assumption. This is a reasonable assumption for the structure, because the walls are thin, but the heat transfer analysis of the motor would benefit from a more complex analysis. The motor is made of several materials and includes many different components that have different thermal properties, so a finer level of detail would resolve these differences. Despite the number of assumptions that were required, this type of lower-dimensional heat transfer analysis provides reasonable insight into the thermal requirements for structural design. In each of the full-flight trajectories presented here, the motor's enclosing structure is in a transient thermal state, due to the heat flux values which change frequently over the duration of the flight, necessitated by the operating requirements of the motor.

2.3 Conclusion

This chapter presented a simplified transient thermal model of the X-57 high-lift motor based on mission performance requirements, for three different scenarios. The rate of heat transferred into and out of the structure changes constantly over time, based on the varying power output required of the motor, as well as the fluctuating operating environment. Because of these constantly changing heat flux boundary conditions, the thermal state of the motor's housing structure never reaches a steady-state for any of the envisioned scenarios. These transient thermal loads can not be properly approximated by steady-state analysis. If maximum temperature were to be matched between steady-state and transient thermal analyses, the distribution of temperature would look completely different, leading to different optimized structural designs. The thermal analysis in this chapter demonstrates that steady-state thermal analysis is not sufficient for applications similar to this one which demand a transient thermal treatment.

CHAPTER 3

TOPOLOGY OPTIMIZATION FRAMEWORK

3.1 Topology optimization background

Generally speaking, the topology optimization process begins by defining a geometry or domain, and the forces and boundary conditions that are applied to the domain (Figure 1.1a). Next, this domain is discretized, or meshed, into many elements (Figure 1.1b). The topology optimization problem then seeks to determine whether material should be present (or not) in each of these elements, which determines the optimized design (Figure 1.1c). The final design depends on the problem formulation chosen, with the general form of Equation 1.1. The problem formulation minimizes some objective function (for example: minimize the mass, or minimize the maximum stress) subject to constraints on the design (for example: an upper bound on the mass or volume fraction, or a limit on maximum stress being below the yield stress), using the design variables[1] $x_i \in (0, 1]$ which define whether an element is "void" ($x_i = 0$) or "solid" ($x_i = 1$). Finally, the optimization problem is governed by the finite element equations because the objective and constraint values depend on the physics of the problem.

The design variables in this work are defined at the node locations and then interpolated from the nodes to the elements on the forest of a quadtree data structure. This interpolation can be expressed as

$$\boldsymbol{\xi} = \mathbf{F}\mathbf{x} \tag{3.1}$$

where $\mathbf{x} \in [\epsilon_0, 1]^{n_n}$ are the n_n nodal design variables with a lower bound of $\epsilon_0 = 10^{-6}$, $\boldsymbol{\xi} \in \mathbb{R}^{n_e}$ are the n_e interpolated element density values, and $\mathbf{F} \in \mathbb{R}^{n_e \times n_n}$ is the interpolation matrix from the nodal design variables to the element densities. The matrix $\mathbf{F}$

[1] In practice, a small, finite lower bound ϵ_0 is used on the design variables to avoid matrix-conditioning issues for the finite element problem.

varies depending on the type of design variable filter used. For the examples in chapter 4, a Lagrange filter is used, which uses a trilinear interpolation scheme to compute element densities from nodal design variables. Using this approach, the interpolation matrix $\mathbf{F}$ satisfies the partition of unity property.

For the examples in chapter 5 and chapter 6, the matrix $\mathbf{F}$ is an explicit filter matrix which approximates a Helmholtz partial differential equation (PDE) filter. The Helmholtz PDE is ideal for the basis of a implicit filter, since it introduces a length-scale and produces mesh-independent designs. However, two complications arise when using a Helmholtz PDE filter: first, a straightforward finite-element discretization of the Helmholtz PDE will not satisfy the discrete maximum principle and will therefore violate the positivity property on some meshes, and second, the linear system of equations must be solved to sufficient precision to obtain accurate and consistent gradient information.

An explicit filter matrix $\mathbf{F}$ that approximates the Helmholtz PDE filter and is also a partition-of-unity filter can be constructed as follows. This construction of the filter matrix ensures the discrete partition-of-unity property and can be used to obtain exact gradients without approximation.

A filter matrix of the form in (Equation 3.1) is a partition-of-unity filter if $\mathbf{F}$ satisfies two properties:

1. *Non-negativity:* The entries of $\mathbf{F}$ should be component-wise non-negative so that $F_{ij} \geq 0$.

2. *Sum-to-unity:* The rows of $\mathbf{F}$ should sum to unity such that $\mathbf{F}\mathbf{e} = \mathbf{e}$ where $\mathbf{e} \in \mathbb{R}^{n_n}$ is a vector of ones.

The partition of unity property is valuable since a constraint that the design variables lie on the unit interval $\mathbf{x} \in [0,1]^{n_n}$ results in a density field lying on the unit interval, $\boldsymbol{\xi} \in [0,1]^{n_e}$.

Consider the following implicit expression for the filter matrix

$$(\mathbf{D} - \mathbf{B})\boldsymbol{\xi} = \mathbf{x}$$

Here, $\mathbf{D} \in \mathbb{R}^{n_n \times n_e}$ is a diagonal matrix with positive entries on the diagonal $D_{ii} > 0$, and $\mathbf{B} \in \mathbb{R}^{n_n \times n_e}$ is a matrix of non-negative entries $B_{ij} \geq 0$. This non-negative requirement is imposed to ensure that the entries of the filter are positive.

Provided that the spectral radius of the matrix $\mathbf{D}^{-1}\mathbf{B}$ is strictly less than one, such that $\max_k |\lambda_k(\mathbf{D}^{-1}\mathbf{B})| < 1$, the implicit filter can be computed using the Neumann series inverse

$$\boldsymbol{\xi} = (\mathbf{I} - \mathbf{D}^{-1}\mathbf{B})^{-1}\mathbf{D}^{-1}\mathbf{x} = \sum_{k=0}^{\infty}(\mathbf{D}^{-1}\mathbf{B})^k\mathbf{D}^{-1}\mathbf{x}$$

This series may be truncated to contain $N + 1$ terms, to give the following explicit expression for the filter

$$\mathbf{F} = \mathbf{T}^{-1}\sum_{k=0}^{N}(\mathbf{D}^{-1}\mathbf{B})^k\mathbf{D}^{-1} \tag{3.2}$$

Here $\mathbf{T}$ is a diagonal matrix used to ensure the sum-to-unity property of the explicit filter so that

$$\mathbf{T} = \operatorname{diag}\left[\sum_{k=0}^{N}(\mathbf{D}^{-1}\mathbf{B})^k\right]\mathbf{D}^{-1}\mathbf{e}$$

With these definitions, the filter matrix $\mathbf{F}$ has all positive entries and retains the sum-to-unity property. As a result, the filter (Equation 3.2) is a discrete partition-of-unity filter.

The design variables $\mathbf{x}$ are represented as continuous variables in order to avoid solving a large combinatorial optimization problem. However, we desire discrete designs - with either solid or void elements - because intermediate design variables are not physically realizable. To do this, intermediate design variables are penalized. This is typically done through SIMP [2] or RAMP [94] penalization. With either approach, the element density

is determined by multiplying the material density with the element's design variable,

$$\rho_i = x_i \rho, \tag{3.3}$$

and the Young's modulus of the element is evaluated by multiplying an elemental weighting factor w_i by the Young's modulus of the material,

$$E_i = w(x_i) E. \tag{3.4}$$

For SIMP penalization, the element's weight is determined by

$$w(x_i) = x_i^P, \tag{3.5}$$

where P is the SIMP penalization value, and for RAMP penalization, the element's weight is computed as

$$w(x_i) = \frac{x_i}{1 + q(1 - x_i)}, \tag{3.6}$$

where q is the RAMP penalization value. The effect of RAMP penalization is shown in Figure 3.1 with a RAMP penalization value of $q = 8$. The stiffness-to-mass ratios are penalized for $x < 1$ so that intermediate materials are less desirable, ideally leading the optimizer to select values which are mostly either ~ 0 or ~ 1. RAMP penalization is used throughout this work.

3.2 Description of computational tools

All computational tools used for this work that are described in this section are open source[2]. Figure 3.2 illustrates the interaction between each of the computational tools used for topology optimization. First, the geometry used for topology optimization is created using EGADS [95] through the 'egads4py' interface. This geometry is imported into

[2]https://github.com/smdogroup

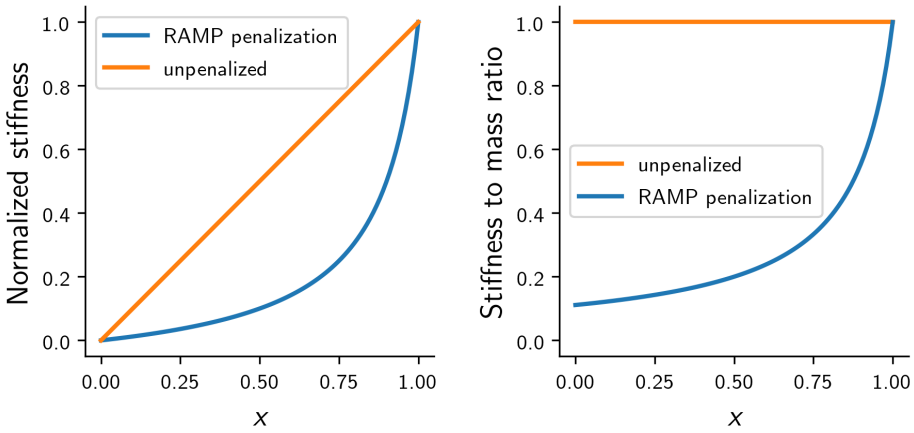

Figure 3.1: Effect of RAMP penalization. Normalized stiffness as a function of design variable value (left), and stiffness-to-mass ratio as a function of design variable value (right).

TMR [96], a parallel adaptive mesh generation tool, which meshes the geometry using a semi-structured quadtree or octree method. TMR is also used to define material properties, loads, and boundary conditions for the topology optimization problem. The mesh, material properties, loads and boundary conditions are then passed to TACS [97], an open-source parallel finite-element solver. In addition to solving the finite element system of equations, TACS computes the functions used for the objective and constraint values, and their gradients using the adjoint method. The total derivative of a function f can be expressed as

$$\frac{\mathrm{d}f}{\mathrm{d}\mathbf{x}} = \frac{\partial f}{\partial \mathbf{x}} + \frac{\partial f}{\partial \mathbf{u}} \frac{\mathrm{d}\mathbf{u}}{\mathrm{d}\mathbf{x}}. \tag{3.7}$$

The implicit component of the total derivative can be more easily obtained by differentiating the residual $\mathbf{R}(\mathbf{x}, \mathbf{u}) = 0$,

$$\frac{\mathrm{d}\mathbf{R}}{\mathrm{d}\mathbf{x}} = \frac{\partial \mathbf{R}}{\partial \mathbf{x}} + \frac{\partial \mathbf{R}}{\partial \mathbf{u}} \frac{\mathrm{d}\mathbf{u}}{\mathrm{d}\mathbf{x}} = 0, \tag{3.8}$$

and rearranging to obtain

$$\left[\frac{\partial \mathbf{R}}{\partial \mathbf{u}}\right] \frac{\mathrm{d}\mathbf{u}}{\mathrm{d}\mathbf{x}} = -\left[\frac{\partial \mathbf{R}}{\partial \mathbf{x}}\right]. \tag{3.9}$$

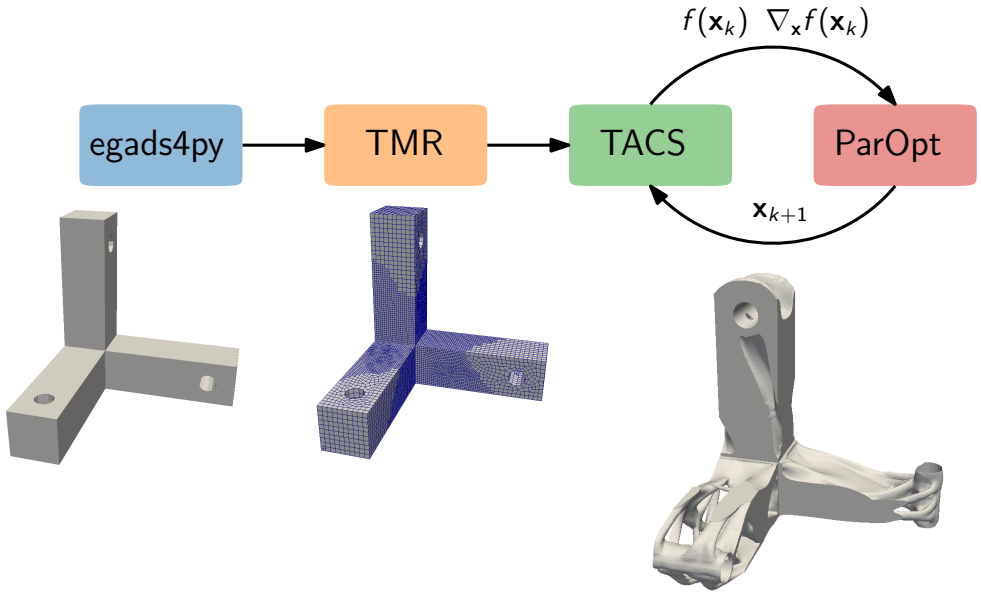

Figure 3.2: Diagram of computational tools during the topology optimization process

Incorporating this back into Equation 3.7 provides

$$\frac{\mathrm{d}f}{\mathrm{d}\mathbf{x}} = \frac{\partial f}{\partial \mathbf{x}} - \underbrace{\frac{\partial f}{\partial \mathbf{u}} \left[\frac{\mathrm{d}\mathbf{R}}{\mathrm{d}\mathbf{u}}\right]^{-1}}_{\boldsymbol{\psi}^T} \left[\frac{\mathrm{d}\mathbf{R}}{\mathrm{d}\mathbf{x}}\right], \tag{3.10}$$

where $\boldsymbol{\psi}$ is the adjoint vector. Using this adjoint approach results in an efficient solution of the total derivative, requiring only a single linear system solve for each function of interest - which in the context of structural optimization, are much fewer than the number of design variables.

The objective and constraint values and their corresponding gradients are then passed to ParOpt [96] for optimization. ParOpt solves for the update to the design variables, which are then passed back to TACS where the new objective, constraint, and gradient values are computed. This optimization loop iterates until a solution tolerance is satisfied or a maximum number of iterations is reached. After a fixed number of iterations, a new mesh will be generated by TMR using adaptive mesh refinement. TMR balances and repartitions the new mesh and the optimization loop resumes.

3.2.1 Mesh generation: TMR

TMR is a parallel adaptive mesh generation tool that is capable of efficiently meshing complex geometries with hundreds of millions of hexahedral elements using a semistructured octree method. These high-resolution meshes are created by first generating an initial coarse hexahedral mesh and subsequently refining the mesh using an octree on each coarse element [98, 99]. The initial coarse hexahedral volume mesh can be either generated in TMR using a swept-mesh method or taken as input from external hexahedral meshing tools. The swept-mesh technique results in a hexahedral mesh that is unstructured on the source and target faces, but structured in the swept direction [100]. The source quadrilateral mesh is generated using the Blossom-Quad algorithm [101]. This algorithm generates an even number of triangular elements, and then recombines triangles into quadrilaterals by computing an optimal pairing [102] based on a quality function for each possible quadrilateral. TMR uses the Blossom V implementation of the Blossom algorithm [103].

To demonstrate the capability of the mesh generation techniques in TMR, the hexahedron shape metric (first proposed by Knupp [104]) is plotted to evaluate the mesh quality. The shape metric is a scale-invariant value and ranges from 0 to 1, with the value 1 denoting a cube element and 0 denoting a degenerate element. Based on CUBIT [105], an automated mesh generation toolkit used in Sandia National Laboratories, elements with a shape metric value between 0.3 and 1 are considered to be good quality. Figure 3.3 shows the mesh quality metric for the orthogonal bracket presented subsection 4.3.2. The shape metric varies between 0.68 and 1, indicating that all the elements in the mesh are of good quality.

In order to mesh more complex geometries, I added the capability to TMR to import multiple coincident `step` files and combine the final meshes. Figure 3.4 illustrates this process. The left image of this figure shows a geometry decomposed into mesh-able bodies, with the final combined mesh shown in the center. The image on the right of this figure shows a battery housing geometry meshed using this approach, with a cutaway to show the

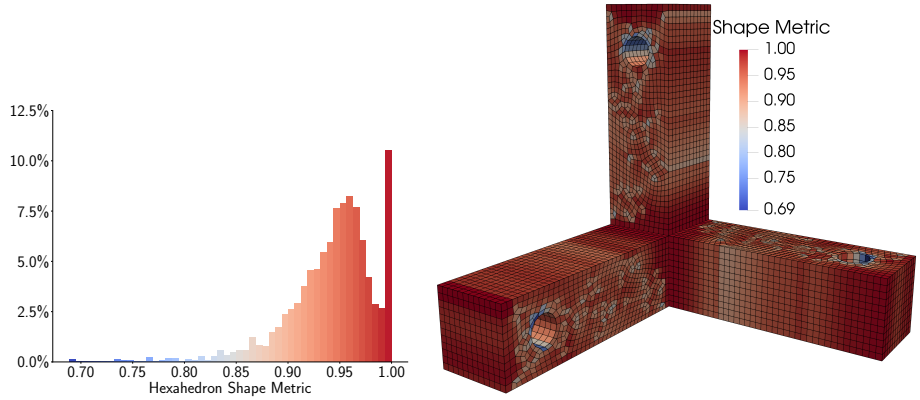

Figure 3.3: Mesh quality for the orthogonal bracket geometry

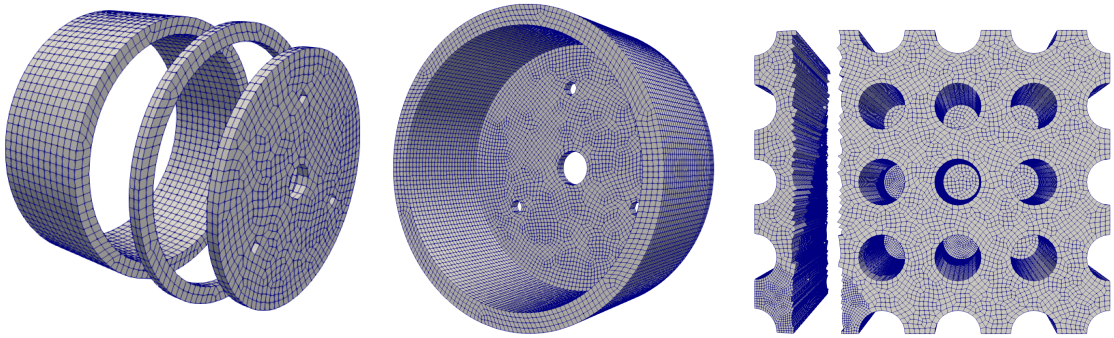

Figure 3.4: Geometry decomposition to mesh complex domains

internal elements.

A key benefit of using the quad/octree structure is the ability to adaptively refine the mesh as the design evolves during the topology optimization process. The optimization begins with a uniformly sized mesh, and as the design emerges, the mesh can be updated to improve the resolution of the design at a lower computational cost. In the literature there are several adaptive mesh refinement indicators that have been employed for topology optimization, such as feature-based methods [106], solution-based methods [107], and functional output-based methods [108]. The results in chapter 4 utilize a feature-based heuristic. With the feature-based adaptive refinement approach, elements are refined or coarsened based on the optimized material distribution.

For feature-based refinement, a simple heuristic is used which refines the mesh where the optimizer has placed material, and coarsens the mesh where the optimizer has allocated

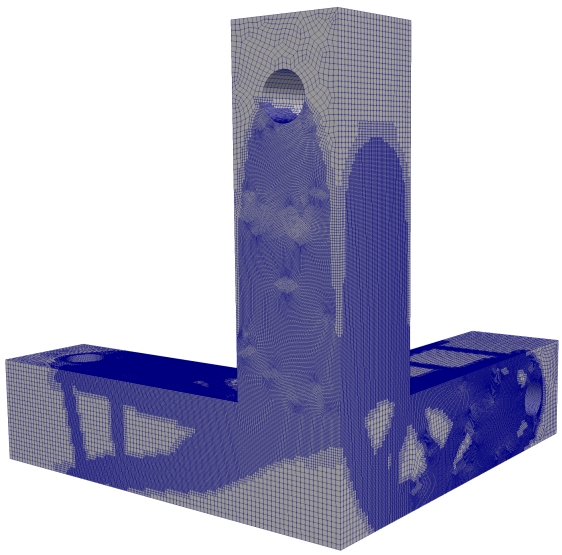

Figure 3.5: Example of adaptive mesh refinement

void. The parameter x_{rl} defines an upper limit on the void material, below which elements with nearly zero density are coarsened whenever $\rho_i \leq x_{rl}$. For the examples in chapter 4, a value of $x_{rl} = 0.05$ is used, so that elements which are nearly void are coarsened. The parameter x_{ru} defines a lower limit on the density, above which elements are refined. The examples in chapter 4 use a value of $x_{ru} = 0.25$, which refines the mesh in areas where there is either intermediate or converged solid material. After the mesh adaptation step is invoked, the design on the new mesh is interpolated from the previously optimized design using TMR. After the mesh is refined, the resulting meshes must be balanced, meaning that there is no more than one level of difference in refinement across edges or faces. The overall feature-based adaptive refinement heuristics used in this work is outlined in Algorithm 1. Figure 3.5 shows an example mesh after one step of adaptive mesh refinement.

Results in chapter 5 and chapter 6 use a different approach, where the mesh is refined along the solid-void boundary, which is computed through the solution of a Helmholtz equation. The mesh is correspondingly coarsened in regions which are completely void or completely solid, away from the solid-void interface. Elements which are completely solid don't need to be refined in order to improve the resolution of the design, so this Helmholtz-based approach allows a further reduction in computational cost compared to

Algorithm 1 Topology optimization with adaptive mesh refinement

Input: CAD geometry; initial mesh spacing
Generate initial analysis and design meshes in TMR
Optimize to obtain initial topology
while Termination criterion not satisfied **do**
    Identify elements to coarsen with filtered density $\rho_i \leq x_{rl}$
    Identify elements to refine with filtered density $\rho_i \geq x_{ru}$
    Regenerate the mesh in TMR based on updated refinement
    Interpolate design variables onto the new mesh
    Restart the topology optimization
end while

the feature-based approach.

3.2.2 Finite element analysis: TACS

The finite-element solver used in the topology optimization framework is TACS [97]. In this application, TACS uses a parallel geometric multigrid preconditioner with a Krylov subspace method to solve the structural governing equations. This approach is well suited to the elliptic governing equations [109]. Within the multigrid preconditioner, parallel block Gauss–Seidel relaxation is applied on each mesh level generated by TMR, while the linear system on the coarsest mesh is solved using a parallel direct solution method [97]. This preconditioner is similar to the method developed by Aage, Andreassen, and Lazarov [110] and Aage, Andreassen, Lazarov, and Sigmund [111], in that geometric multigrid is applied to the finest meshes, but differs in the application of a direct solution algorithm on the coarsest mesh. TACS is also used to evaluate quantities of interest, such as the structural mass, compliance or aggregated stress, and their derivatives using the adjoint method.

3.2.3 Optimization: ParOpt

ParOpt is a parallel optimizer that is designed for the large-scale optimization problems that arise in high-resolution topology optimization applications with $\mathcal{O}(10^8)$ design variables. ParOpt is implemented to handle the distributed design vectors that are encountered in

parallel topology optimization applications. ParOpt contains a number of optimization algorithms, including an interior-point method [112] and an Sℓ_1QP method with an ℓ_∞ trust-region globalization strategy [113]. In this work, the trust-region optimizer is used. The Sℓ_1QP method appends the inequality constraints as an ℓ_1 penalty function, using a smooth elastic-programming technique. The ℓ_∞ trust region constraint is enforced through bound constraints on the design variables. This quadratic optimization subproblem is solved using the interior-point method in ParOpt. Each iteration of the Sℓ_1QP method requires one evaluation of the objective and constraints and one evaluation of the objective and constraint gradients.

For topology optimization, an Sℓ_1QP Trust Region method is used, which is formulated to minimize the sum of a quadratic approximation and an ℓ_1 penalization of the constraint violation. This sub-optimization problem is subject to a trust region radius constraint on the step, and a bound constraint on the step. The Trust Region sub-problem is formulated as:

$$\begin{aligned} \min_{\mathbf{p}} \quad & h_k(\mathbf{p}) = f(\mathbf{x}_k) + \mathbf{g}_k^T\mathbf{p} + \frac{1}{2}\mathbf{p}^T\mathbf{B}_k\mathbf{p} + \gamma_k \left[\mathbf{c}(\mathbf{x}_k) + \mathbf{A}_k\mathbf{p}\right]_1 \\ \text{such that} \quad & \|\mathbf{p}\|_\infty \leq \Delta_k \\ & \mathbf{x}_k + \mathbf{p} \geq 0 \end{aligned} \tag{3.11}$$

The performance of this trust-region problem is sensitive to the penalty parameter γ_k; it must be larger than the Lagrange multiplier of the constraint ($\gamma > \lambda$) (which is generally not known prior to optimization), but a value too large would prohibit progress toward the solution. To alleviate this issue, this parameter can be updated adaptively with ParOpt. First, the subproblem is solved with a large γ (10^6), which provides a prediction of the greatest infeasibility reduction available. Next, a heuristic is used to increase or decrease γ based on feasibility and Lagrange multipliers. If the current point is feasible, and $\gamma > 2\lambda$, then γ is decreased using the damped scheme: $\gamma = \frac{1}{2}(\gamma + \lambda)$. If the current point is

infeasible, and the actual infeasibility reduction is less than 99.5% of the best infeasibility reduction available, then γ is increased by a factor of 1.5. The Sℓ_1QP trust region algorithm is outlined in detail in Algorithm 2.

Algorithm 2 Sℓ_1QP method with trust region globalization

Input: Initial design point $\mathbf{x}_1$ and initial trust region radius Δ_1
Set $k = 1$
while Optimality criteria not satisfied **do**
    Compute the candidate step $\mathbf{p}_k$ by solving Equation 3.11
    Evaluate the ratio $\hat{\rho}_k$ using Equation 3.13
    if $\hat{\rho}_k \geq \eta$ **then**
        Accept step $\mathbf{p}_k$ and set $\mathbf{x}_{k+1} = \mathbf{x}_k + \mathbf{p}_k$
    end if
    if $\hat{\rho}_k < \hat{\rho}_l$ **then**
        Set $\Delta_k = \max(\Delta_k/4, \Delta_{\min})$ ▷ Shrink the trust region
    else if $\hat{\rho}_k > \hat{\rho}_u$ **then**
        Set $\Delta_k = \min(2\Delta_k, \Delta_{\max})$ ▷ Expand the trust region
    else
        Set $\Delta_{k+1} = \Delta_k$ ▷ Keep the same trust region
    end if
    Update quasi-Newton Hessian approximation
    $k \leftarrow k + 1$
end while

Once a candidate step, $\mathbf{p}_k$, is computed as a solution of the quadratic optimization problem (Equation 3.11), its acceptance is based on the merit function

$$\phi_1(\mathbf{x}; \gamma_k) = f(\mathbf{x}) + \gamma_k \left[\mathbf{c}(\mathbf{x})\right]_1 , \tag{3.12}$$

and conventional trust region acceptance criteria [114]. The trust region update criteria are based on the ratio of the actual improvement in the merit function (Equation 3.12), to the improvement predicted by the model. This ratio, denoted $\hat{\rho}_k$, is defined as follows

$$\hat{\rho}_k = \frac{\phi_1(\mathbf{x}_k, \gamma_k) - \phi_1(\mathbf{x}_k + \mathbf{p}_k, \gamma_k)}{\phi_1(\mathbf{x}_k, \gamma_k) - h_k(\mathbf{p}_k)}. \tag{3.13}$$

Based on the value of $\hat{\rho}_k$, a candidate step is either accepted or rejected and the model

function h_k is improved through a quasi-Newton update procedure. The overall Sℓ_1QP trust region algorithm is shown in Algorithm 2. The acceptance of the step is governed by the criteria that it must make sufficient improvement such that $\hat{\rho}_k \geq \eta$ where the parameter takes a value of $\eta = 1/4$. The trust region radius is updated also based on the ratio $\hat{\rho}_k$ such that values below $\hat{\rho}_l = 1/4$ result in a decrease of the trust region radius, while values which are indicative of good progress exceeding $\hat{\rho}_u = 3/4$ result in an increase in the trust region radius.

CHAPTER 4

STRESS- AND FREQUENCY-CONSTRAINED TOPOLOGY OPTIMIZATION

4.1 Stress constraints

There are several factors which make maximum stress a challenging function to include in a topology optimization problem. First, there is a well-known stress-singularity issue that affects stress constraints in areas of vanishing density [62, 63, 64]. Throughout this work, the standard ϵ-relaxation approach [63, 64] is utilized to alleviate this issue. A local relaxed stress ratio in element i is defined as follows

$$s_r = \frac{\rho_i}{1 - \epsilon(1 - \rho_i)} \frac{\sigma_i}{\sigma_y}, \tag{4.1}$$

where ρ_i is the interpolated element density, σ_i is the von Mises stress in element i computed from the finite-element solution, σ_y is yield stress of the material, and ϵ is the stress relaxation parameter. A stress relaxation factor of $\epsilon = 0.1$ was used for all cases shown in this chapter. By construction, the relaxed stress ratio (Equation 4.1) vanishes as the local interpolated density vanishes, $\rho_i \to 0$, but achieves the full stress ratio at an interpolated density value of $\rho_i = 1$. Note that the relaxed stress ratio is a function of both the design variables and the finite-element state vector.

The second issue has to do with constraining a point-wise quantity. We want the maximum stress *anywhere* to be less than the yield stress, which if taken literally, would add one constraint per element to the optimization problem. This would be too computationally burdensome, so another approach is needed. Simply using a maximum function would not work either, because it is a non-differentiable function. Constraint aggregation alleviates both of these issues, by computing an approximate maximum of the function over the domain in a differentiable manner with only a single or a small number of constraints.

There are a few different approaches for constraint aggregation, including p-norm aggregation [20, 61, 64, 115], Kreisselmeier—Steinhauser (KS) aggregation [116, 117, 118], and Induced Exponential (IE) aggregation [117, 118, 119].

To bound the stress everywhere within the structure, we aggregate the relaxed stress ratio using a single KS aggregation functional [117, 120]. The aggregated stress constraint is formulated as

$$c_{\mathrm{KS}}(\mathbf{x}, \mathbf{u}; \rho_{\mathrm{KS}}) = s_r^{\max} + \frac{1}{\rho_{\mathrm{KS}}} \ln \left[\int_\Omega e^{\rho_{\mathrm{KS}}(s_r - s_r^{\max})} \mathrm{d}\Omega \right] \leq \beta, \tag{4.2}$$

where $c_{\mathrm{KS}}(\mathbf{x}, \mathbf{u}; \rho_{\mathrm{KS}})$ is the KS functional, $s_r^{\max}$ is the maximum relaxed stress ratio in the domain Ω, and ρ_{KS} is the KS parameter. The constraint (Equation 4.2) provides a smooth approximation of the maximum stress in the domain. The KS functional is used here, rather than the discrete KS function, which is non-conservative but exhibits mesh independence [117]. The use of the KS functional, instead of a discrete aggregate, ensures that the design problem formulation is consistent between meshes. The parameter β is chosen to be less than unity, due to the use of the non-conservative form of the KS functional, so that the resulting maximum stress is approximately equal to the yield stress. Typical values for β are between 0.5 to 0.7, depending on the value of the aggregation parameter, ρ_{KS}.

Stress-constrained topology optimization designs often exhibit mesh-sensitivity. This issue is more severe in stress-constrained problems compared to compliance design problems, since the local stress is predicted less accurately than the compliance. To address this challenge, the local stress is evaluated using an element-wise reconstruction. The advantage of the reconstruction technique is that it achieves a less mesh-sensitive estimate of the true value of the stress aggregate (Equation 4.2) than without reconstruction. While different reconstruction methods have been utilized by other authors [121, 122], in this work, the local element strain, and subsequently the stress, are evaluated based on a reconstruction of the displacement field within each element. This approach is designed to be simple to

implement and increases the smoothness of the constraint gradient. However, the proposed approach does not improve the asymptotic order of convergence of the stress aggregate itself. This deficiency, in most cases, is moot since the presence of stress singularities in the problem limits asymptotic accuracy. Although not addressed here, alternative schemes could be developed to preserve the invariance of the strain using C_1 elements [123].

The reconstruction technique proceeds by adding enrichment basis functions to fit the average displacement derivatives at the element nodes. This process is performed independently for each element, for each displacement component. For the x-component of the displacement, the enriched displacement field is interpolated as follows

$$u(\boldsymbol{\eta}) = \mathbf{N}(\boldsymbol{\eta})^T \mathbf{u}_e + \bar{\mathbf{N}}(\boldsymbol{\eta})^T \bar{\mathbf{u}}_e, \tag{4.3}$$

where $u(\boldsymbol{\eta}) \in \mathbb{R}$ is the interpolated displacement along the x-direction, $\boldsymbol{\eta} \in [-1, 1]^3$ are the coordinates in the computational domain, $\mathbf{N}(\boldsymbol{\eta}) \in \mathbb{R}^8$ are the element shape functions, $\mathbf{u}_e \in \mathbb{R}^8$ are the x-component of the displacement at each element node, and $\bar{\mathbf{u}}_e \in \mathbb{R}^9$, are the enriched displacements. The enrichment basis functions, $\bar{\mathbf{N}}(\boldsymbol{\eta})$, are zero at the element nodes so that the nodal displacement values are not modified. For a trilinear hexahedral element, 9 enrichment functions are utilized for the displacement along each coordinate direction, as described in Appendix section 8.1.

The process to obtain the element-wise enriched displacements requires two steps. First, the approximate spatial derivatives of the displacements at each node in the mesh are obtained by averaging the derivatives from all elements that touch that node. Next, on an element-by-element basis, the enriched displacements, $\bar{\mathbf{u}}_e$, are obtained by solving a least-squares problem which minimizes the ℓ_2 norm of the difference between the averaged derivatives at the nodes of each element, $\mathbf{u}_{e,x} \in \mathbb{R}^{24}$, and the derivatives obtained from the element-wise displacement (Equation 4.3). This least-squares problem can be written in terms of the two matrices, $\mathbf{A}_x \in \mathbb{R}^{24\times 8}$ and $\bar{\mathbf{A}}_x \in \mathbb{R}^{24\times 9}$, which give the derivative of

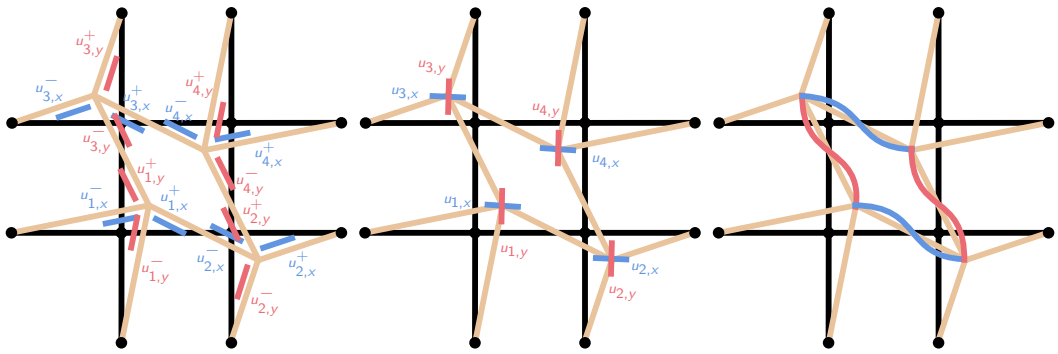

(a) Nodal displacement derivatives (b) Nodal displacement derivatives (c) Reconstructed displacement field

Figure 4.1: Reconstruction process

the displacement $u(\boldsymbol{\eta})$ along each coordinate direction at the nodes. These matrices are described in Appendix section 8.1. With these definitions, the least-squares problem can be written as

$$\min_{\bar{\mathbf{u}}_e} ||\mathbf{u}_{e,x} - \mathbf{A}_x\mathbf{u} - \bar{\mathbf{A}}_x\bar{\mathbf{u}}_e||_2. \tag{4.4}$$

The solution of the element-by-element problem (Equation 4.4) is

$$\bar{\mathbf{u}}_e = (\bar{\mathbf{A}}_x^T\bar{\mathbf{A}}_x)^{-1}\bar{\mathbf{A}}_x^T(\mathbf{u}_{e,x} - \mathbf{A}_x\mathbf{u}_e). \tag{4.5}$$

Note that the matrices, $\bar{\mathbf{A}}_x$ and $\mathbf{A}_x$, are independent of the displacement solution and only depend on the shape functions, the enrichment basis, and the geometry of the element.

Figure 4.1 illustrates the reconstruction process in two dimensions. Figure 4.1a shows a structured mesh in black and an associated displacement field in brown. The displacement derivatives at each node are denoted, $u^{+/-}_{i,x/y}$, with the subscripts indicating the node number and the direction of the derivative, and the superscript indicating whether the derivative is being taken from the positive or negative coordinate direction. Derivatives in the x-direction are shown in blue and derivatives in the y-direction are shown in red to indicate that the reconstruction process occurs simultaneously and independently in each direction. Figure 4.1b shows the averaged nodal displacement derivatives, $u_{i,x/y}$. These averaged

nodal derivatives are then used to compute the reconstructed displacement field shown in Figure 4.1c.

With the reconstruction, the derivative of the KS functional (Equation 4.3) with respect to element displacement involves the original nodal displacement values and contributions from the enriched displacement field

$$\frac{\mathrm{d}c_{\mathrm{KS}}}{\mathrm{d}\mathbf{u}_e} = \frac{\partial c_{\mathrm{KS}}}{\partial \epsilon_{ij}} \frac{\partial \epsilon_{ij}}{\partial \mathbf{u}_e} + \frac{\partial c_{\mathrm{KS}}}{\partial \epsilon_{ij}} \frac{\partial \epsilon_{ij}}{\partial \bar{\mathbf{u}}_e} \left(\frac{\partial \bar{\mathbf{u}}_e}{\partial \mathbf{u}_e} + \frac{\partial \bar{\mathbf{u}}_e}{\partial \mathbf{u}_{e,x}} \frac{\partial \mathbf{u}_{e,x}}{\partial \mathbf{u}_e} \right), \tag{4.6}$$

where ϵ_{ij} is the element strain. The two terms in (Equation 4.6) involving the enriched displacement components $\bar{\mathbf{u}}_e$ are functions of the terms from the least-squares reconstruction process and are computed as

$$\frac{\partial \bar{\mathbf{u}}_e}{\partial \mathbf{u}_e} = -(\bar{\mathbf{A}}_x^T \bar{\mathbf{A}}_x)^{-1} \bar{\mathbf{A}}_x^T \mathbf{A}_x, \tag{4.7}$$

$$\frac{\partial \bar{\mathbf{u}}_e}{\partial \mathbf{u}_{e,x}} = (\bar{\mathbf{A}}_x^T \bar{\mathbf{A}}_x)^{-1} \bar{\mathbf{A}}_x^T. \tag{4.8}$$

The derivative of the KS functional with respect to the finite-element solution vector is assembled from the contributions from each elements in the mesh.

4.1.1 Reconstruction demonstration and verification

To demonstrate the effect of this element-wise reconstruction, Figure 4.2 shows the von Mises stress field for a 3D crank problem using 8-node trilinear elements, with polynomial degree $p = 1$, and 27-node triquadratic elements, with polynomial degree $p = 2$, with and without computing the reconstruction. The von Mises stress obtained with reconstruction, $p = 1+$, is significantly smoother and exhibits better symmetry than the solution using trilinear shape functions with the standard approach, $p = 1$. The difference for the elements using triquadratic shape functions, $p = 2$ and $p = 2+$, is less significant but can still be observed near the areas of highest stress.

As a further verification of the stress constraint, Figure 4.3 shows the design obtained

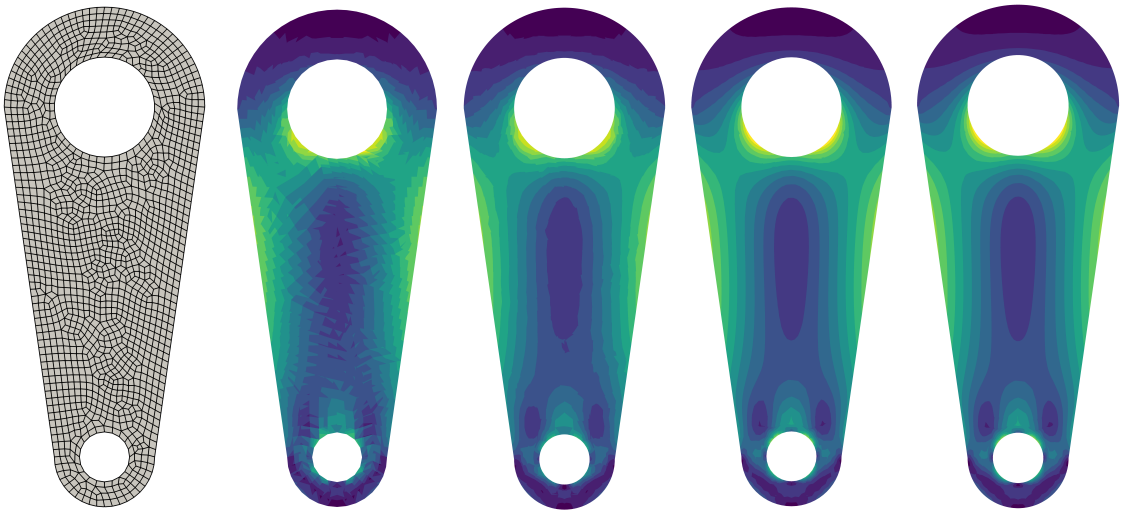

(a) Mesh (b) p = 1 (c) p = 1+ (d) p = 2 (e) p = 2+

Figure 4.2: Stress field comparison between solutions with and without reconstruction

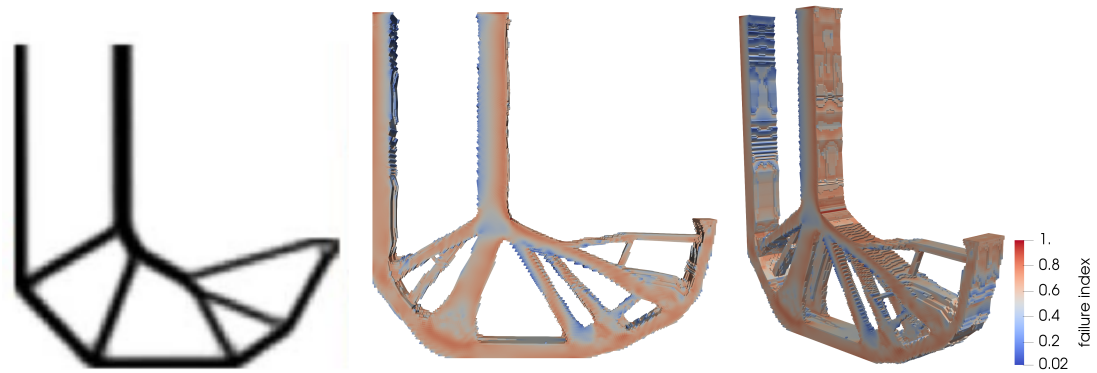

(a) Result from Le, Norato, Bruns, Ha, and Tortorelli [64]

(b) Solution using reconstruction

Figure 4.3: Validation against the 2D L-bracket problem

from the solution of a stress-constrained mass minimization problem using a 3D analogue of the 2D L-bracket problem presented by Le, Norato, Bruns, Ha, and Tortorelli [64]. While Le, Norato, Bruns, Ha, and Tortorelli obtained results using 2D plane stress elements, the results shown here utilize the proposed 3D reconstruction process. The domain of the 3D problem consists of the same in-plane dimensions as the 2D problem, while the out-of-plane thickness is increased from $1\ \mathrm{mm}$ in the original problem, to $10\ \mathrm{mm}$ in the 3D problem, to allow through-thickness topology to be resolved. To account for the increased depth of the domain, a $18\ \mathrm{N}$ load is applied over the upper $5\ \mathrm{mm}$ of the top corner of the horizontal member to produce the same force per unit depth as the original problem. To emulate the formulation of Le, Norato, Bruns, Ha, and Tortorelli [64], these results employ SIMP penalization with $P = 3$, but use the proposed KS aggregation with $\rho_{\mathrm{KS}} = 30$. Figure 4.3a shows the result from Le, Norato, Bruns, Ha, and Tortorelli [64], and Figure 4.3b shows the present result from two different views. Both the 2D and 3D designs share similarities with a deep rounded corner that avoids the re-entrant corner in the initial domain. However, the 3D topology has significant differences due to the ability to vary member dimensions in the through-thickness direction.

4.2 Frequency constraints

Finding the natural frequencies of vibration requires the solution of the generalized eigenvalue problem

$$\mathbf{K}(\mathbf{x})\mathbf{u}_i = \lambda_i \mathbf{M}(\mathbf{x})\mathbf{u}_i, \tag{4.9}$$

where λ_i is the eigenvalue and $\mathbf{u}_i$ is the corresponding eigenvector. Throughout the remainder of this section, the design vector arguments to the mass and stiffness matrices are omitted for simplicity.

In this work, the goal of natural frequency constraints is to bound the fundamental natural frequency from below by a specified value, so that all natural frequencies are greater

than or equal to a prescribed value ω_0. There are two primary challenges when imposing this type of frequency constraint within the context of a topology optimization problem: first, the mathematical issue of mode switching, which makes the eigenvalues locally non-differentiable [124], and second, the algorithmic issue of developing efficient and scalable eigenvalue solution procedures for large-scale problems. Mode switching occurs when the eigenmode associated with the lowest eigenvalue switches as the design evolves. At the cross-over point, the minimum eigenvalue is not differentiable [124]. Authors have addressed this issue using the bound formulation with modal assurance techniques [125, 126], or using p-norm or KS aggregation strategies [127]. In this work, the r-lowest eigenvalues, $\lambda_1 \leq \lambda_2 \leq \ldots \leq \lambda_r$, are KS-aggregated resulting in the following constraint

$$c_{\mathrm{KS}_\lambda}(\lambda_1, \ldots, \lambda_r; \rho_{\mathrm{KS}_\lambda}) = \lambda_1 - \frac{1}{\rho_{\mathrm{KS}_\lambda}} \ln \left[\sum_{i=1}^{r} e^{-\rho_{\mathrm{KS}_\lambda}(\lambda_i - \lambda_1)} \right] \geq \omega_0^2, \tag{4.10}$$

where $\rho_{\mathrm{KS}_\lambda} = 50$. This way, as long as the lowest eigenvalue is at all times due to one of the r-lowest modes, then KS-aggregation will identify the approximate lowest eigenvalue, and therefore eigenmode tracking is not required.

Evaluating the eigenvalue aggregate (Equation 4.10) requires the solution of a large-scale generalized eigenvalue problem. Many eigenvalue solution methods utilize direct factorization techniques, making them too computationally expensive for high-resolution topology optimization problems. In this work, a Jacobi–Davidson method [86] was developed to compute the eigenvalues of the natural frequency problem (Equation 4.9). This method leverages the scalable geometric multigrid preconditioner used in the Krylov solution method for the finite-element governing equations. To accelerate the eigenvalue solution procedure, two eigenvector recycling strategies are proposed, which utilize eigenvectors from the eigenproblem at the previous design iteration to provide an initial subspace. Eigenvector recycling has been used in the context of nonlinear eigenvalue problems [128], but have not been investigated in the context of topology optimization. Re-

cycling methods for the solution of linear systems have been demonstrated for topology optimization in the context of mass-constrained compliance minimization [129, 130], but not for eigenvalue problems. To compare the performance of the proposed method,the eigenproblem (Equation 4.9) is also solved using a conventional shift-and-invert Lanczos method [85].

4.2.1 Shift-and-invert Lanczos method

Shift-and-invert Lanczos techniques are commonly used in finite-element frequency and buckling analysis [85]. The shift-and-invert strategy preconditions the spectral properties of the eigenproblem (Equation 4.9) to promote separation of the eigenvalues close to a desired value, thereby accelerating the convergence of the Lanczos method. With a shift-and-invert strategy, the natural frequency eigenproblem (Equation 4.9) becomes

$$\mathbf{M}(\mathbf{K} - \sigma\mathbf{M})^{-1}\mathbf{M}\mathbf{u}_i = \mu_i \mathbf{M}\mathbf{u}_i, \tag{4.11}$$

where the transformed eigenvalues are $\mu_i = 1/(\lambda_i - \sigma)$ and the original eigenvalues that are close to the shift value σ become the extreme eigenvalues of the transformed eigenproblem. Shift-and-invert Lanczos methods have proven to be very effective when a full factorization of the matrix $\mathbf{K} - \sigma\mathbf{M}$ is available. However, for large-scale applications, a full factorization is not computationally feasible, and iterative solution methods are required instead. Unfortunately, shift-and-invert strategies require a tightly-converged solution for every application of the operator $(\mathbf{K} - \sigma\mathbf{M})^{-1}$, making them expensive when combined with iterative methods. In contrast, the Jacobi–Davidson method can be used with inexact solutions of a linear system without sacrificing the accuracy of the method.

4.2.2 Jacobi–Davidson method

The goal of the Jacobi–Davidson method is to find approximate solutions of the generalized eigenproblem (Equation 4.9) through an iterative technique that uses the Davidson approach of constructing an approximation to the eigenvector using an $\mathbf{M}$-orthogonal subspace, while using Jacobi's method to search for new vectors to add to this subspace [86]. A detailed description of the algorithm is shown in Appendix section 8.2 in Algorithm 3.

At iteration k, the Jacobi–Davidson method uses an $\mathbf{M}$-orthogonal subspace of dimension k, denoted $\mathbf{V}_k \in \mathbb{R}^{n \times k}$ that satisfies the property

$$\mathbf{V}_k^T \mathbf{M} \mathbf{V}_k = \mathbf{I}.$$

The approximate eigenvalues and eigenvectors, called the Ritz values and Ritz vectors, are written as $\lambda_i \approx \theta_i$, and $\mathbf{u}_i \approx \mathbf{V}_k \mathbf{y}_i$. The Ritz values and vectors are obtained by enforcing a Galerkin orthogonality condition leading to the reduced eigenproblem

$$\mathbf{V}_k^T \mathbf{K} \mathbf{V}_k \mathbf{y}_i = \theta_i \mathbf{V}_k^T \mathbf{M} \mathbf{V}_k \mathbf{y}_i.$$

Introducing the matrix $\mathbf{A}_k \triangleq \mathbf{V}_k^T \mathbf{K} \mathbf{V}_k \in \mathbb{R}^{k \times k}$, and applying the $\mathbf{M}$-orthogonality property, this problem can be simplified as

$$\mathbf{A}_k \mathbf{y}_i = \theta_i \mathbf{y}_i. \tag{4.12}$$

Since the dimension of the subspace is small, such that $k \ll n$, a solution method for small dense eigenproblems can be used to solve (Equation 4.12). The Ritz value and vector are approximations, so the residual $\mathbf{r}_i = (\mathbf{K} - \theta_i \mathbf{M}) \mathbf{V}_k \mathbf{y}_i$ is non-zero and an indicator of the accuracy of the approximation.

In the implementation of the Jacobi–Davidson method, for the first s iterations, we build $\mathbf{V}_k$ using recycled eigenvectors from previous eigenproblems. After this initial recycling

phase, the subspace $\mathbf{V}_k$ is built using vectors generated from an inexact Newton solution. To motivate the update scheme, consider the following Newton-step on the residuals of the i-th generalized eigenvalue appended with the $\mathbf{M}$-normality condition $\mathbf{u}_i^T\mathbf{M}\mathbf{u}_i = 1$

$$\begin{bmatrix} (\mathbf{K} - \theta_i\mathbf{M}) & \mathbf{M}\mathbf{u}_i \\ \mathbf{u}_i^T\mathbf{M} & 0 \end{bmatrix} \begin{bmatrix} \mathbf{t} \\ \Delta\lambda \end{bmatrix} = \begin{bmatrix} -(\mathbf{K} - \theta_i\mathbf{M})\mathbf{u}_i \\ \frac{1}{2}(\mathbf{u}_i^T\mathbf{M}\mathbf{u}_i - 1) \end{bmatrix} = \begin{bmatrix} -\mathbf{r}_i \\ 0 \end{bmatrix}, \tag{4.13}$$

which gives the update $(\mathbf{t}, \Delta\lambda)$ to the Ritz pair. Note that by construction the Ritz vector is in the span of the basis, $\mathbf{u}_i \in \text{span}\,\{\mathbf{V}_k\}$, and the residual is orthogonal to the basis such that $\mathbf{r}_i^T\mathbf{V}_k = 0$. As a result, the approximate eigenvector $\mathbf{u}_i$ satisfies

$$\mathbf{u}_i^T\mathbf{r}_i = 0.$$

As a consequence of this identity $(\mathbf{I} - \mathbf{M}\mathbf{u}_i\mathbf{u}_i^T)\mathbf{r}_i = \mathbf{r}_i$. The second condition in the linear system (Equation 4.13) imposes $\mathbf{u}_i^T\mathbf{M}\mathbf{t} = 0$ such that $\mathbf{t} = (\mathbf{I} - \mathbf{u}_i\mathbf{u}_i^T\mathbf{M})\mathbf{t}$. Combining these two results, the Newton update (Equation 4.13) can be written as

$$(\mathbf{I} - \mathbf{M}\mathbf{u}_i\mathbf{u}_i^T)(\mathbf{K} - \theta_i\mathbf{M})(\mathbf{I} - \mathbf{u}_i\mathbf{u}_i^T\mathbf{M})\mathbf{t} = -\mathbf{r}_i. \tag{4.14}$$

Instead of solving the update (Equation 4.14) to a tight tolerance, it can be beneficial to use a loose tolerance that requires fewer iterations. $\text{FGMRES}(m)$ is used to loosely solve (Equation 4.14) (with $m = 10$), where the geometric multigrid preconditioner is the same preconditioner used for the linear finite element solver.

4.2.3 Recycling methods for Jacobi–Davidson method

Since the proposed Jacobi–Davidson method is used in a design optimization process, it will be repeatedly applied to a sequence of related eigenproblems. In particular, the eigenvectors will exhibit similar characteristics between optimization iterations, and the differ-

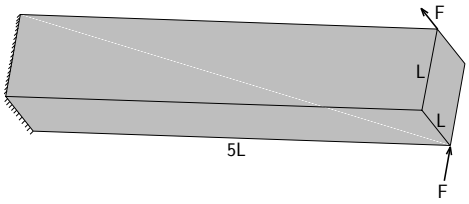

Figure 4.4: 3D cantilever beam with point loads

ence in the eigenvalues between iterations will converge to zero as the design converges. To take advantage of this property, the eigenvectors computed at the previous iterations can be recycled to accelerate the convergence of the next eigenproblem. The Jacobi–Davidson method is well suited to a variety of recycling strategies since the subspace vectors, $\mathbf{V}_k$, only need to be $\mathbf{M}$-orthogonal. An $\mathbf{M}$-orthogonal set of vectors can easily be obtained from any set of vectors by applying the modified Gram–Schmidt algorithm [131].

The recycling technique starts by constructing a set of an initial set of s vectors, stored as columns in $\mathbf{R}_s \in \mathbb{R}^{n\times s}$ that are computed from the eigenvectors obtained in the previous iteration. The following two strategies are examined: (1) one recycled vector, $s = 1$, that is an equally-weighted linear combination of the eigenvectors from the previous solution, and (2) a number of recycled eigenvectors, $s \leq r$, that are associated with the lowest eigenvalues from the previous solution. The first step in the recycling algorithm is to perform modified Gram–Schmidt to re-orthogonalize the set of recycled vectors and store them in the first s-columns of the basis $\mathbf{V}_k \in \mathbb{R}^{n\times k}$, with $k = s$. Next, the algorithm forms the portion of the $\mathbf{A}_k \in \mathbb{R}^{k\times k}$ matrix formed by $\mathbf{A}_k = \mathbf{V}_k^T\mathbf{K}\mathbf{V}_k$. Finally, the regular Jacobi–Davidson method is started from iteration $k = s$.

4.2.4 Performance of shift-and-invert Lanczos and Jacobi–Davidson

To quantify the benefits of the Jacobi–Davidson method over shift-and-invert Lanczos, a compliance-minimization study with mass and frequency constraints for a 3D beam problem is performed, with the results shown in Figure 4.4. The beam domain is $5\times 1\times 1$ and is discretized using two different mesh sizes, one having $32\times 32\times 160$ elements with $525,987$

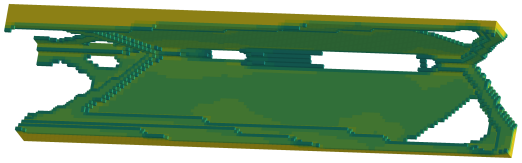

(a) Design obtained using 24 processors for mesh with $525,987$ degrees of freedom

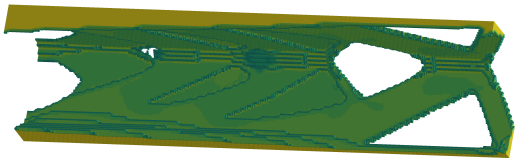

(b) Design obtained using 48 processors for mesh with 4 million degrees of freedom

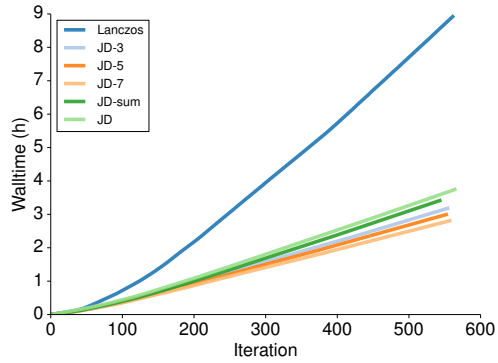

(c) Cumulative wall time using 24 processors for mesh with $525,987$ degrees of freedom

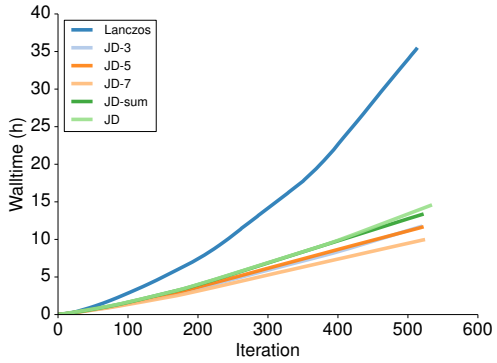

(d) Cumulative wall time using 48 processors for mesh with 4 million degrees of freedom

Figure 4.5: Design and wall time for the different methods on different mesh sizes

degrees of freedom and the other having $64 \times 64 \times 320$ elements with over 4 million degrees of freedom. The frequency constraint is evaluated by the shift-and-invert Lanczos or Jacobi–Davidson with different recycling strategies. The mass is constrained such that only 10% of the domain volume is occupied by material. The smaller mesh case was run on 24 processors, while the larger mesh case was run on 48 processors.

Figure 4.5 shows a summary of the topologies and computational times from this study. Figure 4.5c and Figure 4.5d show a comparison between between the total computational time using Lanczos and different variants of the Jacobi–Davidson for the small and large cases, respectively. For the smaller problem, the Jacobi–Davidson method required between 56 to 70% less computational time than the shift-and-invert Lanczos method. The larger problem exhibits similar time savings, with between 60 and 73% less computational time depending on the recycling strategy used for the Jacobi–Davidson method. The Jacobi–Davidson methods on both mesh sizes lie within the same performance range even as the design evolves. Without using recycling schemes, Jacobi–Davidson, denoted by JD,

does not perform as well as the JD variants that use recycling. This is expected since the method without recycling discards information about eigenvectors from the solution at the previous optimization iteration. The Jacobi–Davidson method that uses one recycled vector that is an equally-weighted linear combination of the eigenvectors from the previous solution, denoted by JD-sum, only outperformed the Jacobi–Davidson method without any recycling. Lastly, JD-s, where s is the lowest s eigenvectors recycled from the previous solution, demonstrated better performance as the number of eigenvectors recycled from the previous solution increases. In this example, $s = 3$, 5, and 7 eigenvectors were recycled out of 10 total eigenvectors. Recycling 7 eigenvectors performed the best, and resulted in a 28 to 33% reduction in computational time when compared to the Jacobi–Davidson method without any recycling. From this example, the benefits of the Jacobi–Davidson method with eigenvector recycling are clear, especially with high-resolution 3D structures.

4.3 Results

4.3.1 Problem formulations

In this section, three different topology optimization problem formulations are presented: (1) mass-constrained compliance minimization, (2) stress-constrained mass minimization, and (3) stress- and frequency-constrained mass minimization.

Mass-constrained compliance minimization

The mass-constrained compliance minimization problem is formulated as:

$$\begin{aligned} \min \quad & c(\mathbf{x}) = \mathbf{f}^T \mathbf{K}(\mathbf{x})^{-1} \mathbf{f} \\ \text{with respect to} \quad & \epsilon_0 \leq \mathbf{x} \leq 1 \\ \text{such that} \quad & m_{\text{fixed}} - m(\mathbf{x}) \geq 0 \\ \text{governed by} \quad & \mathbf{K}(\mathbf{x})\mathbf{u} = \mathbf{f} \end{aligned} \tag{4.15}$$

where $c(\mathbf{x})$ is the compliance of the structure, and $m(\mathbf{x})$ is the mass of the structure. The fixed mass value m_{fixed} is given by:

$$m_{\text{fixed}} = f_v V \rho \tag{4.16}$$

where f_v is the prescribed volume fraction, V is the total volume of the domain, and ρ is the density of the solid material.

Stress-constrained mass minimization

The mass minimization problem with stress constraints is formulated as:

$$\begin{aligned} \min \quad & m(\mathbf{x}) \\ \text{with respect to} \quad & \epsilon_0 \leq \mathbf{x} \leq 1 \\ \text{such that} \quad & c_{\text{KS}}\left(\mathbf{x}, \mathbf{u}\right) \leq \beta \\ \text{governed by} \quad & \mathbf{K}(\mathbf{x})\mathbf{u} = \mathbf{f} \end{aligned} \tag{4.17}$$

where β is a value chosen to be less than or equal to 1 to account for the non-conservative nature of the continuous KS functional.

Stress- and frequency-constrained mass minimization

The mass minimization problem with stress and frequency constraints is formulated as:

$$\begin{aligned} \min \quad & m(\mathbf{x}) \\ \text{with respect to} \quad & \epsilon_0 \leq \mathbf{x} \leq 1 \\ \text{such that} \quad & c_{\text{KS}}\left(\mathbf{x}, \mathbf{u}\right) \leq \beta \\ & c_{\text{KS}_\lambda}\left(\lambda_1, \ldots, \lambda_r\right) \geq \omega_0^2 \\ \text{governed by} \quad & \mathbf{K}(\mathbf{x})\mathbf{u} = \mathbf{f} \\ & \mathbf{K}(\mathbf{x})\mathbf{u}_i = \lambda_i \mathbf{M}(\mathbf{x})\mathbf{u}_i \end{aligned} \tag{4.18}$$

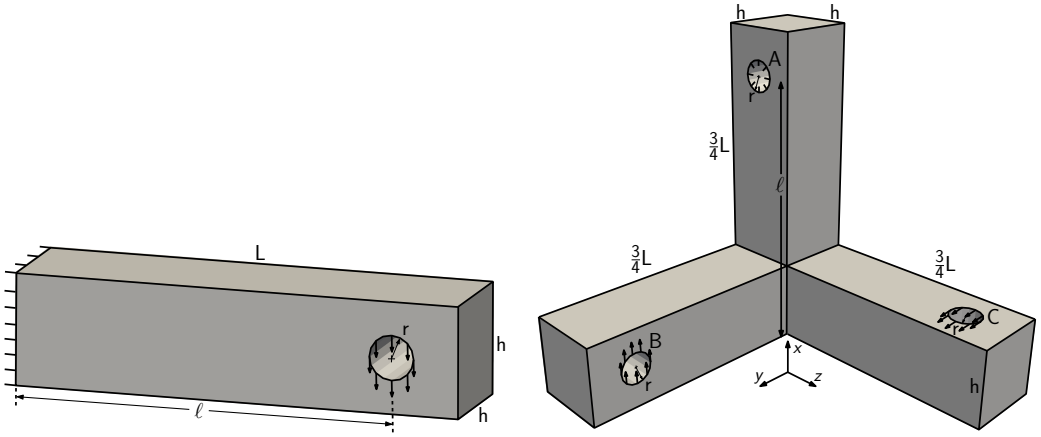

(a) Cantilever beam problem domain (b) Orthogonal bracket problem domain

Figure 4.6: Problem domains

The minimum allowable natural frequency, ω_0, is specified based on the problem domain.

4.3.2 Problem domains

Two problem domains (shown in Figure 4.6) are used to demonstrate the proposed stress- and frequency-constrained topology optimization methods. These problem domains consist of a cantilever beam and an orthogonal bracket. For all cases, aluminum is used as the design material with a density value of $\rho = 2,600 \text{ kg/m}^3$, a Young's modulus value of $E = 70 \text{ GPa}$, a Poisson's ratio of $\nu = 0.3$, and a yield stress value of $\sigma_y = 276 \text{ MPa}$.

Cantilever beam problem

Figure 4.6a shows a cantilevered beam with a hole cut out near the free end, with a downward traction applied throughout the hole. The geometry is nondimensional with values of $\ell/L = 0.85$, $h/L = 0.25$, and $r/L = 0.05$. We also define nondimensional load and frequencies so that these results can be replicated independent of scale.

For the cantilever beam problem, the maximum stress in the beam based on Euler–Bernoulli beam theory is

$$\sigma_{\max} = \frac{6F\ell}{h^3}. \tag{4.19}$$

Substituting the material yield stress σ_y for $\sigma_{\max}$ and rearranging, a normalized load, $\bar{F}$, can be defined as

$$\bar{F} = \frac{6F\ell}{\sigma_y h^3}. \tag{4.20}$$

Using dimensional analysis, we define a nondimensional natural frequency as

$$\bar{\omega}_0 = \omega_0 L\sqrt{\rho/E}. \tag{4.21}$$

For the cantilever beam problem, $\bar{F} = 0.54$ and $\bar{\omega}_0 = 0.3$ are the nondimensionalized load and frequency values used in the following cantilever beam examples.

Orthogonal bracket problem

Figure 4.6b shows the orthogonal bracket domain, with three beam members orthogonal to each other with holes cut near the free ends of each member. The holes are each cut in different orientations. Hole A at the top of the vertical member is completely clamped, while traction loads of equal magnitude are applied to holes B and C. This has the effect of creating a bending moment in each of the horizontal members, and a combined bending, torsional, and axial load in the vertical member. Here, nondimensional length ratios shown in the diagram below are $\ell/L = 0.85$, $h/L = 0.25$, and $r/L = 0.05$.

In order to scale the loads for the orthogonal bracket, we compute the maximum von Mises stress in the beam and compare this value to the material yield stress. Because both loads act at a distance on the vertical member, the maximum stress will occur near the cutout in the vertical member. The loads on the horizontal members result in equivalent moments M_x and M_z, and equivalent point loads F_y and F_x. The axial stress $\sigma_{11}(y, z)$ is computed from the contributions from both M_z and F_x as

$$\sigma_{11}(y,z) = \frac{F_x}{A} - y\frac{M_z + F_y\ell}{\frac{1}{12}h^4} = \frac{-F}{h^2}\left(1 + y\frac{24\ell}{h^2}\right).$$

Computing the shear stresses in the beam from torsion is challenging due to warping caused by the square cross section. To do this, we use the closed-form approximation from Bauchau and Craig [132, p. 285]

$$\sigma_{12}(y,z) = \frac{36F\ell}{h^3}\left[\left(\frac{y}{h}\right)^2 - \frac{1}{4}\right]\left(\frac{z}{h}\right),$$
$$\sigma_{13}(y,z) = \frac{-36F\ell}{h^3}\left(\frac{y}{h}\right)\left[\left(\frac{z}{h}\right)^2 - \frac{1}{4}\right].$$

There is an additional component of σ_{12} from the shear stress from F_y which is

$$\sigma_{12}(y,z) = \frac{3}{2}\frac{F}{h^2}\left(1 - \left(\frac{y}{h}\right)^2\right).$$

Computing an estimate of the maximum von Mises stress based on these stress components gives

$$\sigma_{\max} = \frac{F}{h^2}\sqrt{\frac{819}{2}\left(\frac{\ell}{h}\right)^2 + 48\left(\frac{\ell}{h}\right) + \frac{307}{32}}$$

Substituting σ_y for $\sigma_{\max}$ and rearranging results in the following expression for normalized load:

$$\bar{F} = \frac{F}{\sigma_y h^2}\sqrt{\frac{819}{2}\left(\frac{\ell}{h}\right)^2 + 48\left(\frac{\ell}{h}\right) + \frac{307}{32}} \tag{4.22}$$

The nondimensional expression for the frequency (Equation 4.21) from the cantilever beam case is applied again here. For the orthogonal bracket problem, $\bar{F} = 1.0$ and $\bar{\omega}_0 = 0.18$ are the nondimensionalized load and frequency values used in the following orthogonal beam examples.

4.3.3 Topology optimization results

Reconstruction and stress constraint comparison

Before examining the full set of results, we first study the effect of the reconstruction technique presented in section 4.1 on the optimized designs. For this study, the cantilever

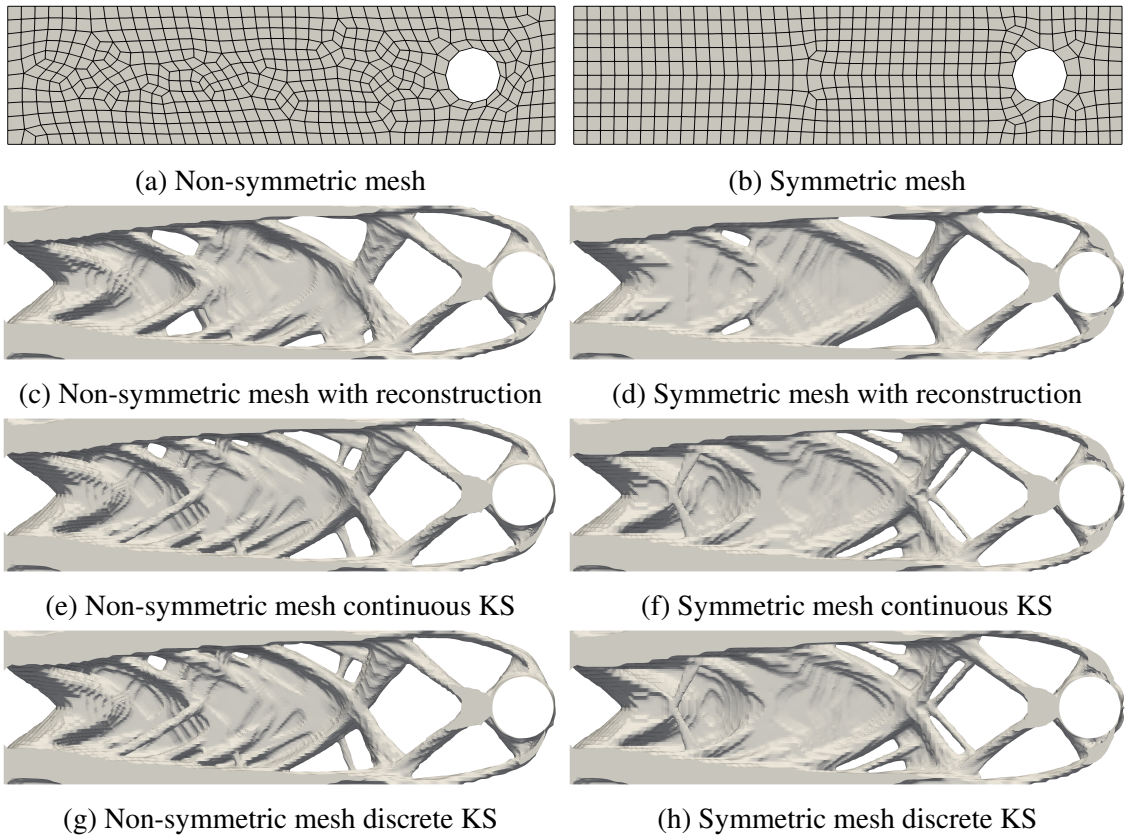

(a) Non-symmetric mesh (b) Symmetric mesh

(c) Non-symmetric mesh with reconstruction (d) Symmetric mesh with reconstruction

(e) Non-symmetric mesh continuous KS (f) Symmetric mesh continuous KS

(g) Non-symmetric mesh discrete KS (h) Symmetric mesh discrete KS

Figure 4.7: Stress constrained topology optimization results using different techniques to evaluate the stress constraint. The left column shows results generated on a non-symmetric mesh, while the right column shows results using a symmetric mesh. The top row shows each mesh, the second row uses stress reconstruction with the continuous KS functional, the third row uses the KS functional without stress reconstruction, and the bottom row uses the discrete KS function without stress reconstruction.

Table 4.1: Problem data for the cantilever beam stress constraint comparison

Problem/mesh type	Elements	DOF	q
Reconstruction/symm.	8,101,863	23,722,908	5
Continuous KS/symm.	8,056,188	23,586,873	5
Discrete KS/symm.	8,072,498	23,631,708	5
Reconstruction/non-symm.	9,330,720	27,328,236	5
Continuous KS/non-symm.	9,171,624	26,872,533	5
Discrete KS/non-symm.	9,155,328	26,824,899	5

Table 4.2: Optimization result data from the cantilever beam stress constraint comparison

Problem/mesh type	$m\%$	infeas.	ℓ_∞	Time (h)
Reconstruction/symm.	34.95%	2.6×10^{-5}	7.3×10^{-3}	8.5
Continuous KS/symm.	35.15%	1.4×10^{-6}	2.0×10^{-3}	7.7
Discrete KS/symm.	34.87%	1.9×10^{-5}	4.3×10^{-3}	7.6
Reconstruction/non-symm.	35.19%	2.1×10^{-5}	2.7×10^{-3}	9.5
Continuous KS/non-symm.	34.90%	2.2×10^{-5}	4.6×10^{-3}	10.1
Discrete KS/non-symm.	34.37%	6.2×10^{-7}	2.2×10^{-3}	10.2

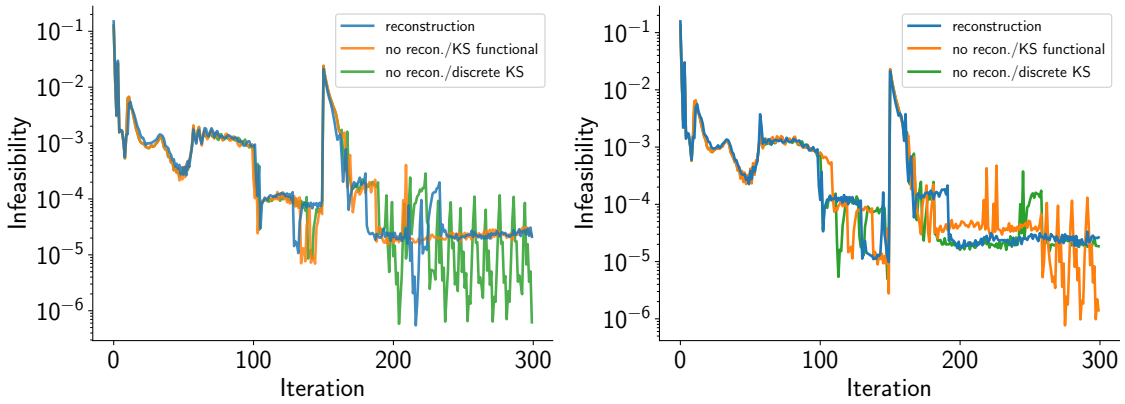

(a) Infeasibility for non-symmetric meshes

(b) Infeasibility for symmetric meshes

Figure 4.8: Infeasibility history for stress constrained topology using different techniques to evaluate the stress constraint. The left column shows results generated on a non-symmetric mesh, while the right column shows results using a symmetric mesh.

domain is used to compare designs obtained from stress-constrained mass minimization using the reconstruction with designs obtained without reconstruction, using both the KS functional and the discrete KS function. Additionally, the effect of using a non-symmetric or symmetric mesh are shown in Figure 4.7a and Figure 4.7b, respectively. Note that twice uniformly coarsened versions of the full finite-element meshes are shown for clarity.

In each case, the optimization utilizes one cycle of adaptive mesh refinement, with 150 optimization iterations on the initial mesh, and 150 iterations on the refined mesh. Each case was run on 72 processor cores. Table 4.1 provides the final mesh sizes and penalty values used for each problem, and Table 4.2 summarizes the results for each optimization, including optimized mass, optimization convergence, and computation cost. Note that in all cases, the final volume fraction of structure is within 1% while the symmetric and non-

symmetric cases with reconstruction are within 0.25%. Figure 4.8 shows the history of the infeasibility for each problem on a log-scale, where the non-symmetric results are shown in Figure 4.8a, and the symmetric results are shown in Figure 4.8b. All convergence histories share similar infeasibility behavior, with a large jump in the infeasibility after the adaptive refinement step. Figure 4.7 shows the optimized designs for each case, where Figure 4.7c, Figure 4.7e, and Figure 4.7g show the non-symmetric results, and Figure 4.7d, Figure 4.7f, and Figure 4.7h show the symmetric results. Figure 4.7c and Figure 4.7d show the solutions when stress reconstruction is used, Figure 4.7e and Figure 4.7f shows the cases where no reconstruction is used and the stress constraint is evaluated using the KS functional, and Figure 4.7g and Figure 4.7h show the solutions without reconstruction, where the discrete KS function is used to evaluate the stress constraints. Overall the designs share many similarities with a top and bottom flange and web-like structure which transitions to an open truss at the load application point. The designs that employ reconstruction have a more consolidated geometry with fewer, thicker members, while the designs without reconstruction have more numerous slender members. These differences can be attributed to the reconstruction technique predicting higher stress in slender elements represented by fewer finite-elements. The primary difference between the symmetric and non-symmetric designs with reconstruction in Figure 4.7d and Figure 4.7c, respectively, is the additional attachment point between the lower flange and web structure at about 70% of the length from the root in the non-symmetric result. Unlike the other web attachment points, this additional feature does not span the entire width of the web but is attached symmetrically on either side about the width. The single side view of the topology over-emphasizes the asymmetry in this case.

Cantilever beam results

Figure 4.9, Figure 4.10, and Figure 4.11 show the results for the compliance, stress-constrained, and stress- and frequency-constrained problems, respectively for the cantilever beam do-

main. For each problem, a top view, a side view, and a rear view from the cantilevered end are provided. Each of these problems uses one cycle of adaptive mesh refinement, resulting in a mesh size between 13.4 and 14.3 million elements, and between 40.1 and 42.7 million degrees of freedom (DOF), depending on the problem. Each problem is solved on the same initial mesh for a fixed 500 iterations, and then adaptive mesh refinement is performed, and then the optimization proceeds for another fixed 500 iterations. The adaptation step produces a new design mesh and associated design parametrization. The old design point is interpolated to the new design space and all other optimization parameters are retained. A fixed number of iterations is used since tight convergence cannot be achieved for these large-scale design problems within a reasonable computational budget. However, as can be seen in Table 4.4, each solution finds a feasible point, with the infeasibility less than 4.2×10^{-5} in each case presented. The ℓ_∞ norm of the optimality error is in each case is less than 5.4×10^{-3}, indicating a converged solution.

As a first step, the stress-constrained mass minimization problem is solved, resulting in a structure with a mass fraction of 34.9% and a maximum stress of 103% of the yield stress. This small stress violation is due to the non-conservative nature of the KS functional itself, not due to a constraint violation in the optimization problem. Next, the conventional mass-constrained compliance minimization problem is solved with the mass fraction constrained to 35%, selected based on the stress-constrained result. Finally, the stress- and frequency-constrained mass minimization problem is solved with the lowest nondimensionalized natural frequency constrained to be greater than a value of $\bar{\omega}_0 = 0.3$. The resulting structure has a mass fraction of 34.4%, a maximum stress of 102% of the yield stress, and a nondimensionalized first natural frequency of $\bar{\omega}_1 = 0.46$. Interestingly, the frequency constraint is not active at the final design point. Once the frequency constraint is satisfied, the optimizer finds a design to minimize the stress that coincidentally has a higher minimum natural frequency than the constraint value. The frequency constraint still had a significant impact on the design, without being active at the final optimization iteration.

Table 4.3: Problem data for the cantilever beam domain

Problem	Elements	DOF	q
Compliance	14,350,202	42,738,516	10, 10
Stress	14,068,319	41,534,952	8, 10
Stress & freq.	13,401,506	40,108,296	8, 10

Table 4.4: Optimization result data for the cantilever beam domain

Problem	$m\%$	infeas.	ℓ_∞	$\sigma_{\max}/\sigma_y$	$\bar{\omega}_0$	Time (h)
Compliance	35%	0	1.4×10^{-4}	—	—	16.1
Stress	34.9%	1.5×10^{-5}	3.2×10^{-3}	1.03	—	63.3
Stress & freq.	34.4%	4.2×10^{-5}	5.4×10^{-3}	1.02	0.3	202.2

Table 4.3 provides the problem data for the cantilever beam, including problem size, and values of the RAMP penalization, and Table 4.4 summarizes the results and computation cost. Note that the two values of the RAMP penalization indicate the value used on the initial mesh, followed by the value used on the mesh after adaptive mesh refinement is performed. Each case is run on 72 processor cores for a total of 1000 iterations.

The stress-constrained result, in Figure 4.10, and the compliance minimization result, in Figure 4.9, both form structures which resemble I-beams. However, the compliance minimization result and the frequency constrained result, shown in Figure 4.11, form closed boxes. The stress- and frequency-constrained result has features resembling both the compliance based design and the stress based design. This is intuitive since compliance minimization is equivalent to stiffness maximization, and stiffer structures generally have higher natural frequencies for the same mass. Applying stress and frequency constraints can then be thought of as increasing the stiffness of the structure while enforcing stress constraints.

Figure 4.9: Top, side, and rear views of the mass-constrained compliance minimization result for the cantilever beam problem

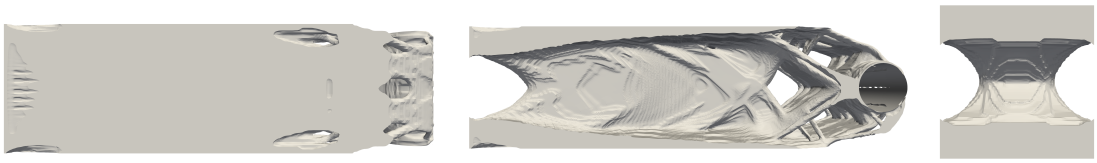

Figure 4.10: Top, side, and rear views of the stress-constrained mass minimization result for the cantilever beam problem

Figure 4.11: Top, side, and rear views of the stress- and frequency-constrained mass minimization result for the cantilever beam problem

Note that the web structures formed in the stress-constrained case and in the compliance minimization case are hollow inside.

Figure 4.12, Figure 4.13, and Figure 4.14 show the material failure ratio for the compliance, stress-constrained, and stress- and frequency-constrained problems, respectively, with the topology side-by-side for reference. The stress-constrained mass minimization result is almost uniformly stressed everywhere. The compliance minimization case shows high stress concentrations at the top and bottom of the flange of the beam near the root. The stress- and frequency-constrained mass minimization case shows a region near the root of the beam along the sides with low stress.

Figure 4.15a shows the history of the stress and frequency constraints during the design. The constraint ratio is the ratio of the constraint value to the design limit, which for feasible

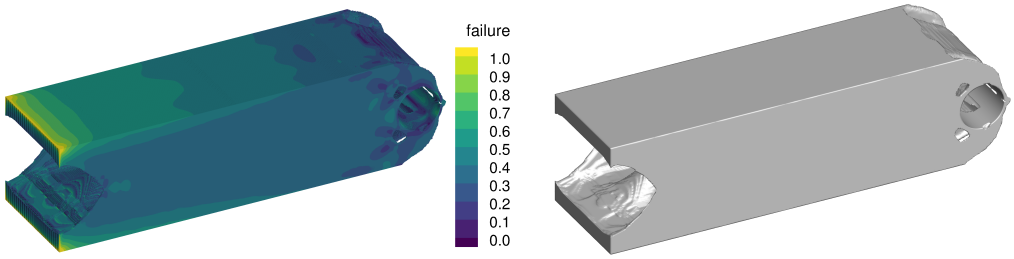

Figure 4.12: Failure (left) and topology (right) for the mass-constrained compliance minimization case of the cantilever beam problem

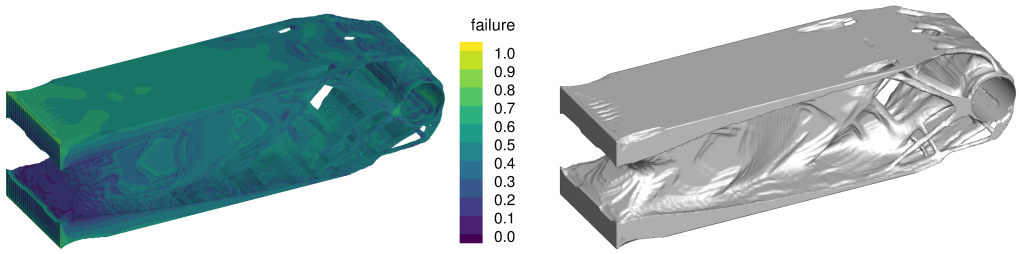

Figure 4.13: Failure (left) and topology (right) for the stress-constrained mass minimization case of the cantilever beam problem

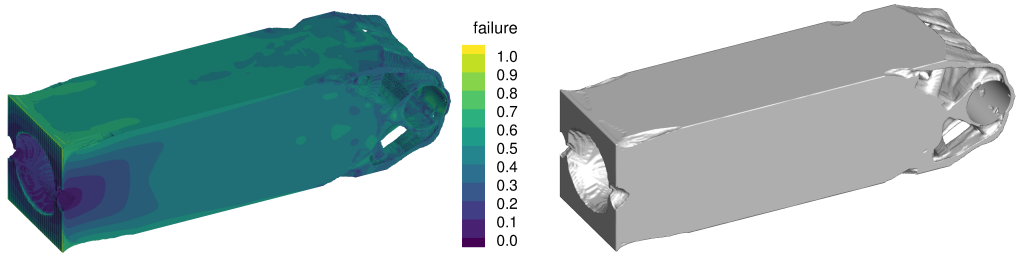

Figure 4.14: Failure (left) and topology (right) for the stress- and frequency-constrained mass minimization case of the cantilever beam problem

designs, should be less than or equal to one for stress, and greater than or equal to one for frequency. The optimizer quickly satisfies both the stress and frequency constraints, but once the frequency constraint is satisfied, the first eigenvalue continues to increase, and the optimizer is then only concerned with finding the minimum mass solution which satisfies the stress constraint. Even though it is inactive during much of the design optimization, the frequency constraint has the effect of closing off a portion of the design space where the stress-constrained minimum mass solution existed, resulting in a different topology. Also note that the sudden change in the constraint values at 500 iterations occurs due to the application of adaptive mesh refinement at that steps.

Figure 4.15b shows the optimization history of the mass and the infeasibility, with designs highlighted at 35, 100, 500, and 1000 iterations. The design quickly becomes feasible at iteration 36. By iteration 100, the design has largely converged, and changes after this point are relatively minor. The design becomes infeasible again after the adaptive mesh refinement step, but quickly recovers to a feasible point. Figure 4.16 shows the

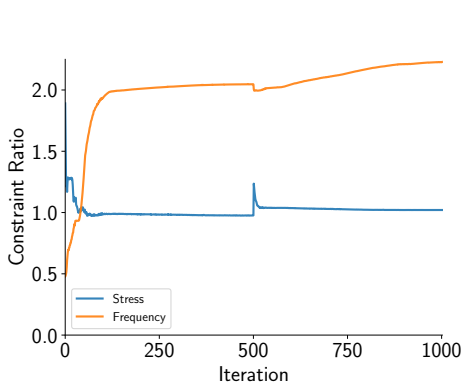

(a) Convergence of stress and frequency constraints

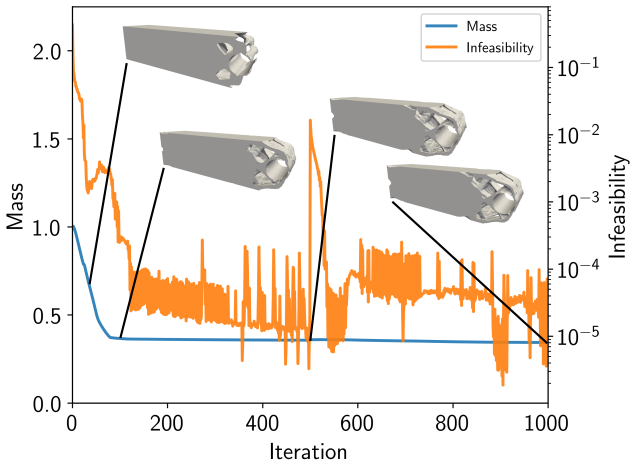

(b) History of objective and infeasibility

Figure 4.15: Optimization history of cantilever beam problem

history of the first six beam eigenvalues as the design evolved. Initially, the first two natural frequencies, ω_1 and ω_2, are repeated, but over the course of the optimization they spread out and become distinct by the final design. In addition, at the initial design point, ω_4 and ω_5 are repeated natural frequencies, while ω_3 and ω_6 are well-separated. At the final design point the gap between the frequencies ω_3 and ω_4 as well as ω_5 and ω_6 is small. The normalized natural frequencies at the final design point take values of $\bar{\omega}_1 = 0.46$, $\bar{\omega}_2 = 0.49$, $\bar{\omega}_3 = 1.12$, $\bar{\omega}_4 = 1.15$, $\bar{\omega}_5 = 1.35$, and $\bar{\omega}_6 = 1.38$, respectively.

Orthogonal bracket results

Figure 4.17, Figure 4.18, and Figure 4.19 show the results for the compliance, stress-constrained, and stress- and frequency-constrained problems, respectively, for the orthogonal bracket domain. Two views are provided: an isometric view, and a view from the top, looking down from the perspective of the vertical member. Again, one cycle of adaptive mesh refinement was used, resulting in meshes with between 4.7 and 5.3 million elements and between 14.1 and 16 million degrees of freedom.

As a first step, the stress-constrained mass minimization problem is solved, resulting in a structure with a mass fraction of 37.1% and a maximum stress at 99% of the yield

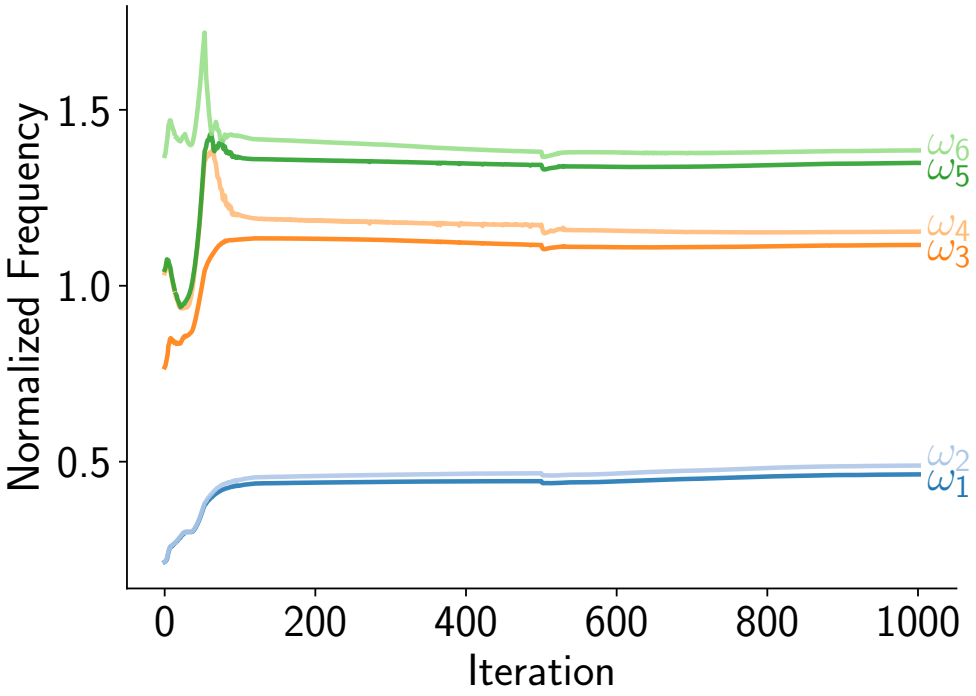

Figure 4.16: History of beam natural frequencies

stress. Next, the mass-constrained compliance minimization problem is solved with the mass fraction constrained to 40% in order for the result to be comparable to the mass minimization problem. Finally, the stress- and frequency-constrained mass minimization problem is solved with a minimum normalized first natural frequency value of $\bar{\omega}_0 = 0.18$. The resulting structure has a mass fraction of 41.9%, with a maximum stress of 98% of the yield stress, and a normalized first natural frequency value of $\bar{\omega}_1 = 0.19$. In this case, the frequency constraint is active at the final design point. Table 4.5 provides the problem data for the orthogonal bracket, including problem size, and values of the RAMP penalization, and Table 4.6 summarizes the results, and computation cost. Note that the two values of the RAMP penalization indicate the value used on the initial mesh, and the value used on the adaptively refined mesh. Each case is run on 48 processor cores with the same initial mesh for the first 500 optimization iterations, and then another 500 iterations on the adaptively refined mesh. Table 4.6 shows that each case achieves an infeasibility less than 3.8×10^{-4}, and an ℓ_∞ optimality error of less than 1.4×10^{-2}.

Figure 4.17: Isometric and top views of the mass-constrained compliance minimization result for the orthogonal bracket problem

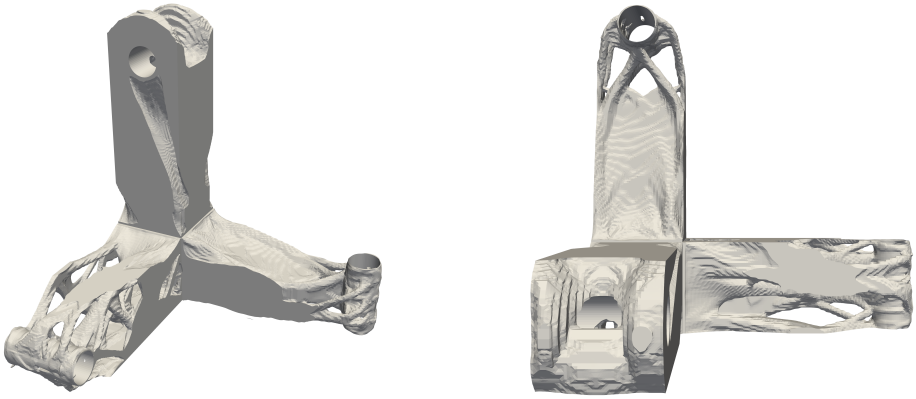

Figure 4.18: Isometric and top views of the stress-constrained mass minimization result for the orthogonal bracket problem

Comparing the resulting topology of each problem, the stress-constrained case has a more open-section design, while the compliance minimization case is the most closed-off. For the case with stress and frequency constraints, there are more closed sections than the stress-constrained case, but fewer than the compliance minimization case. Again, there are strong similarities between the stress- and frequency-constrained results and both the stress-based and the compliance-based results.

Figure 4.20 shows the material failure ratio for each result for the orthogonal bracket domain. In each case, the maximum stress ratio is achieved at both the hole at the top, which is fully restrained, and near the reentrant corners of the original domain. The stress-constrained designs reduce these maximum stresses compared to the compliance minimiza-

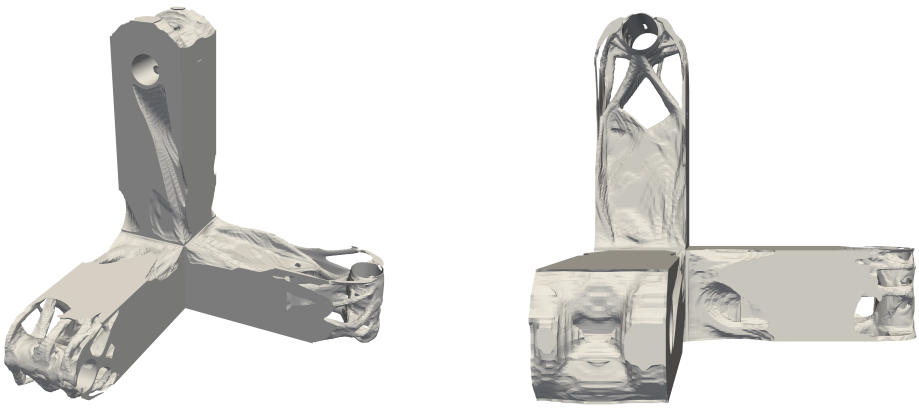

Figure 4.19: Isometric and top views of the stress- and frequency-constrained mass minimization result for the orthogonal bracket problem

Table 4.5: Problem data for the orthogonal bracket domain

Problem	Elements	DOF	q
Compliance	5,045,912	15,005,418	10, 10
Stress	4,758,457	14,078,607	8, 10
Stress & freq.	5,356,033	16,005,678	10, 10

Table 4.6: Optimization result data for the orthogonal bracket domain

Problem	$m\%$	infeas.	ℓ_∞	$\sigma_{\max}/\sigma_y$	$\bar{\omega}_0$	Time (h)
Compliance	40%	0	1.4×10^{-3}	—	—	10.9
Stress	37.1%	3.8×10^{-4}	1.4×10^{-2}	0.99	—	24.8
Stress & freq.	41.9%	5.1×10^{-6}	7.9×10^{-3}	0.98	0.18	68.4

tion case. The mass-constrained compliance minimization design has the highest stress near the reentrant corners and on the boundary of the fixed hole, while the stress ratio is below the limit in much of the rest of the structure. In the stress-constrained and stress- and frequency-constrained designs, the material above the fixed hole does not carry much load while all remaining material is closer to the failure limit than the compliance-based design. In the stress- and frequency-constrained mass minimization case, there are some areas which have lower load-carrying utilization, particularly in the walls formed in the horizontal members, but these features contribute to increasing the fundamental frequency of the structure.

Figure 4.21a shows the history of the stress and frequency constraints during the design optimization. The optimizer satisfies both constraints within about 100 iterations. In the design history, the stress constraint violation spikes at 500 iterations due to the adaptive mesh refinement step, but quickly recovers feasibility.

Figure 4.21b shows the optimization history of the mass and the infeasibility for the stress- and frequency-constrained mass minimization problem, with infeasibility shown on a log scale. Designs are shown at 50, 100, 500, and 1000 iterations. Most of the mass reduction of the structure happens within the first 100 iterations, with a gradual decrease after that point. By the 50th iteration, the optimizer has removed much of the material near the holes where the loads are applied, but by iteration 100, material has started to re-form in these areas. By iteration 500, the design has largely converged, but more detail emerges by the final design. Figure 4.22 shows the optimization history of the first six natural frequencies of the orthogonal bracket. Among these six, there are no repeated natural frequencies at any point. Each natural frequency quickly increased in the beginning of the optimization, but there are only gradual changes after the first 150 iterations. At the final design, the normalized natural frequencies are $\bar{\omega}_1 = 0.19$, $\bar{\omega}_2 = 0.22$, $\bar{\omega}_3 = 0.27$, $\bar{\omega}_4 = 0.37$, $\bar{\omega}_5 = 0.47$, and $\bar{\omega}_6 = 0.55$, respectively.

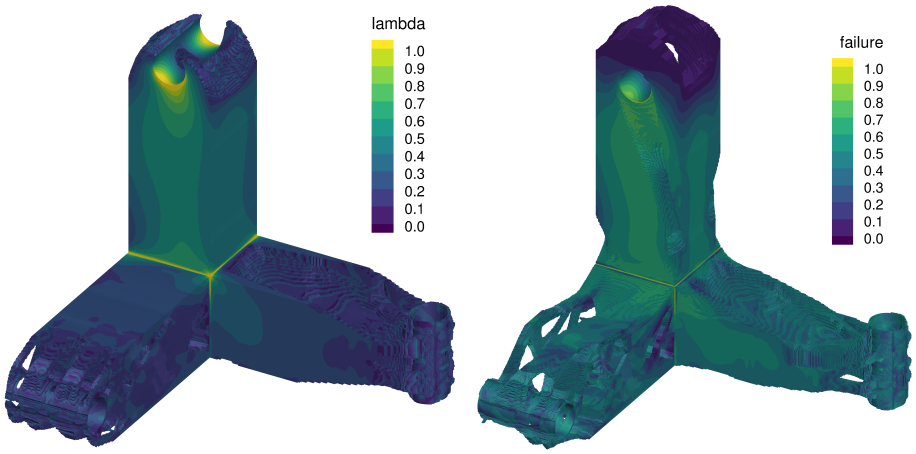

(a) Mass-constrained compliance minimization

(b) Stress-constrained mass minimization

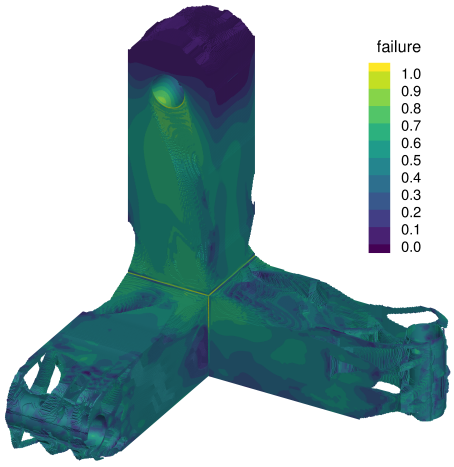

(c) Stress- and frequency-constrained mass minimization

Figure 4.20: Failure for the orthogonal bracket problem results

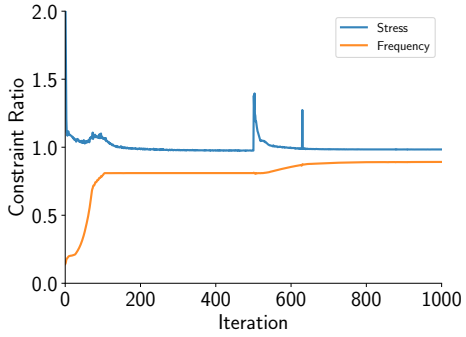

(a) Convergence of stress and frequency constraints

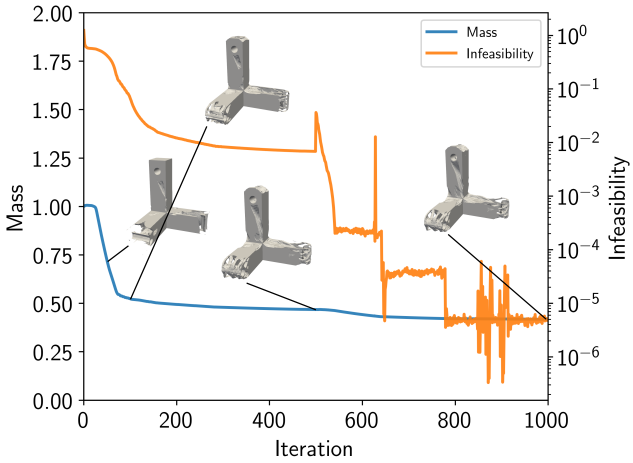

(b) History of objective and infeasibility

Figure 4.21: Optimization history of orthogonal bracket problem

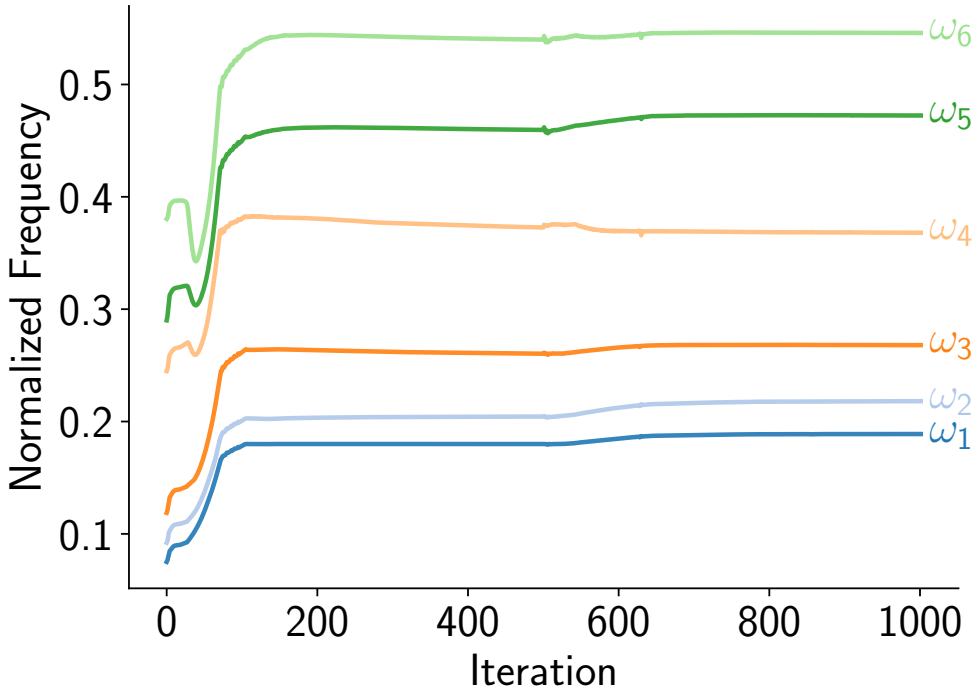

Figure 4.22: History of orthogonal bracket natural frequencies

4.4 Conclusions

High-resolution topology optimization has the potential to be a powerful tool to design structures with strength requirements that operate in high-vibration environments. In order to solve these complex design problems, this work addressed challenges in applying stress and frequency constraints to large-scale topology optimization problems. An element-wise reconstruction of the displacement field enabled the computation of less mesh-sensitive strain and stress fields, improving the design space for stress-constrained optimization. This work also demonstrated that the Jacobi–Davidson method with eigenvector recycling is efficient and robust for solving large-scale natural-frequency problems for topology optimization applications. Finally, these capabilities were demonstrated using cantilever and orthogonal bracket problems, with comparisons for stress-constrained mass minimization, mass-constrained compliance minimization, and stress- and frequency-constrained mass minimization for problems with $\mathcal{O}(10^7)$ degrees of freedom.

CHAPTER 5
STEADY-STATE THERMOELASTIC TOPOLOGY OPTIMIZATION

Many structures must not only withstand mechanical loads, but also operate at high temperatures, inducing thermal expansion that must be accounted for during the design process. This chapter presents thermoelastic topology optimization methodology and results with steady-state heat transfer analysis. First, the equations governing the steady-state thermoelastic analysis within a density-based topology optimization formulation are presented. The modeling approach described in this chapter solves for the distribution of temperature in the domain using the steady-state heat transfer equations, whereas many thermoelastic topology optimization methodologies assume a constant temperature change within the domain, allowing a simple term to be added to the right-hand-side of the linear system. One of the challenges of solving thermoelastic topology optimization problems is that maximum stress and maximum temperature can be competing design considerations that are difficult to trade off. To demonstrate this issue, a Pareto front with 101 optimized designs is presented, minimizing a weighted combination of maximum stress and maximum temperature for a range of weights. Finally, steady-state thermoelastic topology optimization results are presented, including a 2D example which serves as a benchmark for the transient results in the following chapter, and 3D results for the design of an electric motor structural mount.

5.1 Steady-state thermoelastic analysis

This section presents an overview of the steady-state thermoelastic governing equations, first in their continuous form, and then in the discretized form that will be solved using the finite-element tool TACS [97]. The steady-state thermoelastic analysis consists of two components; the continuous form of the linear elasticity equations which are given in Equation 5.1, and the continuous form of the steady-state heat-transfer equations which are given

in Equation 5.2. In the linear elasticity PDE (Equation 5.1), $\mathbf{b}$ are the body forces, and $\tilde{\mathbf{u}}$ are the displacement boundary conditions. The traction vector is represented by $\mathbf{t}$, and $\mathbf{n}$ defines the surface normal. In the heat transfer PDE (Equation 5.2), θ is the temperature state variable, κ is the thermal conductivity, Q is the volumetric heat source, $\tilde{\theta}$ is the prescribed temperature boundary condition, and q defines the heat flux boundary condition. In both sets of equations, $\partial_1\Omega$ is the surface where the Dirichlet boundary conditions are defined, and $\partial_2\Omega$ is the surface where the Neumann boundary conditions are defined, shown in Figure 5.1.

$$\begin{aligned} \nabla \cdot \boldsymbol{\sigma} + \mathbf{b} = 0, \quad \text{on } \Omega \\ \mathbf{u} = \tilde{\mathbf{u}}, \quad \text{on } \partial_1\Omega \\ \boldsymbol{\sigma} \cdot \mathbf{n} = \mathbf{t}, \quad \text{on } \partial_2\Omega \end{aligned} \tag{5.1}$$

$$\begin{aligned} \nabla \cdot (\kappa \nabla\theta) + Q = 0, \quad \text{on } \Omega \\ \theta = \tilde{\theta}, \quad \text{on } \partial_1\Omega \\ (\kappa \nabla\theta) \cdot \mathbf{n} = q, \quad \text{on } \partial_2\Omega \end{aligned} \tag{5.2}$$

The constitutive equation for the elasticity problem is given by Equation 5.3, where $\mathcal{D}$ is the constitutive tensor, $\nabla_s\mathbf{u}$ is the strain given by $\nabla_s\mathbf{u} = \frac{1}{2}(\nabla\mathbf{u} + \nabla^T\mathbf{u})$.

$$\boldsymbol{\sigma} = \mathcal{D} \cdot (\nabla_s\mathbf{u} - \boldsymbol{\alpha}\boldsymbol{\theta}) \tag{5.3}$$

The weak form version of these two sets of equations are then discretized to form the finite element linear system of equations, where the mechanical finite element equations are combined with the heat-conduction finite element equations by adding a one-way coupling term for the linear thermoelastic response. The coupled thermoelastic system of equations is given as

$$\begin{bmatrix} \mathbf{K}(\mathbf{x}) & \mathbf{L}(\mathbf{x}) \\ 0 & \mathbf{H}(\mathbf{x}) \end{bmatrix} \begin{bmatrix} \mathbf{u} \\ \boldsymbol{\theta} \end{bmatrix} = \begin{bmatrix} \mathbf{f} \\ \mathbf{q} \end{bmatrix}, \tag{5.4}$$

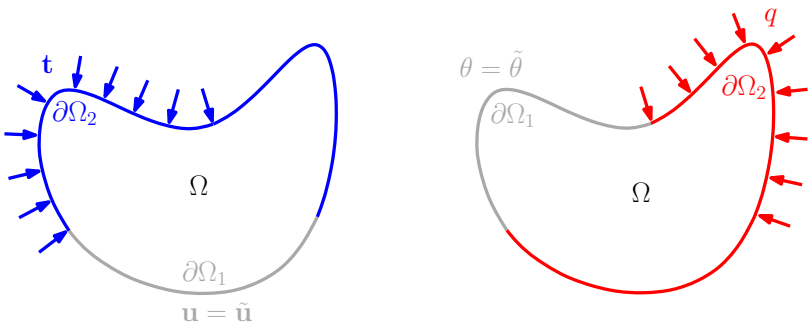

Figure 5.1: Domains for the linear elasticity equations (left) and the steady-state heat transfer equations (right)

where $\mathbf{K}(\mathbf{x})$ is the design-dependent stiffness matrix, $\mathbf{H}(\mathbf{x})$ is the design-dependent thermal conductivity matrix, and $\mathbf{L}(\mathbf{x})$ is the thermoelastic coupling matrix. The vector $\mathbf{u}$ are the displacement state variables, $\boldsymbol{\theta}$ are the temperature state variables, $\mathbf{f}$ are the mechanical forces, and $\mathbf{q}$ are the heat fluxes specified on the boundary.

The stiffness matrix $\mathbf{K}(\mathbf{x})$ is given by

$$\mathbf{K}(\mathbf{x}) = \sum_{i=1}^{n_e} \left(\frac{\xi_i}{1 + q(1 - \xi_i)} + \kappa_0 \right) \mathbf{K}_i, \tag{5.5}$$

where q is the RAMP penalization parameter on the material stiffness. In this work, $q = 5$ is used.

The thermal conductivity matrix, $\mathbf{H}(\mathbf{x})$, is computed as

$$\mathbf{H}(\mathbf{x}) = \int_\Omega \mathbf{B}_\theta^T \kappa(\mathbf{x}) \mathbf{B}_\theta \mathrm{d}\Omega = \sum_{i=1}^{n_e} \left(\frac{\xi_i}{1 + q_\kappa(1 - \xi_i)} + \kappa_0 \right) \mathbf{H}_i, \tag{5.6}$$

where $\mathbf{B}_\theta$ relates the temperature change $\boldsymbol{\theta}$ to its spatial gradient, and $\mathbf{H}_i$ is the element heat conduction matrix. The thermal conductivity $\kappa(\mathbf{x})$ penalized using RAMP penalization with the penalty parameter q_κ, where $q_\kappa = 5$ is used in this work. A small, finite value $\kappa_0 = 10^{-6}$ is added to avoid poor matrix conditioning. The thermal-mechanical coupling

matrix, $\mathbf{L}(\mathbf{x})$, is given by

$$\mathbf{L}(\mathbf{x}) = -\int_{\Omega} \mathbf{B}^T \mathbf{D}\boldsymbol{\alpha}(\mathbf{x})\mathbf{N}\mathrm{d}\Omega = \sum_{i=1}^{n_e} \left(\frac{\xi_i}{1 + q_\beta(1-\xi_i)} + \kappa_0 \right) \mathbf{L}_i, \tag{5.7}$$

where $\mathbf{B}$ is the strain-displacement matrix, $\mathbf{D}$ is the constitutive matrix, $\boldsymbol{\alpha}(\mathbf{x})$ are the thermal coefficients of expansion, and $\mathbf{N}$ are the shape functions. q_β represents the RAMP penalty parameter on the combined term $\mathbf{D}\boldsymbol{\alpha}(\mathbf{x})$, with a value of $q_\beta = 5$ used in this work.

For the thermoelastic problem, the local stress in element i is computed as

$$\sigma_i = \mathbf{D}\left(\mathbf{B}\mathbf{u} - \alpha\boldsymbol{\phi}\left(\mathbf{x}\right)\mathbf{N}\boldsymbol{\theta}\right), \tag{5.8}$$

where $\boldsymbol{\phi}$ is defined as $[1\,1\,0]$ for 2D problems, and $[1\,1\,1\,0\,0\,0]$ for 3D problems.

5.2 Pareto front for multi-objective optimization

Minimizing the maximum temperature of the structure while satisfying stress constraints can be challenging due to the competing nature of these two design considerations. Here, a Pareto front is presented to better understand the trade-off between stress and thermal performance. The Pareto front is based on steady-state topology optimization results where the objective function is a weighted combination of the approximate maximum temperature and approximate maximum stress, given as

$$\begin{aligned}
\min \quad & w_\theta \frac{c_{\mathrm{KS}}(\boldsymbol{\theta}(\mathbf{x}))}{\theta_{\mathrm{ref}}} + (1-w_\theta)\frac{c_{\mathrm{KS}}(\boldsymbol{\sigma}_{\mathrm{vM}}(\mathbf{x},\,\mathbf{u},\,\boldsymbol{\theta}))}{\sigma_y} \\
\text{with respect to} \quad & \epsilon_0 \leq \mathbf{x} \leq 1 \\
\text{such that} \quad & m(\mathbf{x}) \leq m_f \\
\text{governed by} \quad & \begin{bmatrix} \mathbf{K}(\mathbf{x}) & \mathbf{L}(\mathbf{x}) \\ 0 & \mathbf{H}(\mathbf{x}) \end{bmatrix} \begin{bmatrix} \mathbf{u} \\ \boldsymbol{\theta} \end{bmatrix} = \begin{bmatrix} \mathbf{f} \\ \mathbf{q} \end{bmatrix}
\end{aligned} \tag{5.9}$$

Table 5.1: Material properties and dimensions used for Pareto front

Variable	Value
Height, h	$30\ \mathrm{cm}$
Length, l	$80\ \mathrm{cm}$
Traction length, Δh	$8\ \mathrm{cm}$
Heat flux length, Δl	$16\ \mathrm{cm}$
Thickness, b	$1\ \mathrm{cm}$
Density, ρ	$2780\ \mathrm{kg/m^3}$
Young's modulus, E	$72.4\ \mathrm{GPa}$
Yield stress, σ_y	$345\ \mathrm{MPa}$
Coefficient of thermal expansion, α	$24 \times 10^{-6}\ ^\circ\mathrm{C}^{-1}$
Specific heat capacity, c	$0.875\ \mathrm{kJ/kg} \cdot^\circ \mathrm{C}$
Thermal conductivity, k	$151\ \mathrm{W/m \cdot K}$

where $w_\theta \in [0, 1]$ is the weight on the temperature portion of the objective, and $1 - w_\theta$ is the weight on the stress portion. A weight value of $w_\theta = 0$ indicates a maximum stress minimization problem, and a weight value of $w_\theta = 1$ indicates a maximum temperature minimization problem. The stress value is scaled by the yield stress, and the temperature value is scaled by a reference temperature change, θ_{ref}, so that the two components of the objective are both unitless and of the same order of magnitude.

The problem domain used is shown in Figure 5.2, which is a cantilever beam with a traction over a portion of the right-hand edge, an input heat flux over a portion of the bottom surface, and a fixed temperature boundary on the top surface of $\Delta T = 0$. The dimensions of the geometry and the material properties of the problem are given in Table 5.1, with the selected material properties based on Aluminum 2024-T6. The mechanical traction is $P/\Delta h = 15 \times 10^6\ \mathrm{N/m}$, and the heat flux is $1250\ \mathrm{W/m}$.

Figures Figure 5.3 and Figure 5.4 below show the results of the Pareto front generated using 101 topology optimized designs. For both figures, the y-axis shows the value of the scaled temperature objective, and the x-axis shows the value of the scaled stress objective. Figure Figure 5.3 shows the Pareto front with topologies for w_θ = 0%, 10%, 20%, ..., and 100%, and Figure Figure 5.4 shows some particular topologies that are highlighted in the

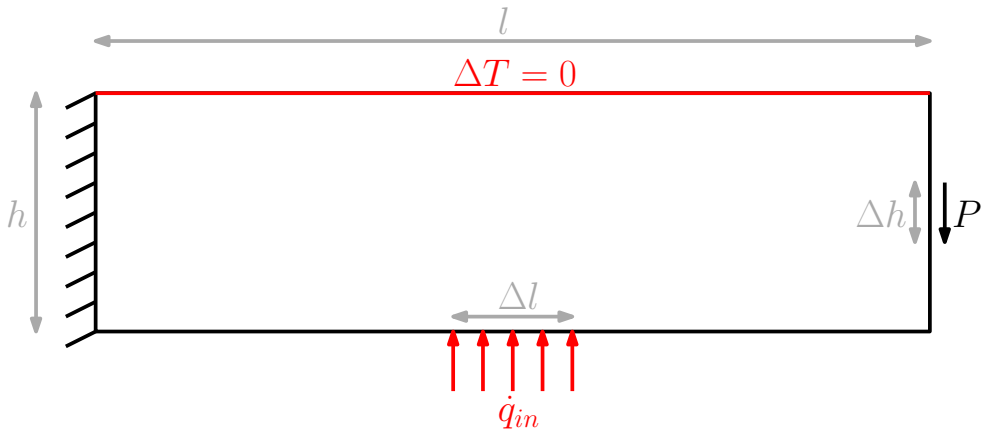

Figure 5.2: Problem domain and boundary conditions

following discussion.

The design with $w_\theta = 0\%$ shows a structure with prominent truss features and material along the top and bottom edges to increase the bending stiffness of the structure. This maximum stress minimization design is asymmetric, which is expected because of the temperature gradient between the top and the bottom surfaces. The first five designs ($w_\theta = 0$ through 4%) all look very similar, with the same number of members in generally the same pattern. As the design evolves to incorporate thermal considerations, the internal truss structures on the right are being shifted down. At $w_\theta = 5\%$, a new small truss is added between the existing members and the location of the heat flux boundary condition. This small addition results in the first gap down on the plot, improving the thermal performance significantly. As w_θ increases, the internal upper truss member continues to move down toward the location of the heat source. By $w_\theta = 22\%$ the small truss that formed at $w_\theta = 5\%$ has now been absorbed by the neighboring structure, thickening the region near the heat source. Note that up to this point, the trend on the Pareto front has been approximately vertical, indicating that thermal performance can be factored into the design without any increase in maximum stress, up to a point (for this specific design problem).

At this point, the truss that had been shifting down is now effectively connected between the heat source on the bottom and the heat sink at the top. There is still a slight bend near the bottom of this member, which will straighten out as w_θ increases further - first noticeable at

$w_\theta = 38\%$. This "heat pipe" feature will remain prominent and become gradually thicker and more vertical to increase the heat-carrying capacity and shorten the heat conduction distance. Here, the left-most trusses begin to change drastically between designs, with no clear trend - note the differences between 38%, 41%, and 42%. At $w_\theta = 57\%$, a gap along the upper surface emerges and remains until the next major design change at $w_\theta = 70\%$. This results in a small discontinuity down from $w_\theta = 69\%$ to $w_\theta = 70\%$, indicating that this design change had a significantly favorable effect on the thermal performance. This improvement is driven by the heat pipe being made fully vertical, and now there are two angled members connecting the heat pipe to the fixed mechanical boundary condition on the left end. On the plot around this point, we can see that the trend becomes much more horizontal, indicating that a small reduction in maximum temperature requires a large increase in maximum stress. After $w_\theta = 70\%$, the design changes are subtle, predominantly consisting of a steady increase in thickness of the heat pipe, and thinning the members connecting the heat pipe to the fixed displacement boundary condition on the left. By $w_\theta = 99\%$, the structure is attached to the force on the right by a very thin member with some intermediate material surrounding it. At $w_\theta = 100\%$, the final design is simply the central heat pipe. The points for $w_\theta = 97\%$, 98%, 99%, and 100% are not shown because the stress becomes so large that it would have distorted the scale of the figure. Overall the trend of the Pareto front is very smooth, with certain jumps or breaks in the trend that can be explained by discrete, significant changes in the design.

5.3 Steady-state thermoelastic topology optimization results

5.3.1 2D steady-state thermoelastic topology optimization results

This section presents a steady-state thermoelastic topology optimization result with the same domain (Figure 5.2), material properties (Table 5.1), and boundary conditions as were used in the Pareto front. This steady-state example will serve as a basis for comparison with the transient thermoelastic topology optimization results in the following chapter.

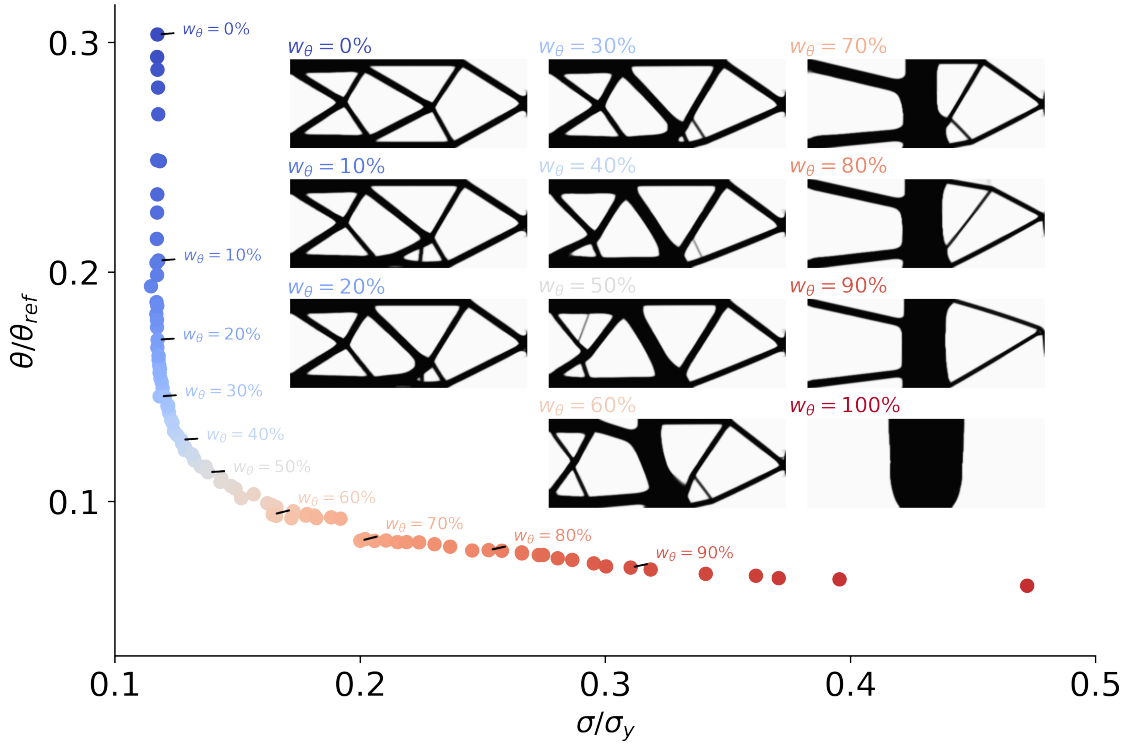

Figure 5.3: Pareto front of 100 topology optimization results minimizing a weighted sum of maximum stress and maximum temperature

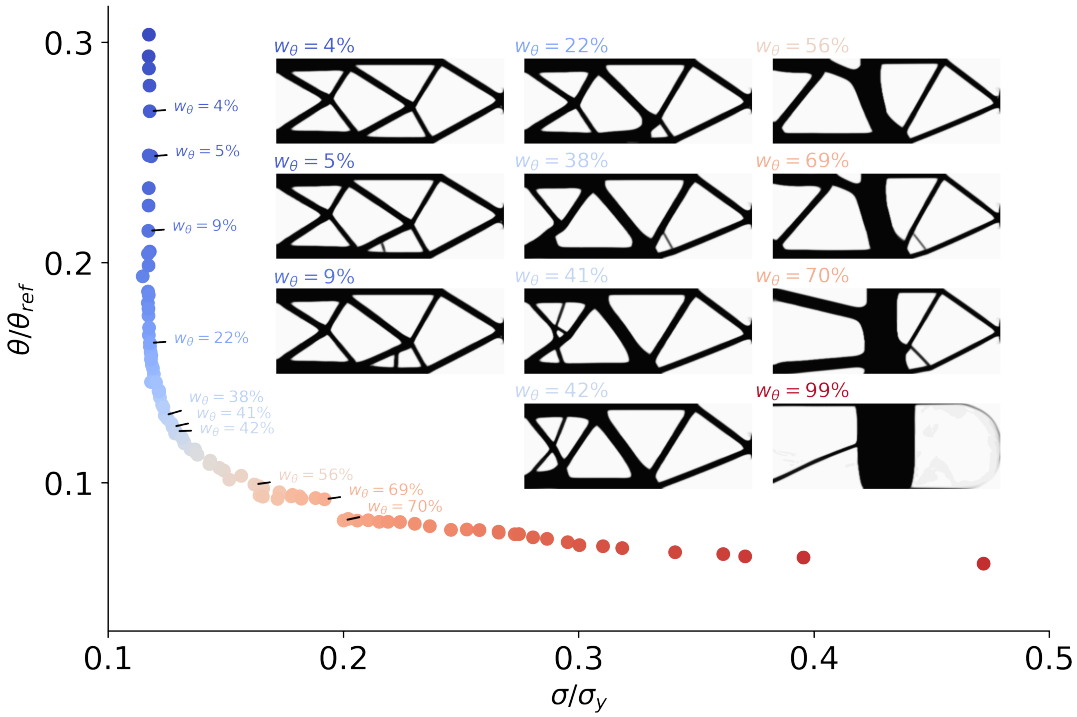

Figure 5.4: Pareto front of 101 topology optimization results minimizing a weighted sum of maximum stress and maximum temperature with particular topologies shown

For the steady-state thermomechanical topology optimization design problem, we seek to minimize the maximum temperature subject to a fixed-mass constraint and a constraint on the maximum stress. The maximum temperature and maximum stress are both computed approximately using KS-aggregation (Equation 4.2). The optimization problem is stated as:

$$\begin{aligned}
\min \quad & c_{\mathrm{KS}}(\boldsymbol{\theta}(\mathbf{x})) \\
\text{with respect to} \quad & \epsilon_0 \leq \mathbf{x} \leq 1 \\
\text{such that} \quad & m(\mathbf{x}) \leq m_f \\
& c_{\mathrm{KS}}(\boldsymbol{\sigma}_{\mathbf{vM}}(\mathbf{x}, \mathbf{u}, \boldsymbol{\theta}))/\sigma_y \leq \beta \\
\text{governed by} \quad & \begin{bmatrix} \mathbf{K}(\mathbf{x}) & \mathbf{L}(\mathbf{x}) \\ 0 & \mathbf{H}(\mathbf{x}) \end{bmatrix} \begin{bmatrix} \mathbf{u} \\ \boldsymbol{\theta} \end{bmatrix} = \begin{bmatrix} \mathbf{f} \\ \mathbf{q} \end{bmatrix}
\end{aligned} \tag{5.10}$$

where ϵ_0 is a small, finite lower bound on the design values, m_f is the fixed-mass value, σ_{vM} is the von Mises stress, and σ_y is the material yield stress.

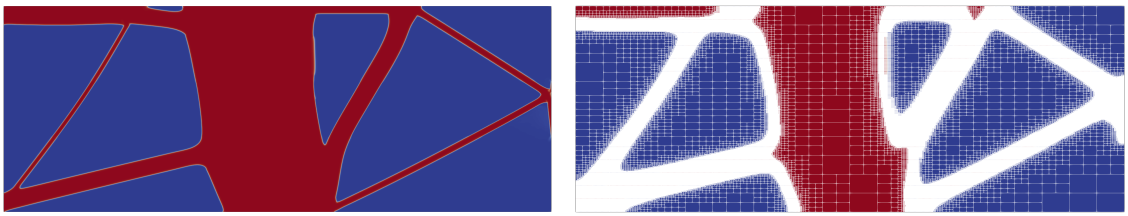

(a) Steady-state topology optimization result (b) Final mesh

Figure 5.5: Optimized topology with steady-state analysis and final mesh after three cycles of adaptive mesh refinement

The objective of the topology optimization problem is to minimize the maximum temperature, subject to a stress constraint and a fixed-mass constraint (Equation 5.10). The result of the steady-state topology optimization is shown in Figure 5.5a, with the final mesh after three cycles of adaptive mesh refinement shown in Figure 5.5b, refining the mesh along the solid-void boundary according to a solution of the Helmholtz equation. The resulting design shows truss-like features and material on the top and bottom surfaces to carry the bending moment, with a prominent vertical member to conduct the heat from the input heat flux boundary condition on the bottom surface to the fixed temperature constraint at the top surface.

5.3.2 X-57 high-lift motor thermoelastic topology optimization results

This section presents steady-state thermoelastic topology optimization for a practical 3D application - specifically, the mounting structure for the high-lift motors on the NASA X-57 Maxwell. Electric aircraft generate excess heat from batteries, motors, and power electronics with limited mechanisms to efficiently dissipate it. As a result, it can be beneficial to design electric aircraft structures to both sustain structural loads, while also conducting excess heat to an exposed aerodynamic surface where it can be convected away from the vehicle. In this section, coupled thermoelastic topology optimization is applied to the design domain to produce a light-weight structural concept that can sustain both thermal and mechanical loads. Two choices of mechanical boundary conditions are presented, and the

effects on the resulting designs are investigated. Additionally, the thermoelastic topology optimized designs are compared with purely mechanical designs.

The motor (Figure 2.1a) occupies the volume enclosed by the motor housing. The primary mechanical loads induced on the motor housing structure are a result of the inertia of the motor during flight maneuvers. To model these loads, a traction is applied to the inner surfaces of the volume equal to the mass of the motor multiplied by the g-loading requirements of the aircraft. Three motor-containment loads are defined based on the aircraft handling requirements: a 3.4g upward acceleration, a 2g downward acceleration, and a 3g forward acceleration. The containment loads are only applied to the surfaces that make intuitive sense for each case, so the upward acceleration results in a traction distributed across the lower half of the inner shell structure, the downward acceleration results in a traction distributed across the top half of the inner shell structure, and the forward acceleration creates a traction across the inner surface of the mounting plate structure. A safety factor n_{vert} is applied to both the upward and downward motor-containment loads, and a safety factor of n_{fwd} is applied for the forward motor-containment load. An outward pressure load is also applied to both the inner and outer surfaces. These loads are combined to form a set of three load cases depicted in Figure 5.6. Note that the blue arrows indicate the loads due to the acceleration of the motor contained within the structure, which act purely in the Cartesian directions they are shown, while the black arrows indicate the pressure loading, which acts normal to the surface.

The motor drives the propeller through the axial rod, which passes through the center hole in the base of this geometry. It is inferred that the inner surface of this hole should be frictionless, so the hole in the base plate is constrained in all radial ($x,\ y$) directions, but unrestricted axially (z). The three smaller holes on the plate are used as connections to the motor as well as the structure on the other side, so these holes will be fully clamped. The forward-most surface connects to the nose cap of the high-lift motor, and the outer portion of the aft surface connects to the neighboring nacelle structure. Since these surfaces

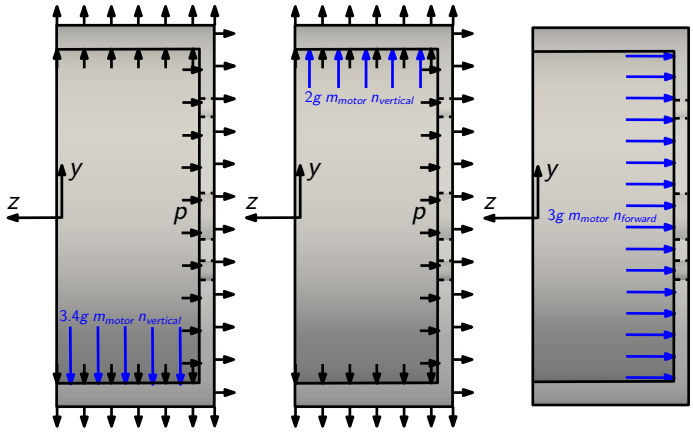

(a) Load case 1 (b) Load case 2 (c) Load case 3

Figure 5.6: Load cases defined for topology optimization. Note that blue arrows indicate loads applied in the Cartesian direction they are shown, while the black arrows indicate pressure loads which act normal to the surface.

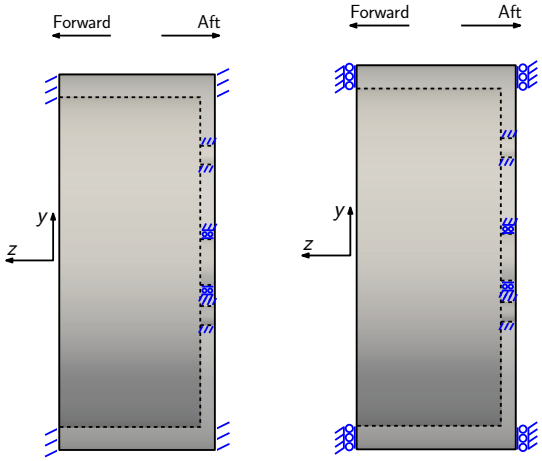

(a) Fully-constrained structural boundary conditions (b) Axially-constrained structural boundary conditions

Figure 5.7: Fully-constrained structural boundary conditions, and axially-constrained structural boundary conditions

connect to other components which are also elastic, the appropriate choice of boundary conditions for these faces is somewhat unclear. Two choices are considered: the first, in which theses surfaces are fully-constrained, and the second, in which these surfaces are constrained only in the axial ($\pm\, z$) directions. The first choice is overly constrained but ensures the surfaces will be properly mated. For the second choice, it can be argued that since this is a thin-walled structure, the resistance to motion will be greatest in the axial direction, and that because the four holes are all already being constrained radially, that the radial direction is sufficiently constrained. Figure 5.7a depicts the fully-constrained set of boundary conditions, while Figure 5.7b depicts the axially-constrained set of boundary conditions.

The remainder of this section presents thermoelastic topology optimization results using the boundary conditions and load cases discussed above. The thermomechanical topology optimization design problem is stated to minimize the structure's mass while satisfying a stress constraint for each one of the three load cases outlined. The problem formulation can be written as

$$
\begin{aligned}
\min \quad & m(\mathbf{x}) \\
\text{with respect to} \quad & \epsilon_0 \leq \mathbf{x} \leq 1 \\
\text{such that} \quad & c_{\mathrm{KS}}(\boldsymbol{\sigma}_{\mathrm{vM}}(\mathbf{x}, \mathbf{u}_i, \boldsymbol{\theta}_i))/\sigma_y \leq \beta \qquad \text{for } \; i = 1, 2, 3 \\
\text{governed by} \quad & \begin{bmatrix} \mathbf{K}(\mathbf{x}) & \mathbf{L}(\mathbf{x}) \\ 0 & \mathbf{H}(\mathbf{x}) \end{bmatrix} \begin{bmatrix} \mathbf{u}_i \\ \boldsymbol{\theta}_i \end{bmatrix} = \begin{bmatrix} \mathbf{f}_i \\ \mathbf{q}_i \end{bmatrix}
\end{aligned}
\tag{5.11}
$$

where $\mathbf{x}$ are the design variables, and $\mathbf{u}_i$ and $\boldsymbol{\theta}_i$ are the state variables at each of the three load cases for $\mathbf{f}_i$ and $\mathbf{q}_i$, with $i = 1, 2, 3$. Here, ϵ_0 is a small finite value used as a lower bound on the design variables. Each optimization problem is solved with a RAMP penalization value of $q = 8$, a stress-relaxation parameter value of $\epsilon = 0.2$, and a KS parameter value of $\rho_{\mathrm{KS}} = 25$. Each case uses the same mesh with 2,181,120 elements and 9,294,068

degrees of freedom, resulting in an optimization problem with 2,323,517 design variables, solved on 72 processors.

Here, topology optimization results are presented for the motor-housing structure using two sets of boundary conditions which differ in how the forward and aft surfaces that interface with adjacent nacelle structure are treated. The first approach treats these surfaces as being fully constrained in each direction, while the second approach constrains these surfaces in only the axial direction. The fully constrained modeling approach assumes perfectly rigid adjacent structures, resulting in higher thermally-induced stresses but more support for mechanical loading. The less-constrained modeling approach results in lower thermally-induced stress, but less rigid structural support. The exact boundary conditions may lie between the two options presented. These boundary conditions strongly impact the resulting topology. This is especially true for thermomechanical topology optimization, because the magnitude of the thermal loads is a direct consequence of the extent to which thermal expansion is inhibited. For each set of boundary conditions, results from purely mechanically loaded cases are presented, as well as cases with a uniform temperature increase throughout the domain. The temperature change values used for these results are incongruent with the thermal analysis in chapter 2, because temperatures higher than those used here do not allow converged designs due to improper boundary conditions. Instead, temperature values were used that allowed converged designs in order to consider designs which consider temperature change. The mechanical boundary conditions may play a role in the degree to which temperature change can be applied to this problem. However, as chapter 2 showed, the heat transfer of this structure has not reached steady-state, so because the steady-state and transient temperature distributions are different, simply matching the maximum temperature between steady-state and transient analyses would not yield the same result for a structural optimization problem, resulting in an over-designed structure.

Figure 5.8 shows the results of the fully-constrained case with no temperature increase, and Figure 5.9 shows the fully-constrained case with a uniform temperature in-

Figure 5.8: Topology optimization results of the fully-constrained case with $\Delta \mathrm{T} = 0\ ^{\circ}\mathrm{C}$. $-x$, $+y$, and $+z$ views shown from left to right

Figure 5.9: Topology optimization results of the fully-constrained case with $\Delta \mathrm{T} = 5\ ^{\circ}\mathrm{C}$. $-x$, $+y$, and $+z$ views shown from left to right

Figure 5.10: Topology optimization results of the axially-constrained case with $\Delta \mathrm{T} = 0\ ^{\circ}\mathrm{C}$. $-x$, $+y$, and $+z$ views shown from left to right

Figure 5.11: Topology optimization results of the axially-constrained case with $\Delta \mathrm{T} = 5\ ^{\circ}\mathrm{C}$. $-x$, $+y$, and $+z$ views shown from left to right

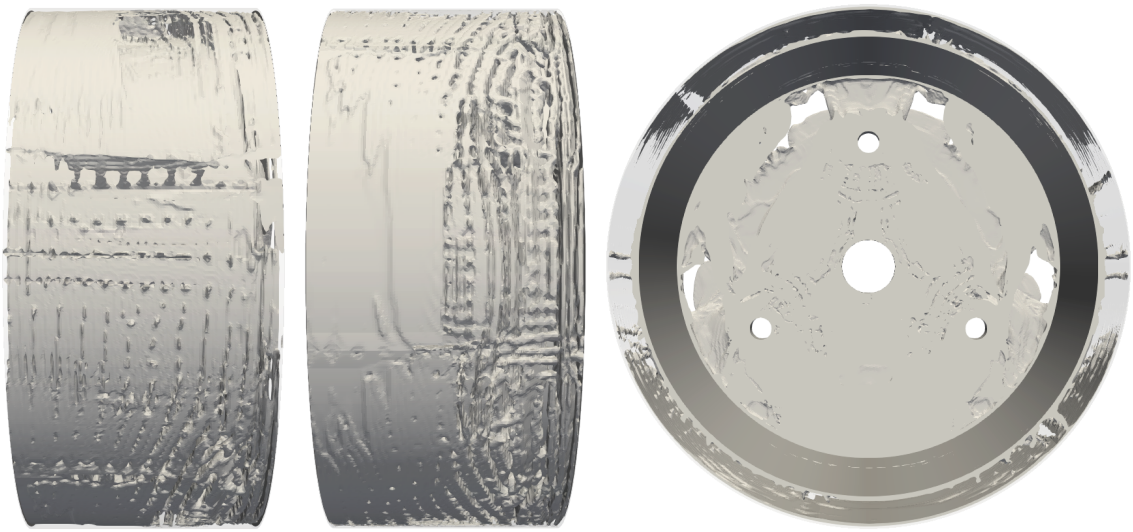

Figure 5.12: Topology optimization results of the axially-constrained case with $\Delta \mathrm{T} = 10\ ^{\circ}\mathrm{C}$. $-x$, $+y$, and $+z$ views shown from left to right

crease of $5\ ^{\circ}\mathrm{C}$. Figure 5.10, Figure 5.11, and Figure 5.12 show the results with the axially-constrained boundary conditions, with temperature increases of $0°$C, $5°$C, and $10°$C, respectively. Table 5.2 provides the load values and temperature change for each case, the resulting mass fraction for each design, the infeasibility and optimality error measure in the ℓ_∞ norm and the total time required to perform each optimization. A limit of 500 design iterations is imposed. The infeasibility in each case is less than 6.9×10^{-4}. The ℓ_∞ norm of the optimality error in each case is less than 6.6×10^{-4}, indicating well-converged solutions. The mechanical loads and the temperature increase are different in each case, but the resulting mass fraction for each design is between 29.4 and 32.8%. The outer shell must be solid in order to have a smooth nacelle outer mold line. To achieve this, the lower bound of the design variables is adjusted for elements on the outer surface to require material there. In all images, this outer shell is made to be transparent so that it is possible to see the interior structure.

In the fully-constrained case with no temperature change, shown in Figure 5.8, the final design removes regions of low stress in the plate, and forms numerous trusses along the top and bottom ($\pm\ y$) faces, connecting the fully-constrained boundary conditions to the shell

Table 5.2: Summary of topology optimization results

BCs	ΔT (°C)	n_{vert}	n_{fwd}	F_{p} (N)	$m\%$	infeas.	ℓ_∞	Time (h)
full	0	1200	350	500	32.1	6.6×10^{-4}	1.5×10^{-4}	18.7
full	5	850	350	400	29.6	2.4×10^{-4}	4.4×10^{-5}	14.4
axial	0	450	250	500	32.0	6.7×10^{-4}	4.8×10^{-4}	17.0
axial	5	500	225	200	30.7	6.9×10^{-4}	1.6×10^{-4}	21.2
axial	10	300	225	200	32.9	3.7×10^{-4}	6.1×10^{-4}	12.5

structure in the directions where the inertial loading is applied. Thin-walls also form along the inside of the shell to carry the pressure loading. When a uniform temperature increase $\Delta\text{T} = 5\ ^\circ\text{C}$ is applied, shown in Figure 5.9, a similar design emerges, with more numerous and longer members along the top and bottom of the shell.

In the axially-constrained case with no temperature increase, shown in Figure 5.10, material is removed from the plate in areas of low stress concentration, with thin shells forming along the top and bottom ($\pm\ y$) faces and thin shell structure forming along the inner surface on the sides ($\pm\ x$). With only axially-constrained boundary conditions, the bending moment through the shell is now much higher due to the inertial loads. This leads to the shell formation along the outermost surfaces on the top and bottom faces, to provide the highest bending stiffness possible. When a temperature increase $\Delta\text{T} = 5\ ^\circ\text{C}$ is applied, as shown in Figure 5.11, a similar design emerges, but now with increased support through the shell through the utilization of truss-like structures along the $-z$ portion of the $\pm\ y$ faces. Since the holes are the only radially-constrained surface, this configuration is similar to a cantilevered beam, so the bending moment is largest on the $-z$ side of the shell. Finally, when a temperature increase of $\Delta\text{T} = 10^\circ\text{C}$ is applied, as shown in Figure 5.12, the optimizer thickens the inner portion of the shell throughout, and numerous truss-like members form between the inner and outer shell faces, predominantly on the top and bottom ($\pm\ y$) faces, but some smaller truss members also form on the sides ($\pm\ x$).

Comparing the two different choices of boundary conditions for the cases where no temperature increase is applied, we can see that the fully-constrained case can withstand

much larger mechanical loads than the case with only axially-constrained boundary conditions. The highest stress concentrations in both cases occur around the holes in the plate. The fully-constrained case can handle a higher load factor because the reaction forces at the holes, and thereby the stress concentrations, are reduced compared to the axially-constrained case. On the other hand, thermal stresses are induced through the thermal expansion of the domain being constrained by the boundary conditions. As a result, since the axially-constrained case is less constrained, it is capable of handling larger temperature increases. When running the topology optimization cases, it was necessary to reduce the applied mechanical loads when a larger temperature increase was applied to achieve a feasible design. Table 5.2 illustrates that the reduction in mechanical loads is less for the axially-constrained boundary conditions than for the fully constrained case. In the case with axial boundary conditions, it was possible to apply a temperature increase of $10\ ^{\circ}\mathrm{C}$ with mechanical loads comparable to those at lower temperatures and still obtain a feasible design. On the other hand, it was not possible to obtain a well-defined topology with a $10\ ^{\circ}\mathrm{C}$ increase in temperature for the fully-constrained case, even at much more modest mechanical loads. The designs presented in this chapter have very intricate features which would make manufacturing these designs impractical. Manufacturability has not been taken into consideration with any of these results. However, many other authors have studied manufacturability, including Vatanabe, Lippi, Lima, Paulino, and Silva [133] and Brackett, Ashcroft, and Hague [134]. In addition to manufacturability, other factors must also be considered before these design concepts can be used in real applications. These factors depend entirely on the structure's requirements, but may include considerations such as fatigue, fracture, dynamic response, or transient thermal behavior.

5.4 Conclusions

This chapter presented steady-state thermoelastic topology optimization methodology and results. Steady-state thermoelastic topology is not a new area of research; however, I pre-

sented a Pareto-front using 101 topology optimization results, providing a novel perspective on the competing nature of mechanical and thermal performance that makes thermoelastic structural design so challenging. I applied stress-constrained thermoelastic topology optimization to produce novel structural design concepts for the mounting structure of an electric motor. These designs are, to my knowledge, the largest stress-constrained thermoelastic topology optimization results presented, with 2,181,120 elements, 9,294,068 degrees of freedom, and 2,323,517 design variables. I presented results using two different choices of boundary conditions and found that the choice of boundary condition has a large impact on the resulting design. Additionally, designs generated without thermal loads were also presented to highlight the effect that the temperature increase has on the resulting design.

CHAPTER 6
TRANSIENT THERMOELASTIC TOPOLOGY OPTIMIZATION

As chapter 2 showed, many structures with significant mechanical loading and heating never reach thermal equilibrium. Steady-state heat transfer analysis is insufficient for these problems for a number of reasons. First, the boundary conditions are often heavily dependent on time, which makes determining the worst-case loads challenging. Second, the distribution of temperature, and therefore also stress, will differ with transient heat transfer, which would lead to different designs. Last, the steady-state heat transfer problem cannot be solved without fixed-temperature boundary conditions that are physically unrealistic in most instances.

This chapter presents transient thermoelastic topology optimization background and examples. First, the equations governing the transient heat transfer problem are presented. Next, the approach used to integrate the governing equations in time is described, followed by the transient thermoelastic topology optimization problem formulation. This approach is then validated against an analytic solution. Finally, stress-based transient thermoelastic topology optimization results are presented and discussed, including a comparison against a steady-state-based result from the previous chapter.

6.1 Transient thermoelastic analysis

This section presents an overview of the transient heat transfer governing equations, first in continuous form, followed by the discretized form that need to be integrated in time numerically. For the transient analysis in this work, only the heat-transfer portion is considered time-dependent. Because the structural time-scale is much shorter than the thermal time-scale, the structural inertia contributions are zeroed out so that only the heat-transfer problem is time-dependent, and the elasticity equations are solved as a quasi-static system.

Stresses are still time-dependent due to the thermal expansion contribution. Given this, the only relevant time-dependent partial differential equation then is the heat transfer equation, given as:

$$\begin{aligned} \rho c\dot{\theta} &= \nabla \cdot (\kappa \nabla \theta) + Q, \quad \text{on } \Omega \text{ for } t \in [0, t_f] \\ \theta &= \tilde{\theta}, \qquad\qquad\qquad \text{on } \partial_1 \Omega \\ (\kappa \nabla \theta) \cdot \mathbf{n} &= q, \qquad\qquad\qquad \text{on } \partial_2 \Omega \\ \theta(t=0) &= \theta_0 \end{aligned} \tag{6.1}$$

which is similar in form to the steady-state heat transfer PDE (Equation 5.2), only now the governing equation holds from the initial time, $t = 0$, to the final time, $t = t_f$, and initial conditions $\theta(t = 0) = \theta_0$ need to be defined, where θ_0 represents the initial temperature state in the domain. The domain Ω and boundaries $\partial\Omega_1$ and $\partial\Omega_2$ refer to the same domain (Figure 5.1) used for the steady-state heat transfer PDE. The linear elasticity PDE is still assumed to be steady-state, so Equation 5.1 still holds. The discretized form of the transient coupled thermoelastic system of equations is given as

$$\begin{bmatrix} 0 & 0 \\ 0 & \mathbf{C}(\mathbf{x}) \end{bmatrix} \begin{bmatrix} 0 \\ \dot{\boldsymbol{\theta}}(t_k) \end{bmatrix} + \begin{bmatrix} \mathbf{K}(\mathbf{x}) & \mathbf{L}(\mathbf{x}) \\ 0 & \mathbf{H}(\mathbf{x}) \end{bmatrix} \begin{bmatrix} \mathbf{u}(t_k) \\ \boldsymbol{\theta}(t_k) \end{bmatrix} = \begin{bmatrix} \mathbf{f} \\ \mathbf{q}(t_k) \end{bmatrix}, \; k = 0, 1, \ldots, N \tag{6.2}$$

where $\mathbf{C}(\mathbf{x})$ is the design-dependent heat capacity matrix, and N indicates the number of time steps so that $t_{k=0} = 0$ and $t_{k=N} = t_f$, resulting in a time-step size of $\Delta t = t_f/N$. The heat capacity matrix is given by

$$\mathbf{C}(\mathbf{x}) = \int_\Omega \rho(\mathbf{x}) c(\mathbf{x}) \mathbf{N} \mathrm{d}\Omega = \sum_{i=1}^{n_e} \xi_i^2 \mathbf{C}_i, \tag{6.3}$$

where $\mathbf{C}_i$ is the element heat capacity matrix. Both density $\rho(\mathbf{x})$ and specific heat capacity $c(\mathbf{x})$ are evaluated linearly to the interpolated density $\boldsymbol{\xi}$, leading to the ξ^2 term.

This linear system of equations must then be integrated in time numerically to obtain the time-dependent solution of the state variables $\mathbf{u}(\mathbf{t})$ and $\boldsymbol{\theta}(\mathbf{t})$. Note that even while the

structural inertia term is zeroed-out, the mechanical displacements $\mathbf{u}$ are still a function of time, due to the thermal expansion component of the mechanical displacement and the temperature state variables $\boldsymbol{\theta}$ being a function of time. These governing equations are integrated in time using TACS [135]. Here, a second-order backwards difference formula (BDF) scheme is used. The procedure used for integrating these equations follow, as given by Boopathy and Kennedy [136]. Since the governing equations for this work only require first derivatives, any second derivative terms are neglected in the following equations. Using the BDF scheme, the first derivative of the state variables at the k^{th} time-step $\dot{\mathbf{q}}_k$ are given by

$$\dot{\mathbf{q}}_k = \frac{1}{\Delta t} \sum_{i=0}^{p} \alpha_i \mathbf{q}_{k-i} + \mathcal{O}(\Delta t^p) \tag{6.4}$$

where Δt is the time-step size (which is constant), α_i are coefficients of integration, and p is the order of integration. In this work, $p = 2$ is used.

After the first time-derivative of the state variables are approximated using Equation 6.4, the residual of the nonlinear system of equations can be formed as

$$\mathbf{R}_k(\dot{\mathbf{q}}_k, \mathbf{q}_k, \mathbf{x}, t_k) = 0. \tag{6.5}$$

The exact form of the residual is given by rearranging Equation 6.2, subtracting the right-hand-side on both sides so that it is equal to zero. This residual is solved iteratively using Newton's method. The state variables are updated by $\Delta\mathbf{q}_k^n$ at each Newton iteration n, and the first time-derivative of the state variables are updated by a scaled factor of the state variable update. The linearization of the residual equation is given by

$$\left[\frac{\alpha_0}{\Delta t}\frac{\partial \mathbf{R}}{\partial \dot{\mathbf{q}}} + \frac{\partial \mathbf{R}}{\partial \mathbf{q}}\right] \Delta\mathbf{q}_k = -\mathbf{R}_k(\dot{\mathbf{q}}_k, \mathbf{q}_k, \mathbf{x}, t_k) \tag{6.6}$$

and the subsequent updates are given by

$$\begin{aligned} \mathbf{q}_k^{n+1} &= \mathbf{q}_k^n + \Delta\mathbf{q}_k^n, \\ \dot{\mathbf{q}}_k^{n+1} &= \dot{\mathbf{q}}_k^n + \frac{\alpha_0}{\Delta t}\Delta\mathbf{q}_k^n. \end{aligned} \tag{6.7}$$

The transient thermoelastic topology optimization problem is formulated to minimize the maximum temperature in the domain at the final time step, represented as $c_{\mathrm{KS}}(\boldsymbol{\theta}(\mathbf{x},\, t = t_f))$. The problem is subject to the same mass constraint used for the steady-state results, and the stress-constraint uses the stress at the final time step, $c_{\mathrm{KS}}(\boldsymbol{\sigma}_{\mathrm{vM}}(\mathbf{x},\, \mathbf{u},\, t = t_f))$. The equations are now governed by the transient heat-transfer equation (Equation 6.1) integrated in time from the initial time, $t = 0$, to the final time, $t = t_f$. The formulation of the time-dependent thermoelastic topology optimization takes the form

$$\begin{aligned} \min \quad & c_{\mathrm{KS}}(\boldsymbol{\theta}(\mathbf{x},\, t = t_f)) \\ \text{with respect to} \quad & \epsilon_0 \leq \mathbf{x} \leq 1 \\ \text{such that} \quad & m(\mathbf{x}) \leq m_f \\ & c_{\mathrm{KS}}(\boldsymbol{\sigma}_{\mathrm{vM}}(\mathbf{x},\, \mathbf{u},\, \boldsymbol{\theta}, t = t_f)/\sigma_y \leq \beta \\ \text{governed by} \quad & \begin{bmatrix} 0 & 0 \\ 0 & \mathbf{C}(\mathbf{x}) \end{bmatrix} \begin{bmatrix} 0 \\ \dot{\boldsymbol{\theta}}(t_k) \end{bmatrix} + \begin{bmatrix} \mathbf{K}(\mathbf{x}) & \mathbf{L}(\mathbf{x}) \\ 0 & \mathbf{H}(\mathbf{x}) \end{bmatrix} \begin{bmatrix} \mathbf{u}(t_k) \\ \boldsymbol{\theta}(t_k) \end{bmatrix} = \begin{bmatrix} \mathbf{f} \\ \mathbf{q}(t_k) \end{bmatrix} \;,\; k = 1, \ldots, N \end{aligned} \tag{6.8}$$

A key benefit of using time-dependent heat transfer is that the worst-case loads can be used for design optimization even when the worst case loads are path-dependent, not known ahead of time, or are design-dependent. For optimization problems in this thesis, the time-dependent objective and constraint values are evaluated at the final time step. This is valid only because of the load-cases that are chosen, where we know in advance that the worst-case temperature (and therefore stress, also) will occur at the final time step. If this were not known in advance of performing the optimization, an additional KS-function could be utilized for time-aggregation.

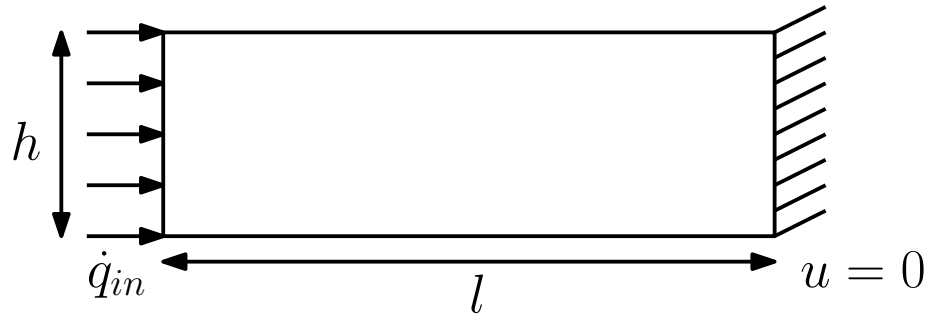

Figure 6.1: Heat conduction problem for validation

6.1.1 Validation of the numerical integration of the transient thermal problem

This section presents a validation of the numerical integration of the transient thermal problem. The notation used for this derivation is slightly different than the previous representations in Equation 6.1, where in this case u represents the temperature state variables. Figure 6.1 depicts a rectangular beam which is subject to a heat flux boundary condition on the left side, with a fixed temperature boundary condition $u = 0$ on the right side. This problem can be treated as a one-dimensional problem, simplifying the analytic result. First, I will derive the analytic solution to this problem, and then I will present a comparison of the solution to this problem computed numerically. The specific PDE which governs this problem is given by:

$$\begin{aligned} &u_t = \alpha u_{xx};\ \alpha = \frac{\kappa}{\rho c_p} \\ &u_x(x = 0,\, t) = -\dot{q}_{\text{in}}/\kappa \\ &u(x = l,\, t) = 0 \\ &u(x,\, t = 0) = 0,\ 0 \leq x \leq l \end{aligned} \tag{6.9}$$

The solution to this problem takes the form:

$$u(x,\, t) = u_E(x) + v(x,t) \tag{6.10}$$

where u_E is the steady-state solution. The ODE governing the steady-state heat conduction

problem is given by

$$\begin{aligned} \kappa \frac{\mathrm{d}^2 u_E}{\mathrm{d}x^2} &= 0 \\ \kappa \left. \frac{\mathrm{d}u_E}{\mathrm{d}x} \right|_{x=0} &= -\dot{q}_{\text{in}} \\ u_E(x = l) &= 0 \end{aligned} \tag{6.11}$$

so the solution to u_E is simply:

$$u_E(x) = \frac{\dot{q}_{\text{in}} l}{\kappa} \left(1 - {}^{x}/_{l}\right). \tag{6.12}$$

The solution to the transient component of the solution, $v(x,t)$, is given by

$$v(x,t) = \sum_{n=1}^{\infty} B_n \cos\left(\frac{n\pi}{2}\frac{x}{l}\right) e^{-\lambda \alpha t} \tag{6.13}$$

with the coefficients B_n given by

$$B_n = \frac{8 l \dot{q}_{\text{in}}}{\pi^2 m^2 \kappa} \left(\cos\left(\frac{\pi m}{2}\right) - 1\right);\ m = 2n - 1 \tag{6.14}$$

and the eigenvalues λ_n given by

$$\lambda_n = \left(\frac{n\pi}{2l}\right)^2. \tag{6.15}$$

The derivation which leads to this result is provided in Appendix section 8.3. Substituting Equation 6.12 and Equation 6.13 into Equation 6.10 results in the final solution:

$$u(x,t) = \frac{\dot{q}_{\text{in}} l}{\kappa} \left(1 - {}^{x}/_{l}\right) + \sum_{n=1}^{\infty} B_n \cos\left(\frac{n\pi}{2}\frac{x}{l}\right) e^{-\lambda \alpha t} \tag{6.16}$$

Figure 6.2 shows how the temperature in the domain evolves over time as the heat conduction trends towards steady-state. The results shown use 100 coefficients for the series term in Equation 6.16.

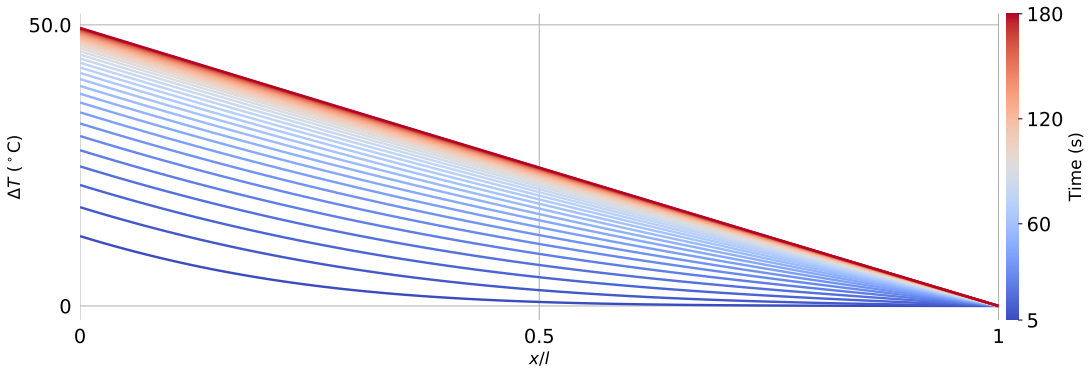

Figure 6.2: Spatial temperature distribution at different time steps

6.1.2 Validation of TACS transient heat transfer solution

Finally, the previous example is used to validate the transient heat transfer solution computed numerically using TACS. To show that TACS computes the solution of the transient heat transfer problem properly, the spatial maximum of the temperature is compared for the analytic solution, as well for as the numeric solution using a range of time steps. Figure 6.3 shows the relative error of the TACS transient heat transfer solution over time, for time step sizes of $\Delta t = 1$ s, $\Delta t = 2$ s, $\Delta t = 5$ s, and $\Delta t = 10$ s. The analytic solution is computed at 1 second intervals using 100 Fourier coefficients for Equation 6.16. Figure 6.3 indicates good agreement between the analytic and numeric solutions to the transient heat transfer problem. The error at $t = 0$ is not shown because this would lead to a division by zero, due to the zero initial conditions. The error for each TACS solutions converges to ~ 0, at different rates. The errors at the final time step for each TACS solution are provided in Table 6.1. The table also shows the first time where the relative error becomes less than 1% for each time step. The results show that the numerical integration is stable and produces accurate results even with very course time steps. This example uses a heat flux boundary condition which is constant over time, but if the heat flux were to vary over time, sufficient temporal resolution should be used to accurately represent the boundary conditions. Using the coarsest time step of 10 s, the relative error at the final time step is $5.4 \times 10^{-2}\%$. This indicates that we can confidently use a coarse time step for topology optimization, since a

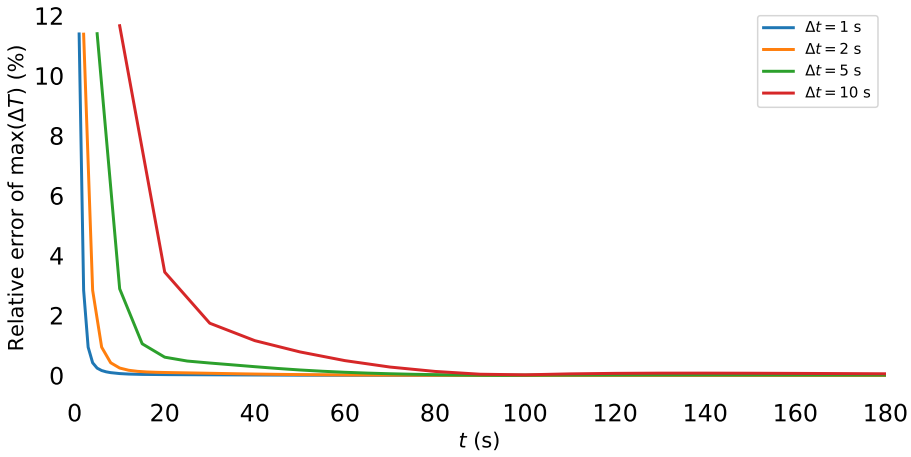

Figure 6.3: Validation of TACS solution to the analytic transient heat transfer example using a range of time step sizes

Table 6.1: Relative error of the the maximum temperature at the final time step comparing the analytic and numeric transient heat transfer solutions

Δt (s)	Relative error at final time (%)	Time when error drops below 1% (s)
1	4.7×10^{-4}	3.0
2	1.8×10^{-3}	6.0
5	1.2×10^{-2}	20.0
10	5.4×10^{-2}	50.0

high-degree of precision is not needed to produce the design.

6.2 Results

Figure 6.4a through Figure 6.4m show the results of topology optimization with transient analysis with the same boundary conditions as the steady-state result shown in Figure 6.4o. The topology optimization problem formulation here is a temperature minimization subject to stress- and mass-constraints, with the temperature and stress values of interest evaluated at the final time step of the transient analysis, as shown in the time-dependent topology optimization formulation (Equation 6.8). In the transient results shown here, the input heat flux is constant, but t_{final} is varied so that the physics is transient to varying degrees. Each case shown initially starts with a uniform mesh with 15,360 elements. After three cycles

of adaptive mesh refinement, the final meshes have between 254,211 and 311,577 total elements. A comparable uniformly refined mesh with the same resolution would have 983,040 total elements, which demonstrates a significant cost savings by using adaptive mesh refinement.

Figure 6.4a and Figure 6.4c shows the results with $t_{\text{final}} = 5$ and 10 seconds, respectively, with a concentration of material forming near the input heat flux. This design feature absorbs the input heat flux as there is not sufficient time to conduct the heat away via the top surface. A similar design feature is present for the results shown in Figure 6.4e, and Figure 6.4g, for the $t_{\text{final}} = 15$ and 20 second results, respectively. However, in these designs the members connecting the bottom edge to the top have thickened to conduct heat away from the heat source, resulting in a tapered vertical member. As the simulation time increases further, the designs for $t_{\text{final}} = 25$, 30, and 60 seconds all show significant resemblance. These topologies feature a uniformly thick vertical member to conduct heat from the heat source to the heat sink, with truss-like members elsewhere to carry the mechanical traction and satisfy the stress constraint. These designs look similar to the steady-state topology (Figure 6.4o), although the truss-like members are arranged in a slightly different pattern, and where a secondary heat conduction path was noticeable in the $t_{\text{final}} = 60$ design, this feature has thickened noticeably in the steady-state design. Table 6.2 provides the optimized maximum temperature objective values of each of the results. Here we see the objective values converging to the steady-state objective value, confirming that the designs not only appear similar, but perform similarly as well.

Each of the designs in Figure 6.4 is intended to minimize the maximum temperature for a given duration of heat flux input, while satisfying a stress constraint. With these optimized designs, we can now compare the time response of each design - taking each topology, and applying a constant heat flux to each for 60 seconds. Figure 6.5 shows the results of this analysis, with the maximum temperature plotted over time for each design. In addition to the legend, a point on each line is plotted to indicate the final time that each

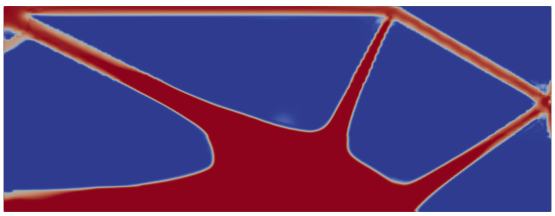

(a) $t_{\text{final}} = 5$ seconds

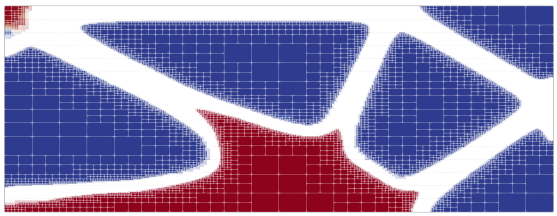

(b) $t_{\text{final}} = 5$ seconds with final mesh

(c) $t_{\text{final}} = 10$ seconds

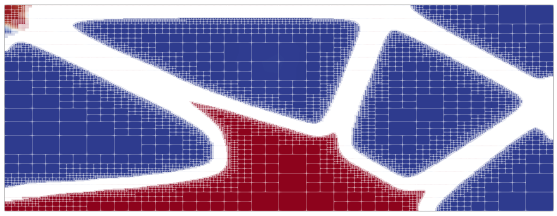

(d) $t_{\text{final}} = 10$ seconds with final mesh

(e) $t_{\text{final}} = 15$ seconds

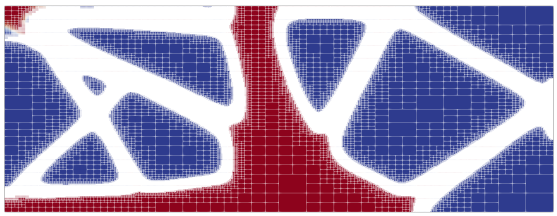

(f) $t_{\text{final}} = 15$ seconds with final mesh

(g) $t_{\text{final}} = 20$ seconds

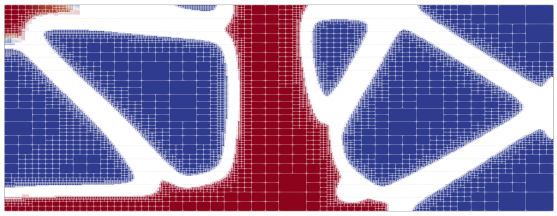

(h) $t_{\text{final}} = 20$ seconds with final mesh

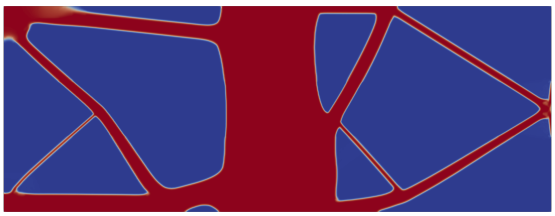

(i) $t_{\text{final}} = 25$ seconds

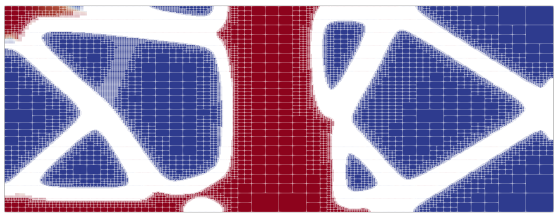

(j) $t_{\text{final}} = 25$ seconds with final mesh

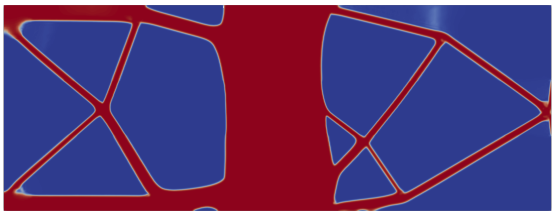

(k) $t_{\text{final}} = 30$ seconds

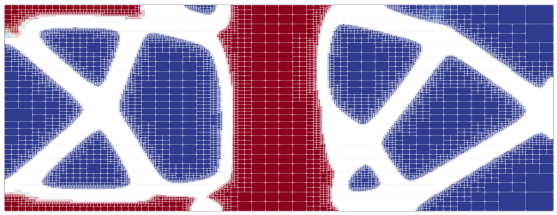

(l) $t_{\text{final}} = 30$ seconds with final mesh

Table 6.2: Final maximum temperature values for each optimization case

t_{final} (s)	$c_{\text{KS}}(\boldsymbol{\theta})^*$, (°C)
5	1.11
10	1.81
15	1.96
20	1.98
25	1.98
30	2.08
60	1.97
Steady-state	1.91

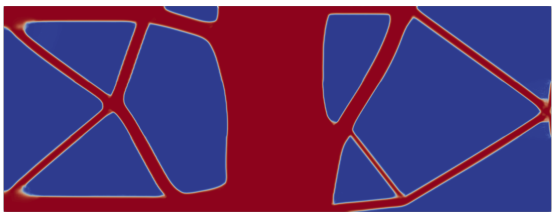

(m) $t_{\text{final}} = 60$ seconds

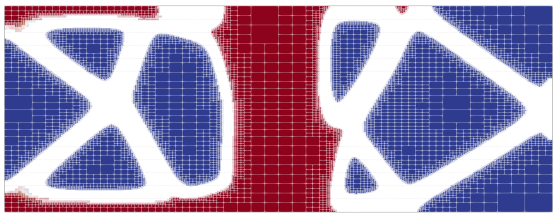

(n) $t_{\text{final}} = 60$ seconds with final mesh

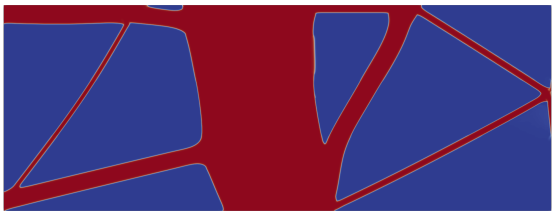

(o) Steady-state

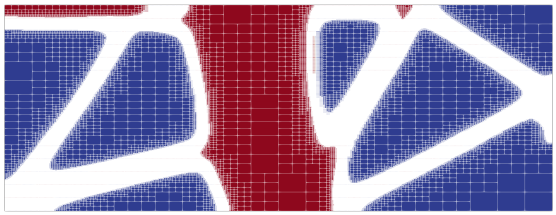

(p) Steady-state with final mesh

Figure 6.4: Optimized topologies using transient analysis with constant heat flux for a range of t_{final}

design was intended for (for the steady-state design, a point is placed at 60 seconds, since this is the boundary of the plot). One other way to think about this is that the optimization considers the time history of the transient heat conduction up to the point of each plotted circle. Note that the lines for $t_{\text{final}} = 25$ and $t_{\text{final}} = 30$ are indistinguishable in the plot; the time response the steady-state design and the $t_{\text{final}} = 60$ design nearly overlap as well. It is expected that the steady-state time response and the $t_{\text{final}} = 60$ time response match so closely, but notable that their performance is so similar with fairly different topologies. One might expect that the circles would be below all the other lines, meaning that when we

minimize the maximum temperature at a certain time, the optimized temperature should be lower than other designs at the same time. With the exception of $t_{\text{final}} = 60$, this is not what we see, though they are all close to being the minimum. The case of $t_{\text{final}} = 10$ is the greatest violation; the maximum temperature of the $t_{\text{final}} = 10$ design at 10 seconds is $2.03\ ^{\circ}\text{C}$, while the temperature of the $t_{\text{final}} = 60$ design at 10 seconds is $1.72\ ^{\circ}\text{C}$, which is 15.3% lower. The first reason this is not the case is that the stress constraints for each of these cases are all slightly different. The stress constraint is applied at t_{final} for each design, which makes this an imperfect comparison. Still, we would expect each to be close to the minimum at their respective times, and we do see that they all nearly meet that criteria. The second reason is that like we saw in the Pareto front (Figure 5.3), coupled thermoelastic topology optimizations can have many local minima, and the objective function values can jump significantly when there are discrete differences in the design like we see here. The final designs obey intuition - in that smaller values of t_{final} have more material close to the heat source, and higher values have more of a heat conduction path between the heat source and the heat sink. This ends up being reflected when comparing the temperatures at $t = 60$. $t_{\text{final}} = 5$ has the highest temperature at $t = 60$, followed by $t_{\text{final}} = 10$, since these two designs have prioritized short time-scale temperature minimization. The temperatures at $t = 60$ for the other topologies are closer to one another, and end up in order of t_{final} as well.

6.3 Conclusions

For structural design problems with combined mechanical and thermal loads, it is important to choose problem formulations which improve thermal performance while also considering material stress limits. Thermal loads are often transient, and we have shown here that the choice of transient or steady-state analysis can have a large impact on the design, depending on the degree to which the thermal loads are transient. Transient thermoelastic topology optimized designs with $\mathcal{O}(10^5)$ elements were generated for a range of input heat

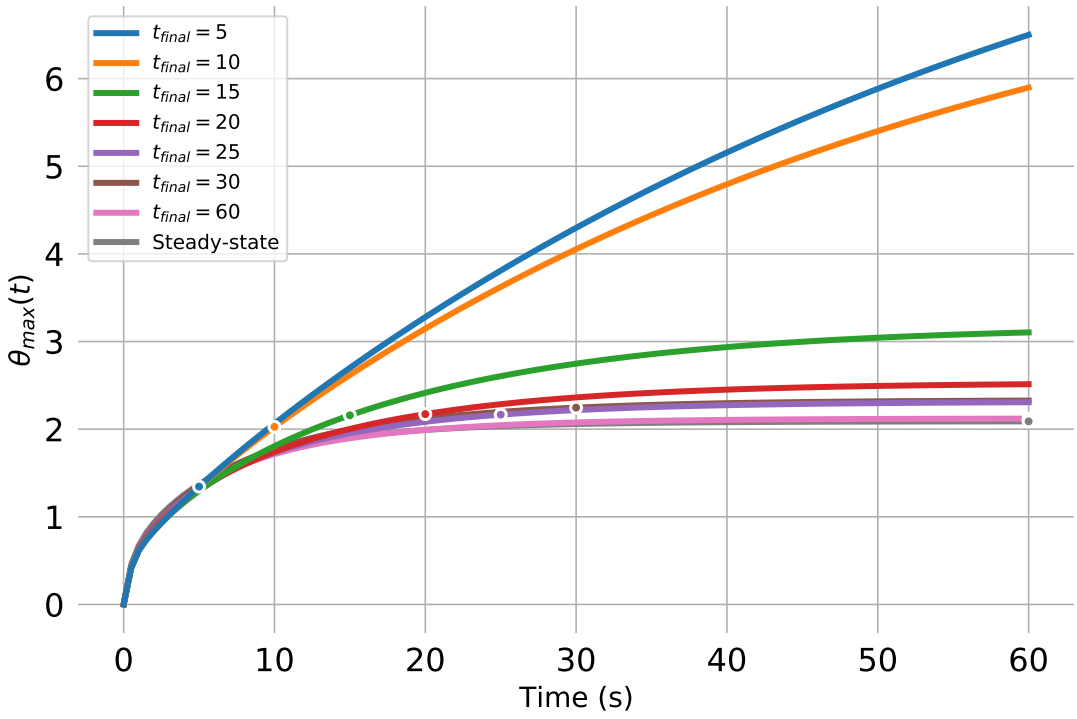

Figure 6.5: Time response of each of the optimized designs

flux duration. This was, to my knowledge, the first time that stress-constrained transient thermoelastic topology optimization has been presented. These designs were compared to a design generated using steady-state analysis. The expected result was confirmed: transient results with longer duration heat flux closely resemble designs generated with steady-state analysis, but shorter duration designs varied drastically.

CHAPTER 7
CONCLUSION

Topology optimization is a powerful design tool, benefiting from a broadened design space that can be efficiently navigated with gradient-based optimization algorithms. Complex design problems which often involve multiple, coupled physics may require the use of gradient-based optimization techniques to satisfy demanding design requirements. In addition to multiphysics analysis, structural optimization problem formulations must consider design stresses in order to produce feasible designs. Popular alternative formulations may produce overly stiff designs which also do not consider areas of stress concentration. Current topology optimization methods use physics modeling which is too simplistic for many design scenarios, and many do not consider design stress within the problem formulation. Finally, designs generated using topology optimization should be finely refined to achieve a smooth and detailed design.

This thesis increases the scope of physics modeling available for topology optimization, while also considering critical design stress limits. First, due to the high-vibration environments that are common with aerospace structures, unwanted frequency response of the structure must be avoided. To address stress- and frequency-constrained problems, stress constraints are formulated using a reconstruction of the displacement field that produces a stress field that is less mesh-sensitive and more amenable to stress-constrained optimization. To address the high computational cost of eigenvalue problems, the natural frequency problem is solved using a Jacobi–Davidson eigenvalue solution method that is compatible with iterative solution techniques. Novel eigenvector recycling strategies, which reuse eigenvector information, are proposed and evaluated. This combination of iterative eigenvalue solution method and recycling strategy enables the solution of high-resolution topology optimization problems with frequency constraints.

Second, many aerospace vehicles require structures to operate at high temperatures while simultaneously being subjected to mechanical loads. In some important design cases, these structures never reach thermal equilibrium. For instance, electric vehicles operate at high power conditions during takeoff, landing or hover, and will not reach thermal steady-state during these flight phases. In these applications, steady-state thermal analysis may not accurately capture thermal or mechanical performance. In this thesis, thermoelastic physics with both steady-state and transient heat transfer analysis is developed for topology optimization.

Each of these modeling domains require significant computational cost. The work in this thesis presents a novel adaptive mesh refinement technique where the mesh is refined adaptively near the solid-void boundary. This provides a substantial savings in computational cost, while providing highly refined designs, making these modeling approaches more viable for topology optimization design.

7.1 Contributions

1. *Solving stress- and frequency-constrained topology optimization problems using a Jacobi-Davidson eigenvalue solver*

   High-resolution topology optimization has the potential to be a powerful tool to design structures with strength requirements that operate in high-vibration environments. In order to solve these complex design problems, this work addressed challenges in applying stress and frequency constraints to large-scale topology optimization problems. An element-wise reconstruction of the displacement field enabled the computation of less mesh-sensitive strain and stress fields, improving the design space for stress-constrained optimization. This work also demonstrated that the Jacobi–Davidson method with eigenvector recycling is efficient and robust for solving large-scale natural-frequency problems for topology optimization applications. Finally, these capabilities were

demonstrated using cantilever and orthogonal bracket problems, with comparisons for stress-constrained mass minimization, mass-constrained compliance minimization, and stress- and frequency-constrained mass minimization for problems with $\mathcal{O}(10^7)$ degrees of freedom.

2. *Solving steady-state coupled thermoelastic topology optimization problems*

   In chapter 5 presented steady-state thermoelastic topology optimization methodology and results. Steady-state thermoelastic topology is not a new area of research; however, I presented a Pareto-front using 101 topology optimization results, providing a novel perspective on the competing nature of mechanical and thermal performance that makes thermoelastic structural design so challenging. I applied stress-constrained thermoelastic topology optimization to produce novel structural design concepts for the mounting structure of an electric motor. These designs are, to my knowledge, the largest stress-constrained thermoelastic topology optimization results presented, with 2,181,120 elements, 9,294,068 degrees of freedom, and 2,323,517 design variables. I presented results using two different choices of boundary conditions and found that the choice of boundary condition has a large impact on the resulting design. Additionally, designs generated without thermal loads were also presented to highlight the effect that the temperature increase has on the resulting design.

3. *Solving stress-constrained transient thermoelastic topology optimization problems*

   For structural design problems with combined mechanical and thermal loads, it is important to choose problem formulations which improve thermal performance while also considering material stress limits. Thermal loads are often transient, and I showed that the choice of transient or steady-state analysis can have a large impact on the design – depending on the degree to which the thermal loads are transient. Transient thermoelastic topology optimized designs with $\mathcal{O}(10^5)$ elements were generated for a range of input heat flux duration.

This was, to my knowledge, the first time that stress-constrained transient thermoelastic topology optimization has been presented. These designs were compared to a design generated using steady-state analysis. The expected result was confirmed: transient results with longer duration heat flux closely resemble designs generated with steady-state analysis, but shorter duration designs varied drastically. This work enables the use of transient thermoelastic physics for topology optimization problems for a broad scope of applications with transient heat transfer, including time-varying heat generation and cooling.

7.2 Future work

7.2.1 Trajectory and topology coupled optimization

In many applications where transient heat transfer is relevant, the thermal boundary conditions (both heat generation and cooling) depend on the operating conditions. For example, in the context of an electric aircraft motor, the heating is determined by the electric power required over time, and the convective cooling is a function of the aircraft's speed and altitude. Two-way coupling exists with this problem because the mission requirements determine thermal loads, but component thermal limits may then restrict the mission. For this type of problem and others like it, the topology optimization could be coupled to a trajectory optimization (for example, using Dymos[1]) to capture the effects of the two-way coupling inherent in the problem.

7.2.2 Natural and forced convection boundary conditions

Many authors have modeled natural and forced convection heat transfer with topology optimization to improve thermal performance [38, 39, 40, 41], but none have done so for stress-based coupled thermal-structural problems. Adding natural or forced convection boundary conditions to this work would enable high-fidelity coupled aero-thermal-structural topol-

[1] https://github.com/OpenMDAO/dymos

ogy optimization. Modeling convection enables the consideration of convective cooling for transient thermal design problems, which are relevant for many applications. This would greatly improve the modeling for coupled trajectory and topology optimization problems as well, in cases where the convective heat flux is a function of trajectory.

7.2.3 Topology optimization under uncertainty

This is a less obvious but an important consideration for future research. In the topology optimization process, many assumptions are made about material properties, geometry, loads, and boundary conditions, and as we add more layers of complexity to the analysis (i.e. thermoelastic governing equations, transient physics, trajectory modeling), the number of assumptions only increases from there. Additionally, based on the Pareto front shown in chapter 5, we know that topology optimization designs can experience discontinuous jumps in performance due to discrete changes in the design. In other words, topology optimization is sensitive to input parameters. Applying optimization under uncertainty concepts to topology optimization can help make these designs more robust to the uncertainty inherent in many of the assumptions that we have to make when we formulate a topology optimization problem.

CHAPTER 8

APPENDIX

8.1 Enrichment functions for reconstruction

In this work, the regular trilinear finite-element shape functions for 8-noded hexahedral elements are denoted $\mathbf{N}(\boldsymbol{\eta})$. The enrichment basis functions are constructed such that their values are zero at the nodes so that the nodal solution remains unchanged. For the trilinear case, the enrichment functions are based on the function

$$r(\eta_1) = (1+\eta_1)(1-\eta_1),$$

which is zero at $\eta_1 = -1$ and $\eta_1 = 1$. With this definition, the enrichment functions can be written as

$$\bar{\mathbf{N}}(\boldsymbol{\eta})^T = \begin{bmatrix} r(\eta_1) & \eta_2 r(\eta_1) & \eta_3 r(\eta_1) & r(\eta_2) & \eta_1 r(\eta_2) & \eta_3 r(\eta_2) & r(\eta_3) & \eta_1 r(\eta_3) & \eta_2 r(\eta_3) \end{bmatrix}$$

The matrices $\mathbf{A}_x \in \mathbb{R}^{24\times 8}$ and $\bar{\mathbf{A}}_x \in \mathbb{R}^{24\times 9}$ are the three spatial derivatives of $\mathbf{N}(\boldsymbol{\eta})$ and $\bar{\mathbf{N}}(\boldsymbol{\eta})$ evaluated at each of the 8 node locations. Given the parametric node locations $\boldsymbol{\eta}_i$,

for $i = 1, \ldots, 8$, these matrices can be written as

$$\mathbf{A}_x = \begin{bmatrix} \mathbf{N}_{,x}(\boldsymbol{\eta}_1)^T \\ \mathbf{N}_{,y}(\boldsymbol{\eta}_1)^T \\ \mathbf{N}_{,z}(\boldsymbol{\eta}_1)^T \\ \vdots \\ \mathbf{N}_{,x}(\boldsymbol{\eta}_8)^T \\ \mathbf{N}_{,y}(\boldsymbol{\eta}_8)^T \\ \mathbf{N}_{,z}(\boldsymbol{\eta}_8)^T \end{bmatrix}, \qquad \bar{\mathbf{A}}_x = \begin{bmatrix} \bar{\mathbf{N}}_{,x}(\boldsymbol{\eta}_1)^T \\ \bar{\mathbf{N}}_{,y}(\boldsymbol{\eta}_1)^T \\ \bar{\mathbf{N}}_{,z}(\boldsymbol{\eta}_1)^T \\ \vdots \\ \bar{\mathbf{N}}_{,x}(\boldsymbol{\eta}_8)^T \\ \bar{\mathbf{N}}_{,y}(\boldsymbol{\eta}_8)^T \\ \bar{\mathbf{N}}_{,z}(\boldsymbol{\eta}_8)^T \end{bmatrix},$$

where the comma notation here denotes differentiation with respect to a coordinate direction.

8.2 Jacobi–Davidson method

Algorithm 3 Jacobi–Davidson method with recycling

Set $k = 0$
while $k \leq s$ **do** ▷ Orthogonalize initial set of recycled vectors
  Set $\mathbf{v}_k \leftarrow \text{ModifiedGramSchmidt}(\mathbf{M}, \mathbf{V}_{k-1}, \mathbf{R}_s\mathbf{e}_k)$ ▷ Extract column k from $\mathbf{R}_s$ and orthogonalize it
  Set $k = k + 1$
end while
Compute $\mathbf{A}_s = \mathbf{V}_s^T\mathbf{K}\mathbf{V}_s$ ▷ Compute the initial reduced matrix
Set $\mathbf{E}_k = \emptyset$ ▷ Set the converged eigenvectors to the empty set
Set $k = s$
while $k \leq$ max iterations **do**
  if $k > s$ **then** ▷ Skip this orthogonalization step when $k = s$
    Set $\mathbf{v}_k \leftarrow \text{ModifiedGramSchmidt}(\mathbf{M}, \mathbf{E}_k, \mathbf{v}_k)$ ▷ Orthogonalize $\mathbf{v}_k$ against converged eigenvectors $\mathbf{E}_k$
    Set $\mathbf{v}_k \leftarrow \text{ModifiedGramSchmidt}(\mathbf{M}, \mathbf{V}_{k-1}, \mathbf{v}_k)$ ▷ Orthogonalize $\mathbf{v}_k$ against $\mathbf{V}_{k-1}$
    Compute $\mathbf{w} = \mathbf{K}\mathbf{v}_k$
    Compute new row/column of $\mathbf{A}_k$ where $[\mathbf{A}_k]_{jk} = \mathbf{w}^T\mathbf{v}_j$ and $[\mathbf{A}_k]_{kj} = \mathbf{w}^T\mathbf{v}_j$
  end if
  Solve the eigenproblem $\mathbf{A}_k\mathbf{y} = \theta\mathbf{y}$
  Compute for the lowest Ritz vector $\mathbf{u}_1 = \mathbf{V}_k\mathbf{y}_1$
  Compute the residual $\mathbf{r} = \mathbf{K}\mathbf{u}_1 - \theta_1\mathbf{M}\mathbf{u}_1$
  if $||\mathbf{r}||_2 \leq \epsilon||\mathbf{K}\mathbf{u}_1||_2$ **then** ▷ Check for convergence of this Ritz pair
    Add $\mathbf{u}_1$ to the converged eigenvectors $\mathbf{E}_k = \mathbf{E}_{k-1} \cup \mathbf{u}_1$
    if required eigenvectors converged **then**
      break ▷ All eigenvalues and eigenvectors converged
    end if
    Compute $\mathbf{u}_2 = \mathbf{V}_k\mathbf{y}_2$, $\mathbf{r} = \mathbf{K}\mathbf{u}_2 - \theta_2\mathbf{M}\mathbf{u}_2$ ▷ Switch to the next Ritz pair
    Set $\mathbf{u}_1 \leftarrow \mathbf{u}_2$
  else
    Set $\mathbf{E}_k = \mathbf{E}_{k-1}$
  end if
  Set $\mathbf{Q}_k = \mathbf{E}_k \cup \mathbf{u}_1$
  Use FGMRES to approximately solve the update equation

$$(\mathbf{I} - \mathbf{M}\mathbf{Q}_k\mathbf{Q}_k^T)(\mathbf{K} - \theta\mathbf{M})(\mathbf{I} - \mathbf{Q}_k\mathbf{Q}_k^T\mathbf{M})\mathbf{t} = -\mathbf{r}$$

  Set $\mathbf{v}_{k+1} = \mathbf{t}$
  Set $k = k + 1$
end while

8.3 The analytic solution to the transient heat conduction validation problem

This section provides a derivation for the solution to the transient component of the heat conduction validation problem presented in Section subsection 6.1.1. The PDE governing the transient component of the solution, $v(x,t)$, is:

$$\begin{aligned} &v_t = \alpha v_{xx};\ \alpha = \frac{\kappa}{\rho c_p} \\ &v_x(x=0,\,t) = -\dot{q}_{\text{in}}/\kappa \\ &v(x=l,\,t) = 0 \\ &v(x,\,t=0) = -u_E(x) = -\frac{\dot{q}_{\text{in}} l}{\kappa}(1 - {}^{x}/_{l}) \end{aligned} \tag{8.1}$$

The solution to $v(x,t)$ follows.

$$v(x,t) = X(x)T(t) \tag{8.2}$$

$$X(x)\dot{T}(t) = \alpha X''(x)T(t) \tag{8.3}$$

$$\begin{aligned} X'' + \lambda X &= 0 \\ \dot{T} + \lambda\alpha T &= 0 \end{aligned} \tag{8.4}$$

$$X(x) = A\sin(\sqrt{\lambda}) + B\cos(\sqrt{\lambda}) \tag{8.5}$$

$$X'(0) = A\sqrt{\lambda} = 0 \rightarrow A = 0 \tag{8.6}$$

$$X(l) = B\cos(\sqrt{\lambda}l) = 0 \rightarrow \lambda_n = \left(\frac{n\pi}{2l}\right)^2 \tag{8.7}$$

$$X(x) = \sum_{n=1}^{\infty} B_n \cos\left(\frac{n\pi}{2}\frac{x}{l}\right) \tag{8.8}$$

$$\dot{T} = -\lambda\alpha T \tag{8.9}$$

$$\implies T_n = C_n e^{-\lambda\alpha t} \tag{8.10}$$

$$\implies v(x,t) = \sum_{n=1}^{\infty} B_n \cos\left(\frac{n\pi}{2}\frac{x}{l}\right) e^{-\lambda\alpha t} \tag{8.11}$$

$$v(x,0) = -u_E(x) = \sum_{n=1}^{\infty} v_n(x,0) = \sum_{n=1}^{\infty} B_n \cos\left(\frac{n\pi}{2}\frac{x}{l}\right) \tag{8.12}$$

$$B_n = \frac{2}{l}\int_0^l \cos\left(\frac{(2n-1)\pi}{2}\frac{x}{l}\right)(-u_E(x))\,dx \tag{8.13}$$

$$B_n = \frac{8l\dot{q}_{\text{in}}}{\pi^2 m^2 \kappa}\left(\cos\left(\frac{\pi m}{2}\right) - 1\right);\ m = 2n-1 \tag{8.14}$$

REFERENCES

[1] PACE, *Partnership for an Advanced Computing Environment (PACE)*, 2017. [Online]. Available: http://www.pace.gatech.edu.

[2] M. P. Bendsøe and N. Kikuchi, "Generating optimal topologies in structural design using a homogenization method," *Computer Methods in Applied Mechanics and Engineering*, vol. 71, no. 2, pp. 197 –224, 1988. DOI: 10.1016/0045-7825(88)90086-2.

[3] S. Osher and J. A. Sethian, "Fronts propagating with curvature-dependent speed: Algorithms based on Hamilton-Jacobi formulations," *Journal of Computational Physics*, vol. 79, no. 1, pp. 12–49, 1988. DOI: 10.1016/0021-9991(88)90002-2.

[4] L. Krog, A. Tucker, M. Kemp, and R. Boyd, "Topology optimisation of aircraft wing box ribs," in *10th AIAA/ISSMO Multidisciplinary Analysis and Optimization Conference*, AIAA 2004-4481, Albany, NY, Aug. 2004. DOI: 10.2514/6.2004-4481.

[5] S. Grihon, L. Krog, and K. Hertel, "A380 weight savings using numerical structural optimization," in *20th AAAF Colloqium on Material for Aerospace Applications*, Paris, France, Nov. 2004, pp. 763–766.

[6] S. Buchanan, "Development of a wingbox rib for a passenger jet aircraft using design optimization and constrained to traditional design and manufacture requirements," in *10th UK Altair Technology Conference*, Altair Engineering, Warwickshire, UK, Sep. 2007. [Online]. Available: https://altairatc.com/EventPage.aspx?event_id=97&name=Conference+Papers+-+2007.

[7] M. D. Moore, "Misconceptions of electric aircraft and their emerging aviation markets," in *52nd Aerospace Sciences Meeting*, AIAA 2014-0535, 2014. DOI: 10.2514/6.2014-0535.

[8] T. Zeng, H. Wang, M. Yang, and J. Alexandersen, "Topology optimization of heat sinks for instantaneous chip cooling using a transient pseudo-3D thermofluid model," *International Journal of Heat and Mass Transfer*, vol. 154, p. 119 681, 2020. DOI: 10.1016/j.ijheatmasstransfer.2020.119681.

[9] H Rodrigues and P Fernandes, "A material based model for topology optimization of thermoelastic structures," *International Journal for Numerical Methods in Engineering*, vol. 38, no. 12, pp. 1951–1965, 1995. DOI: 10.1002/nme.1620381202.

[10] O. Sigmund and S. Torquato, "Design of materials with extreme thermal expansion using a three-phase topology optimization method," *Journal of the Mechanics and*

Physics of Solids, vol. 45, no. 6, pp. 1037–1067, 1997. DOI: 10.1016/S0022-5096(96)00114-7.

[11] J.-B. Bouquet, F. Burgaud, and J. J. Rimoli, "Exploiting length-dependent effects for the design of single-material systems with enhanced thermal transport properties," *International Journal of Heat and Mass Transfer*, vol. 101, pp. 1227–1236, 2016. DOI: 10.1016/j.ijheatmasstransfer.2016.05.122.

[12] B. Stanford and P. Beran, "Aerothermoelastic topology optimization with flutter and buckling metrics," *Structural and Multidisciplinary Optimization*, vol. 48, no. 1, pp. 149–171, Jul. 2013. DOI: 10.1007/s00158-013-0885-x.

[13] C. Lundgaard and O. Sigmund, "A density-based topology optimization methodology for thermoelectric energy conversion problems," *Structural and Multidisciplinary Optimization*, vol. 57, no. 4, pp. 1427–1442, 2018. DOI: 10.1007/s00158-018-1919-1.

[14] H. Chung, O. Amir, and H. A. Kim, "Nonlinear thermoelastic topology optimization with the level-set method," in *AIAA Scitech 2019 Forum*, AIAA 2019-1470, San Diego, CA, 2019. DOI: 10.2514/6.2019-1470.

[15] T. W. Chin and G. J. Kennedy, "Efficient large-scale thermoelastic topology optimization of CAD geometry with automated adaptive mesh generation," in *59th AIAA/ASCE/AHS/ASC Structures, Structural Dynamics, and Materials Conference, AIAA SciTech*, AIAA 2018-1381, Kissimmee, FL, Jan. 2018. DOI: 10.2514/6.2018-1381.

[16] Q. Xia and M. Y. Wang, "Topology optimization of thermoelastic structures using level set method," *Computational Mechanics*, vol. 42, no. 6, p. 837, 2008. DOI: 10.1007/s00466-008-0287-x.

[17] S. Kambampati and H. A. Kim, "Level set topology optimization of load carrying heat dissipation devices," in *AIAA Aviation 2019 Forum*, AIAA 2019-3558, Jun. 2019. DOI: 10.2514/6.2019-3558.

[18] B. Curzadd, A. von Müller, R. Neu, and U. von Toussaint, "Topology optimization of tungsten/copper structures for plasma-facing component applications," *Nuclear Fusion*, 2019. DOI: 10.1088/1741-4326/ab1ff5.

[19] M. K. Leader, T. W. Chin, and G. J. Kennedy, "Thermomechanical design of electric vehicle components with mission performance requirements using topology optimization," in *AIAA Aviation 2019 Forum*, AIAA 2019-3557, Dallas, TX, 2019. DOI: 10.2514/6.2019-3557.

[20] J. D. Deaton and R. V. Grandhi, "Stress-based design of thermal structures via topology optimization," *Structural and Multidisciplinary Optimization*, vol. 53, no. 2, pp. 253–270, 2016. DOI: 10.1007/s00158-015-1331-z.

[21] S. Deng and K. Suresh, "Stress constrained thermo-elastic topology optimization with varying temperature fields via augmented topological sensitivity based level-set," *Structural and Multidisciplinary Optimization*, vol. 56, no. 6, pp. 1413–1427, 2017. DOI: 10.1007/s00158-017-1732-2.

[22] J. D. Deaton and R. V. Grandhi, "Stiffening of restrained thermal structures via topology optimization," *Structural and Multidisciplinary Optimization*, vol. 48, no. 4, pp. 731–745, 2013. DOI: 10.1007/s00158-013-0934-5.

[23] S. Guanghui, G. Chengqi, Q. Dongliang, W. Dongtao, T. Lei, and G. Tong, "An aerospace bracket designed by thermo-elastic topology optimization and manufactured by additive manufacturing," *Chinese Journal of Aeronautics*, 2019. DOI: 10.1016/j.cja.2019.09.006.

[24] X. Zhu, C. Zhao, X. Wang, Y. Zhou, P. Hu, and Z.-D. Ma, "Temperature-constrained topology optimization of thermo-mechanical coupled problems," *Engineering Optimization*, pp. 1–23, 2019. DOI: 10.1080/0305215X.2018.1554065.

[25] C. Zhuang, Z. Xiong, and H. Ding, "Topology optimization of multi-material for the heat conduction problem based on the level set method," *Engineering Optimization*, vol. 42, no. 9, pp. 811–831, 2010. DOI: 10.1080/03052150903443780.

[26] Q. Xia, T. Shi, and L. Xia, "Topology optimization for heat conduction by combining level set method and beso method," *International Journal of Heat and Mass Transfer*, vol. 127, pp. 200–209, 2018. DOI: 10.1016/j.ijheatmasstransfer.2018.08.036.

[27] S.-H. Ha and S. Cho, "Topological shape optimization of heat conduction problems using level set approach," *Numerical Heat Transfer, Part B: Fundamentals*, vol. 48, no. 1, pp. 67–88, 2005. DOI: 10.1080/10407790590935966.

[28] K. E. Jensen, "Solving 2D/3D heat conduction problems by combining topology optimization and anisotropic mesh adaptation," in *World Congress of Structural and Multidisciplinary Optimisation*, Springer, 2017, pp. 1224–1238. DOI: 10.1007/978-3-319-67988-4_92.

[29] S. Yan, F. Wang, and O. Sigmund, "On the non-optimality of tree structures for heat conduction," *International Journal of Heat and Mass Transfer*, vol. 122, pp. 660–680, 2018. DOI: 10.1016/j.ijheatmasstransfer.2018.01.114.

[30] S. Yan, F. Wang, J. Hong, and O. Sigmund, "Topology optimization of microchannel heat sinks using a two-layer model," *International Journal of Heat and Mass Transfer*, vol. 143, p. 118 462, 2019. DOI: 10.1016/j.ijheatmasstransfer.2019.118462.

[31] Q. Li, G. P. Steven, Y. Xie, and O. M. Querin, "Evolutionary topology optimization for temperature reduction of heat conducting fields," *International Journal of Heat and Mass Transfer*, vol. 47, no. 23, pp. 5071–5083, 2004. DOI: 10.1016/j.ijheatmasstransfer.2004.06.010.

[32] A. Gersborg-Hansen, M. P. Bendsøe, and O. Sigmund, "Topology optimization of heat conduction problems using the finite volume method," *Structural and Multidisciplinary Optimization*, vol. 31, no. 4, pp. 251–259, 2006. DOI: 10.1007/s00158-005-0584-3.

[33] T Gao, W. Zhang, J. Zhu, Y. Xu, and D. Bassir, "Topology optimization of heat conduction problem involving design-dependent heat load effect," *Finite Elements in Analysis and Design*, vol. 44, no. 14, pp. 805–813, 2008. DOI: 10.1016/j.finel.2008.06.001.

[34] L. Tang, T. Gao, L. Song, L. Meng, C. Zhang, and W. Zhang, "Topology optimization of nonlinear heat conduction problems involving large temperature gradient," *Computer Methods in Applied Mechanics and Engineering*, vol. 357, p. 112 600, 2019. DOI: 10.1016/j.cma.2019.112600.

[35] H. A. Jahangiry and A. Jahangiri, "Combination of isogeometric analysis and level-set method in topology optimization of heat-conduction systems," *Applied Thermal Engineering*, vol. 161, p. 114 134, 2019. DOI: 10.1016/j.applthermaleng.2019.114134.

[36] L. G. Page, J. Dirker, and J. P. Meyer, "Topology optimization for the conduction cooling of a heat-generating volume with orthotropic material," *International Journal of Heat and Mass Transfer*, vol. 103, pp. 1075–1083, 2016. DOI: 10.1016/j.ijheatmasstransfer.2016.08.020.

[37] Y. Zhang and S. Liu, "Design of conducting paths based on topology optimization," *Heat and Mass Transfer*, vol. 44, no. 10, pp. 1217–1227, 2008. DOI: 10.1007/s00231-007-0365-1.

[38] P. Coffin and K. Maute, "Level set topology optimization of cooling and heating devices using a simplified convection model," *Structural and Multidisciplinary Optimization*, vol. 53, no. 5, pp. 985–1003, 2016. DOI: 10.1007/s00158-015-1343-8.

[39] D. Makhija and K. Maute, "Level set topology optimization of scalar transport problems," *Structural and Multidisciplinary Optimization*, vol. 51, no. 2, pp. 267–285, 2015. DOI: 10.1007/s00158-014-1142-7.

[40] M. Zhou, J. Alexandersen, O. Sigmund, and C. B. Pedersen, "Industrial application of topology optimization for combined conductive and convective heat transfer problems," *Structural and Multidisciplinary Optimization*, vol. 54, no. 4, pp. 1045–1060, 2016. DOI: 10.1007/s00158-016-1433-2.

[41] J. K. Guest and J. H. Prévost, "Topology optimization of creeping fluid flows using a Darcy–Stokes finite element," *International Journal for Numerical Methods in Engineering*, vol. 66, no. 3, pp. 461–484, 2006. DOI: 10.1002/nme.1560.

[42] J. Asmussen, J. Alexandersen, O. Sigmund, and C. S. Andreasen, "A "poor man's" approach to topology optimization of natural convection problems," *Structural and Multidisciplinary Optimization*, vol. 59, no. 4, pp. 1105–1124, 2019. DOI: 10.1007/s00158-019-02215-9.

[43] N. Pollini, O. Sigmund, C. S. Andreasen, and J. Alexandersen, "A "poor man's" approach for high-resolution three-dimensional topology design for natural convection problems," *Advances in Engineering Software*, vol. 140, p. 102 736, 2020. DOI: 10.1016/j.advengsoft.2019.102736.

[44] J. Alexandersen, N. Aage, C. S. Andreasen, and O. Sigmund, "Topology optimisation for natural convection problems," *International Journal for Numerical Methods in Fluids*, vol. 76, no. 10, pp. 699–721, 2014. DOI: 10.1002/fld.3954.

[45] J. Alexandersen, O. Sigmund, and N. Aage, "Large scale three-dimensional topology optimisation of heat sinks cooled by natural convection," *International Journal of Heat and Mass Transfer*, vol. 100, pp. 876–891, 2016. DOI: 10.1016/j.ijheatmasstransfer.2016.05.013.

[46] Y. Joo, I. Lee, and S. J. Kim, "Efficient three-dimensional topology optimization of heat sinks in natural convection using the shape-dependent convection model," *International Journal of Heat and Mass Transfer*, vol. 127, pp. 32–40, 2018. DOI: 10.1016/j.ijheatmasstransfer.2018.08.009.

[47] K. Yaji, T. Yamada, S. Kubo, K. Izui, and S. Nishiwaki, "A topology optimization method for a coupled thermal–fluid problem using level set boundary expressions," *International Journal of Heat and Mass Transfer*, vol. 81, pp. 878–888, 2015. DOI: 10.1016/j.ijheatmasstransfer.2014.11.005.

[48] S. B. Dilgen, C. B. Dilgen, D. R. Fuhrman, O. Sigmund, and B. S. Lazarov, "Density based topology optimization of turbulent flow heat transfer systems," *Struc-*

tural and Multidisciplinary Optimization, vol. 57, no. 5, pp. 1905–1918, 2018. DOI: 10.1007/s00158-018-1967-6.

[49] J. H. Haertel, K. Engelbrecht, B. S. Lazarov, and O. Sigmund, "Topology optimization of a pseudo 3D thermofluid heat sink model," *International Journal of Heat and Mass Transfer*, vol. 121, pp. 1073–1088, 2018. DOI: 10.1016/j.ijheatmasstransfer.2018.01.078.

[50] A. A. Koga, E. C. C. Lopes, H. F. V. Nova, C. R. De Lima, and E. C. N. Silva, "Development of heat sink device by using topology optimization," *International Journal of Heat and Mass Transfer*, vol. 64, pp. 759–772, 2013. DOI: 10.1016/j.ijheatmasstransfer.2013.05.007.

[51] T. Matsumori, T. Kondoh, A. Kawamoto, and T. Nomura, "Topology optimization for fluid–thermal interaction problems under constant input power," *Structural and Multidisciplinary Optimization*, vol. 47, no. 4, pp. 571–581, 2013. DOI: 10.1007/s00158-013-0887-8.

[52] T. Matsumori, A. Kawamoto, and T. Kondoh, "Topology optimization for thermal stress reduction in power semiconductor module," *Structural and Multidisciplinary Optimization*, pp. 1–6, 2019. DOI: 10.1007/s00158-019-02341-4.

[53] S. Kambampati, C. Jauregui, K. Museth, and H. A. Kim, "Large-scale level set topology optimization for elasticity and heat conduction," *Structural and Multidisciplinary Optimization*, vol. 61, no. 1, pp. 19–38, 2020. DOI: 10.1007/s00158-019-02440-2.

[54] T. Gao and W. Zhang, "Topology optimization involving thermo-elastic stress loads," *Structural and Multidisciplinary Optimization*, vol. 42, no. 5, pp. 725–738, 2010. DOI: 10.1007/s00158-010-0527-5.

[55] T. Gao, P. Xu, and W. Zhang, "Topology optimization of thermo-elastic structures with multiple materials under mass constraint," *Computers & Structures*, vol. 173, pp. 150–160, 2016. DOI: 10.1016/j.compstruc.2016.06.002.

[56] T. W. Chin and G. J. Kennedy, "Multimaterial thermoelastic stress-constrained topology optimization of structures with adaptive mesh refinement," in *2018 Multidisciplinary Analysis and Optimization Conference*, AIAA 2018-4054, Atlanta, GA, Jun. 2018. DOI: 10.2514/6.2018-4054.

[57] Z. Kang and K. A. James, "Multimaterial topology design for optimal elastic and thermal response with material-specific temperature constraints," *International Journal for Numerical Methods in Engineering*, vol. 117, no. 10, pp. 1019–1037, 2019. DOI: 10.1002/nme.5989.

[58] P. Pedersen and N. L. Pedersen, "Interpolation/penalization applied for strength design of 3D thermoelastic structures," *Structural and Multidisciplinary Optimization*, vol. 45, no. 6, pp. 773–786, 2012. DOI: 10.1007/s00158-011-0755-3.

[59] ——, "Strength optimized designs of thermoelastic structures," *Structural and Multidisciplinary Optimization*, vol. 42, no. 5, pp. 681–691, 2010. DOI: 10.1007/s00158-010-0535-5.

[60] D. J. Lohan, E. M. Dede, and J. T. Allison, "A study on practical objectives and constraints for heat conduction topology optimization," *Structural and Multidisciplinary Optimization*, vol. 61, no. 2, pp. 475–489, 2020. DOI: 10.1007/s00158-019-02369-6.

[61] P. Duysinx and M. P. Bendsøe, "Topology optimization of continuum structures with local stress constraints," *International Journal for Numerical Methods in Engineering*, vol. 43, no. 8, pp. 1453–1478, 1998. DOI: 10.1002/(SICI)1097-0207(19981230)43:8⟨1453::AID-NME480⟩3.0.CO;2-2.

[62] G. Cheng, "Some aspects of truss topology optimization," *Structural and Multidisciplinary Optimization*, vol. 10, pp. 173–179, 3 1995. DOI: 10.1007/BF01742589.

[63] G. D. Cheng and X. Guo, "ϵ-relaxed approach in structural topology optimization," *Structural and Multidisciplinary Optimization*, vol. 13, pp. 258–266, 4 1997. DOI: 10.1007/BF01197454.

[64] C. Le, J. Norato, T. Bruns, C. Ha, and D. Tortorelli, "Stress-based topology optimization for continua," *Structural and Multidisciplinary Optimization*, vol. 41, pp. 605–620, 4 2010. DOI: 10.1007/s00158-009-0440-y.

[65] M. K. Leader, T. W. Chin, and G. J. Kennedy, "High-resolution topology optimization with stress and natural frequency constraints," *AIAA Journal*, pp. 1–17, 2019. DOI: 10.2514/1.J057777.

[66] J. Guedes, E. Lubrano, H. Rodrigues, and S. Turteltaub, "Hierarchical optimization of material and structure for thermal transient problems," in *IUTAM Symposium on Topological Design Optimization of Structures, Machines and Materials*, Springer, 2006, pp. 527–536.

[67] K. Long, X. Wang, and X. Gu, "Multi-material topology optimization for the transient heat conduction problem using a sequential quadratic programming algorithm," *Engineering Optimization*, vol. 50, no. 12, pp. 2091–2107, 2018. DOI: 10.1080/0305215X.2017.1417401.

[68] C. Zhuang, Z. Xiong, and H. Ding, "Topology optimization of the transient heat conduction problem on a triangular mesh," *Numerical Heat Transfer, Part B: Fun-*

damentals, vol. 64, no. 3, pp. 239–262, 2013. DOI: 10.1080/10407790.2013.791785.

[69] C. Zhuang and Z. Xiong, "A global heat compliance measure based topology optimization for the transient heat conduction problem," *Numerical Heat Transfer, Part B: Fundamentals*, vol. 65, no. 5, pp. 445–471, 2014. DOI: 10.1080/10407790.2013.873309.

[70] ——, "Temperature-constrained topology optimization of transient heat conduction problems," *Numerical Heat Transfer, Part B: Fundamentals*, vol. 68, no. 4, pp. 366–385, 2015. DOI: 10.1080/10407790.2015.1033306.

[71] Y. Li, K. Saitou, and N. Kikuchi, "Topology optimization of thermally actuated compliant mechanisms considering time-transient effect," *Finite Elements in Analysis and Design*, vol. 40, no. 11, pp. 1317–1331, 2004. DOI: 10.1016/j.finel.2003.05.002.

[72] S. Wu, Y. Zhang, and S. Liu, "Transient thermal dissipation efficiency based method for topology optimization of transient heat conduction structures," *International Journal of Heat and Mass Transfer*, vol. 170, p. 121 004, 2021. DOI: 10.1016/j.ijheatmasstransfer.2021.121004.

[73] P. Coffin and K. Maute, "A level-set method for steady-state and transient natural convection problems," *Structural and Multidisciplinary Optimization*, vol. 53, no. 5, pp. 1047–1067, 2016. DOI: 10.1007/s00158-015-1377-y.

[74] Q. Li, G. P. Steven, and Y. Xie, "Thermoelastic topology optimization for problems with varying temperature fields," *Journal of Thermal Stresses*, vol. 24, no. 4, pp. 347–366, 2006. DOI: 10.1080/01495730151078153.

[75] J. Deng, J. Yan, and G. Cheng, "Multi-objective concurrent topology optimization of thermoelastic structures composed of homogeneous porous material," *Structural and Multidisciplinary Optimization*, vol. 47, no. 4, pp. 583–597, 2013. DOI: 10.1007/s00158-012-0849-6.

[76] Z. Kang and K. A. James, "Thermomechanical topology optimization of shape-memory alloy structures using a transient bilevel adjoint method," *International Journal for Numerical Methods in Engineering*, vol. 121, no. 11, pp. 2558–2580, 2020. DOI: 10.1002/nme.6319.

[77] L. A. M. Mello, R. A. Salas, and E. C. N. Silva, "On response time reduction of electrothermomechanical MEMS using topology optimization," *Computer Methods in Applied Mechanics and Engineering*, vol. 247, pp. 93–102, 2012. DOI: 10.1016/j.cma.2012.08.008.

[78] R. Grandhi, "Structural optimization with frequency constraints – a review," *AIAA Journal*, vol. 31, no. 12, pp. 2296–2303, 1993. DOI: 10.2514/3.11928.

[79] R. Grandhi and V. Venkayya, "Structural optimization with frequency constraints," *AIAA Journal*, vol. 26, no. 7, pp. 858–866, 1988.

[80] B. Xu, J. Jiang, W. Tong, and K. Wu, "Topology group concept for truss topology optimization with frequency constraints," *Journal of Sound and Vibration*, vol. 261, no. 5, pp. 911–925, 2003.

[81] N. L. Pedersen, "Maximization of eigenvalues using topology optimization," *Structural and Multidisciplinary Optimization*, vol. 20, no. 1, pp. 2–11, 2000.

[82] L. Shu, M. Y. Wang, Z. Fang, Z. Ma, and P. Wei, "Level set based structural topology optimization for minimizing frequency response," *Journal of Sound and Vibration*, vol. 330, no. 24, pp. 5820–5834, 2011.

[83] F. Ferrari, B. S. Lazarov, and O. Sigmund, "Eigenvalue topology optimization via efficient multilevel solution of the frequency response," *International Journal for Numerical Methods in Engineering*, vol. 115, no. 7, pp. 872–892, 2018. DOI: 10.1002/nme.5829.

[84] P. D. Dunning, E. Ovtchinnikov, J. Scott, and H. A. Kim, "Level-set topology optimization with many linear buckling constraints using an efficient and robust eigensolver," *International Journal for Numerical Methods in Engineering*, vol. 107, no. 12, pp. 1029–1053, 2016. DOI: 10.1002/nme.5203.

[85] R. G. Grimes, J. G. Lewis, and H. D. Simon, "A shifted block Lanczos algorithm for solving sparse symmetric generalized eigenproblems," *SIAM Journal on Matrix Analysis and Applications*, vol. 15, no. 1, pp. 228–272, 1994. DOI: 10.1137/S0895479888151111.

[86] G. L. Sleijpen and H. A. Van der Vorst, "A Jacobi–Davidson iteration method for linear eigenvalue problems," *SIAM Review*, vol. 42, no. 2, pp. 267–293, 2000. DOI: 10.1137/S0036144599363084.

[87] M. E. Hochstenbach and Y. Notay, "The Jacobi–Davidson method," *GAMM-Mitteilungen*, vol. 29, no. 2, pp. 368–382, 2006. DOI: 10.1002/gamm.201490038.

[88] H. Voss, "A new justification of the Jacobi–Davidson method for large eigenproblems," *Linear Algebra and its Applications*, vol. 424, no. 2-3, pp. 448–455, 2007. DOI: 10.1016/j.laa.2007.02.013.

[89] J. Rommes, "Arnoldi and Jacobi-Davidson methods for generalized eigenvalue problems $\mathbf{Ax} = \lambda\mathbf{Bx}$ with singular $\mathbf{B}$," *Mathematics of Computation*, vol. 77, no. 262, pp. 995–1015, 2008. DOI: 10.1090/S0025-5718-07-02040-6.

[90] N. K. Borer, M. D. Patterson, J. K. Viken, M. D. Moore, J. Bevirt, A. M. Stoll, and A. R. Gibson, "Design and performance of the NASA SCEPTOR distributed electric propulsion flight demonstrator," in *16th AIAA Aviation Technology, Integration, and Operations Conference*, 2016. DOI: 10.2514/6.2016-3920.

[91] A. M. Stoll, J. Bevirt, M. D. Moore, W. J. Fredericks, and N. K. Borer, "Drag reduction through distributed electric propulsion," in *14th AIAA Aviation Technology, Integration, and Operations Conference*, AIAA 2014-2851, Atlanta, GA, Jun. 2014. DOI: 10.2514/6.2014-2851.

[92] J. Chin, S. L. Schnulo, and A. Smith, "Transient thermal analyses of passive systems on SCEPTOR X-57," in *17th AIAA Aviation Technology, Integration, and Operations Conference*, AIAA 2017-3784, Denver, CO, Jun. 2017. DOI: 10.2514/6.2017-3784.

[93] S. L. Schnulo, J. C. Chin, R. D. Falck, J. S. Gray, K. V. Papathakis, S. C. Clarke, N. Reid, and N. K. Borer, "Development of a multi-phase mission planning tool for NASA X-57 Maxwell," 2018. [Online]. Available: https://ntrs.nasa.gov/archive/nasa/casi.ntrs.nasa.gov/20180005319.pdf.

[94] M. Stolpe and K. Svanberg, "An alternative interpolation scheme for minimum compliance topology optimization," *Structural and Multidisciplinary Optimization*, vol. 22, pp. 116–124, 2001. DOI: 10.1007/s001580100129.

[95] R. Haimes and M. Drela, "On the construction of aircraft conceptual geometry for high-fidelity analysis and design," in *50th AIAA Aerospace Sciences Meeting Including the New Horizons Forum and Aerospace Exposition*, AIAA 2012-0683, Nashville, TN, Jan. 2012. DOI: 10.2514/6.2012-683.

[96] T. W. Chin, M. L. Leader, and G. J. Kennedy, "A scalable framework for large-scale 3D multimaterial topology optimization with octree-based mesh adaptation," *Advances in Engineering Software*, vol. 135, 2019. DOI: 10.1016/j.advengsoft.2019.05.004.

[97] G. J. Kennedy and J. R.R. A. Martins, "A parallel finite-element framework for large-scale gradient-based design optimization of high-performance structures," *Finite Elements in Analysis and Design*, vol. 87, no. 0, pp. 56 –73, Sep. 2014. DOI: 10.1016/j.finel.2014.04.011.

[98] T. Isaac, C. Burstedde, L. Wilcox, and O. Ghattas, "Recursive algorithms for distributed forests of octrees," *SIAM Journal on Scientific Computing*, vol. 37, no. 5, pp. C497–C531, 2015. DOI: 10.1137/140970963.

[99] C. Burstedde, L. C. Wilcox, and O. Ghattas, "P4est: Scalable algorithms for parallel adaptive mesh refinement on forests of octrees," *SIAM Journal on Scientific Computing*, vol. 33, no. 3, pp. 1103–1133, 2011. DOI: 10.1137/100791634.

[100] S. J. Owen, "A survey of unstructured mesh generation technology.," in *7th International Meshing Roundtable*, Sandia National Lab, Dearborn, MI, Oct. 1998, pp. 239–267.

[101] J.-F. Remacle, J. Lambrechts, B. Seny, E. Marchandise, A. Johnen, and C Geuzainet, "Blossom-Quad: A non-uniform quadrilateral mesh generator using a minimum-cost perfect-matching algorithm," *International Journal for Numerical Methods in Engineering*, vol. 89, no. 9, pp. 1102–1119, 2012. DOI: 10.1002/nme.3279.

[102] J. Edmonds, E. Johnson, and S. Lockhart, "Blossom I: A computer code for the matching problem," *IBM TJ Watson Research Center, Yorktown Heights, New York*, 1969.

[103] V. Kolmogorov, "Blossom V: A new implementation of a minimum cost perfect matching algorithm," *Mathematical Programming Computation*, vol. 1, no. 1, pp. 43–67, 2009. DOI: 10.1007/s12532-009-0002-8.

[104] P. M. Knupp, "Algebraic mesh quality metrics for unstructured initial meshes," *Finite Elements in Analysis and Design*, vol. 39, no. 3, pp. 217 –241, 2003. DOI: 10.1016/S0168-874X(02)00070-7.

[105] Sandia National Laboratories. (2018). CUBIT, the Sandia National Laboratory automated mesh generation toolkit, [Online]. Available: https://cubit.sandia.gov/public/15.3/help_manual/WebHelp/cubithelp.htm (visited on 07/2018).

[106] R. Stainko, "An adaptive multilevel approach to the minimal compliance problem in topology optimization," *Communications in Numerical Methods in Engineering*, vol. 22, no. 2, pp. 109–118, 2006. DOI: 10.1002/cnm.800.

[107] O. C. Zienkiewicz and J. Z. Zhu, "A simple error estimator and adaptive procedure for practical engineerng analysis," *International Journal for Numerical Methods in Engineering*, vol. 24, no. 2, pp. 337–357, 1987. DOI: 10.1002/nme.1620240206.

[108] Y. Wang, Z. Kang, and Q. He, "Adaptive topology optimization with independent error control for separated displacement and density fields," *Computers & Structures*, vol. 135, pp. 50 –61, 2014. DOI: 10.1016/j.compstruc.2014.01.008.

[109] F. Hülsemann, M. Kowarschik, M. Mohr, and U. Rüde, "Parallel geometric multigrid," in *Numerical Solution of Partial Differential Equations on Parallel Computers*, Springer, 2006, pp. 165–208. DOI: 10.1007/3-540-31619-1_5.

[110] N. Aage, E. Andreassen, and B. Lazarov, "Topology optimization using PETSc: An easy-to-use, fully parallel, open source topology optimization framework," *Structural and Multidisciplinary Optimization*, vol. 51, no. 3, pp. 565–572, 2015. DOI: 10.1007/s00158-014-1157-0.

[111] N. Aage, E. Andreassen, B. S. Lazarov, and O. Sigmund, "Giga-voxel computational morphogenesis for structural design," *Nature*, vol. 550, no. 7674, pp. 84–86, 2017. DOI: 10.1038/nature23911.

[112] R. H. Byrd, M. E. Hribar, and J. Nocedal, "An interior point algorithm for large-scale nonlinear programming," *SIAM Journal on Optimization*, vol. 9, no. 4, pp. 877–900, 1999. DOI: 10.1137/S1052623497325107.

[113] R. H. Byrd, J. C. Gilbert, and J. Nocedal, "A trust region method based on interior point techniques for nonlinear programming," *Mathematical Programming*, vol. 89, no. 1, pp. 149–185, 2000. DOI: 10.1007/PL00011391.

[114] A. R. Conn, N. I. Gould, and P. L. Toint, *Trust region methods*. SIAM, 2000, vol. 1.

[115] E. Holmberg, B. Torstenfelt, and A. Klarbring, "Stress constrained topology optimization," *Structural and Multidisciplinary Optimization*, vol. 48, no. 1, pp. 33–47, 2013. DOI: 10.1007/s00158-012-0880-7.

[116] E. Lee, K. A. James, and J. R.R. A. Martins, "Stress-constrained topology optimization with design-dependent loading," *Structural and Multidisciplinary Optimization*, vol. 46, no. 5, pp. 647–661, 2012. DOI: 10.1007/s00158-012-0780-x.

[117] G. J. Kennedy and J. E. Hicken, "Improved constraint-aggregation methods," *Computer Methods in Applied Mechanics and Engineering*, vol. 289, no. 0, pp. 332 – 354, Jun. 2015. DOI: 10.1016/j.cma.2015.02.017.

[118] G. J. Kennedy, "Strategies for adaptive optimization with aggregation constraints using interior-point methods," *Computers & Structures*, vol. 153, no. 0, pp. 217 – 229, Jun. 2015. DOI: 10.1016/j.compstruc.2015.02.024.

[119] A. B. Lambe, G. J. Kennedy, and J. R.R. A. Martins, "An evaluation of constraint aggregation strategies for wing box mass minimization," *Structural and Multidisciplinary Optimization*, vol. 55, no. 1, pp. 257–277, 2017. DOI: 10.1007/s00158-016-1495-1, published.

[120] M. A. Akgun, R. T. Haftka, K. C. Wu, J. L. Walsh, and J. H. Garcelon, "Efficient structural optimization for multiple load cases using adjoint sensitivities," *AIAA Journal*, vol. 39, no. 3, pp. 511–516, 2001. DOI: 10.2514/2.1336.

[121] O. C. Zienkiewicz and J. Z. Zhu, "The superconvergent patch recovery and a posteriori error estimates. part 1: The recovery technique," *International Journal for Numerical Methods in Engineering*, vol. 33, no. 7, pp. 1331–1364, 1992. DOI: 10.1002/nme.1620330702.

[122] R. Picelli, S. Townsend, C. Brampton, J. Norato, and H. Kim, "Stress-based shape and topology optimization with the level set method," *Computer Methods in Applied Mechanics and Engineering*, vol. 329, pp. 1–23, Feb. 2018. DOI: 10.1016/j.cma.2017.09.001.

[123] S. Liu and W. Su, "Topology optimization of couple-stress material structures," *Structural and Multidisciplinary Optimization*, vol. 40, no. 1, pp. 319–327, 2010. DOI: 10.1007/s00158-009-0367-3.

[124] A. P. Seyranian, E. Lund, and N. Olhoff, "Multiple eigenvalues in structural optimization problems," *Structural and Multidisciplinary Optimization*, vol. 8, no. 4, pp. 207–227, 1994. DOI: 10.1007/BF01742705.

[125] T. S. Kim and Y. Y. Kim, "Mac-based mode-tracking in structural topology optimization," *Computers & Structures*, vol. 74, no. 3, pp. 375–383, 2000. DOI: 10.1016/S0045-7949(99)00056-5.

[126] Y. Maeda, S. Nishiwaki, K Izui, M Yoshimura, K Matsui, and K Terada, "Structural topology optimization of vibrating structures with specified eigenfrequencies and eigenmode shapes," *International Journal for Numerical Methods in Engineering*, vol. 67, no. 5, pp. 597–628, 2006. DOI: 10.1002/nme.1626.

[127] A. J. Torii and J. R. d. Faria, "Structural optimization considering smallest magnitude eigenvalues: A smooth approximation," *Journal of the Brazilian Society of Mechanical Sciences and Engineering*, vol. 39, no. 5, pp. 1745–1754, May 2017. DOI: 10.1007/s40430-016-0583-x.

[128] P. Salas, L. Giraud, Y. Saad, and S. Moreau, "Spectral recycling strategies for the solution of nonlinear eigenproblems in thermoacoustics," *Numerical Linear Algebra with Applications*, vol. 22, no. 6, pp. 1039–1058, 2015. DOI: 10.1002/nla.1995.

[129] S. Wang, E. de Sturler, and G. H. Paulino, "Large-scale topology optimization using preconditioned Krylov subspace methods with recycling," *International Journal for Numerical Methods in Engineering*, vol. 69, no. 12, pp. 2441–2468, 2007. DOI: 10.1002/nme.1798.

[130] M. Parks, E. de Sturler, G. Mackey, D. Johnson, and S. Maiti, "Recycling Krylov subspaces for sequences of linear systems," *SIAM Journal on Scientific Computing*, vol. 28, no. 5, pp. 1651–1674, 2006. DOI: 10.1137/040607277.

[131] Y. Saad, *Iterative methods for sparse linear systems*. SIAM, 2003.

[132] O. A. Bauchau and J. I. Craig, *Structural analysis: with applications to aerospace structures*. Springer Science & Business Media, 2009, vol. 163.

[133] S. L. Vatanabe, T. N. Lippi, C. R. de Lima, G. H. Paulino, and E. C. Silva, "Topology optimization with manufacturing constraints: A unified projection-based approach," *Advances in Engineering Software*, vol. 100, pp. 97–112, 2016. DOI: 10.1016/j.advengsoft.2016.07.002.

[134] D Brackett, I Ashcroft, and R Hague, "Topology optimization for additive manufacturing," in *Proceedings of the solid freeform fabrication symposium, Austin, TX*, vol. 1, 2011, pp. 348–362. DOI: 10.1115/DETC2017-68192.

[135] K. Boopathy and G. J. Kennedy, "Parallel finite element framework for rotorcraft multibody dynamics and discrete adjoint sensitivities," *AIAA Journal*, vol. 57, no. 8, pp. 3159–3172, 2019. DOI: 10.2514/1.J056585.

[136] ——, "Adjoint-based derivative evaluation methods for flexible multibody systems with rotorcraft applications," in *55th AIAA Aerospace Sciences Meeting*, AIAA 2017-1671, Grapevine, TX, Jan. 2017. DOI: 10.2514/6.2017-1671.